On the numerical modeling of interfaces in engineering applications

von der Fakultät Maschinenbau
der Technischen Universität Dortmund
zur Erlangung des akademischen Grades

Doktor-Ingenieur (Dr.-Ing.)

genehmigte Dissertation

von

Tillmann Wiegold

aus Hagen

Vorsitz:	Prof. Dr.-Ing. A. Menzel
Referent:	Prof. Dr.-Ing. J. Mosler
Korreferenten:	Prof. Dr.-Ing. S. Klinge
	Prof. Dr. M. Faes
Tag der Einreichung:	04.04.2025
Tag der mündlichen Prüfung:	18.07.2025

Bibliografische Information Der Deutschen Bibliothek
Die Deutsche Bibliothek verzeichnet diese Publikation in der Deutschen Nationalbibliografie; detaillierte bibliografische Daten sind im Internet über **http://dnb.d-nb.de** abrufbar.

Bibliographic information published by Die Deutsche Bibliothek
Die Deutsche Bibliothek lists this publication in the Deutsche Nationalbibliografie; detailed bibliographic data is available in the Internet at **http://dnb.d-nb.de**.

Schriftenreihe des Instituts für Mechanik

Herausgeber: Institut für Mechanik
Fakultät Maschinenbau
Technische Universität Dortmund
Leonhard-Euler-Str. 5
D-44227 Dortmund

Druck: Koffler DruckManagement GmbH

© by Tillmann Wiegold 2025

This work is subject to copyright. All rights are reserved, whether the whole or part of the material is concerned, specifically the rights of translation, reprinting, reuse of illustrations, recitation, broadcasting, reproduction on microfilm or in any other way, and storage in data banks. Duplication of this publication or parts thereof is permitted in connection with reviews or scholarly analysis. Permission for use must always be obtained from the author.

Alle Rechte vorbehalten, auch das des auszugsweisen Nachdrucks, der auszugsweisen oder vollständigen Wiedergabe (Photographie, Mikroskopie), der Speicherung in Datenverarbeitungsanlagen und das der Übersetzung.

Als Manuskript gedruckt. Printed in Germany.

ISSN 2191-0022
ISBN 978-3-947323-53-1

"You fail.
You have to almost fail so many times.
That's how you learn.
You know what you did wrong and then you do it again and you do it again and again and finally you make it.
It's pretty much the same with everything in life."

Ali Boulala

Zusammenfassung

Die vorliegende Arbeit behandelt die Simulation und Modellierung von drei Interfacebeschreibungen anhand von verschiedenen Beispielen. Dabei werden unterschiedliche Diskretisierungsverfahren verwendet, wie die Finite Differenzen, Finite Elemente und Isogeometrische Analyse. Zunächst wird der durch Rezeptordiffusion getriebene Endozytosevorgang beschrieben. Als Basis für die Formulierung dient die Diffusionsgleichung. Das resultierende Gleichungssystem wird mithilfe von finiten Differenzen gelöst. Ziel ist es, das Eindringen eines Virus in eine Zelle abzubilden.
Das zweite Beispiel untersucht die thermo-mechanischen Eigenschaften metallischer Hohlkugeln, nachdem diese durch den Sinterprozess zusammengefügt wurden. Die dünnwandigen Kugeln werden als Schalenelemente mit Hilfe der isogeometrischen Analyse modelliert. Der Fokus liegt dabei auf der thermo-mechanischen Kopplung des zugrundeliegenden Materialmodells sowie der geometrischen Beschreibung mittels NURBS-Ansatzfunktionen. Die Simulationen untersuchen den Einfluss verschiedener Parameter und Randbedingungen auf die Steifigkeit und Verformung der versinterten Strukturen.
Als drittes Beispiel wird die Schädigungsentwicklung unter Einwirkung einer geringen Anzahl an Lastzyklen betrachtet (Low Cycle Fatigue). Dafür wird ein Phasen-Feld-Ansatz mit der Plastizität kombiniert.

Abstract

This thesis deals with the simulation and modeling of three interface descriptions by using different examples. Different discretization methods are used, such as finite differences, finite elements and isogeometric analysis. First, the endocytosis process driven by receptor diffusion is described. The diffusion equation serves as the basis for the formulation. The resulting system of equations is solved by using finite differences. The aim is to depict the penetration of a virus into a cell.
The second example investigates the thermo-mechanical properties of metallic hollow spheres after they have been joined together by the sintering process. The thin-walled spheres are modeled as shell elements by using isogeometric analysis. The focus lies on the thermo-mechanical coupling of the underlying material model and the geometric description via NURBS shape functions. The simulations investigate the influence of various parameters and boundary conditions on the stiffness and deformation of the sintered structures.
As a third example, the development of damage under the influence of a small number of load cycles is considered (low cycle fatigue). For this purpose, a phase-field approach is combined with plasticity.

Publications

Key parts of this thesis are based on peer-reviewed journal articles, which were either published or submitted during the progress of this thesis.

1. T. Wiegold, P. Kurzeja, S. Klinge, J. Mosler: *Non-linear thermo-mechanical modeling of hollow sphere shells using isogeometric analysis*, submitted for publication, 2025.

2. T. Wiegold, S. Klinge, R. P. Gilbert, G. A. Holzapfel: *Numerical simulation of the viral entry into a cell driven by the receptor diffusion*, Computers and Mathematics with Applications, 84:224–243, 2021.

For the journal articles, the author of this thesis contributed essential aspects with regard to the outline of the theory, carried out all of the numerical implementations and simulations, and prepared the articles. The text used in this dissertation represents either the published or currently submitted version of the corresponding paper respectively.

3. S. Aygün, T. Wiegold and S. Klinge: *Coupling of the phase field approach to the Armstrong-Frederick model for the simulation of ductile damage under cyclic load*, Int. J. Plast., 143:103021, 2021.

For the publication mentioned above, all authors confirm, that the author of this thesis contributed essential aspects with regard to preparing algorithmic formulations and derivatives, carrying out numerical implementations, evaluating the simulations, and preparing the article.
In this thesis, the publications mentioned above are cited directly. However, changes to notations, citation numbering, chapter numbering, figure placement and others are made to increase the readability of the thesis. At the submission of this thesis, publication "Non-linear thermo-mechanical modeling of hollow sphere shells using isogeometric analysis" was not yet published but submitted. Thus, citations from this publication refer to a preliminary version. Between this preliminary version and the final publication only minor differences are present, which are not relevant to the content.

In addition, the following contributions were published during and alongside the preparation of this thesis.

1. S. Siddique, M. Awd, T. Wiegold, S. Klinge, F. Walther: *Simulation of cyclic deformation behavior of selective laser melted and hybrid-manufactured aluminum alloys using the phase-field method*, Applied Sciences 8(10), 1948 (2018) 1-18, DOI: 10.3390/app8101948.

2. S. Klinge, T. Wiegold, S. Aygün, R. P. Gilbert and G. A. Holzapfel: *Numerical modeling of the receptor driven endocytosis*, PAMM, 21, 1, e202100142, 2021, DOI: 10.1002/pamm.202100142.

3. T. Wiegold, S. Aygün, S. Klinge: *Numerical simulation of low cycle fatigue behavior, combining the phase-field method and the Armstrong-Frederick model*, PAMM, 21, 1, e202100111, 2021, DOI: 10.1002/pamm.202100111.

4. S. Klinge, T. Wiegold, S. Aygün, R. P. Gilbert and G. A. Holzapfel: *On the mechanical modeling of cell components*, PAMM, 20, 1, e202000129, 2021, DOI: 10.1002/pamm.202000129.

5. T. Wiegold and S. Klinge: *Numerical simulation of cyclic deformation behavior of SLM-manufactured aluminum alloys*, PAMM, 20, 1, e202000181, 2021, DOI: 10.1002/pamm.202000181.

6. T. Wiegold, S. Klinge, R. P. Gilbert and G. A. Holzapfel: *Computational modeling of adhesive contact between a virus and a cellduring receptor driven endocytosis*, PAMM, 19, 1, e201900161, 2019, DOI: 10.1002/pamm.201900161.

7. T. Wiegold, S. Klinge, R. P. Gilbert and G. A. Holzapfel: *Numerical simulation of the viral entry into a cell by receptor driven endocytosis*, Proceedings of 8th GACM Colloquium on Computational Mechanics, 401-404, 2019, DOI: 10.1016/j.camwa.2020.12.012.

8. T. Wiegold, S. Klinge, S. Aygün, R. P. Gilbert, G. A. Holzapfel: *Viscoelasticity of Cross-Linked Actin Network Embedded in Cytosol*, PAMM, 18, 1, e201800151, 2018, DOI: 10.1002/pamm.201800151.

9. M. Awd, S. Siddique, J. Johannsen, T. Wiegold, S. Klinge, C. Emmelmann, F. Walther: *Quality assurance of additively manufactured alloys for aerospace industry by non-destructive testing and numerical modeling*, Proceedings of the 10th International Conference on Non-destructive Testing in Aero-space (2018) 1-10, 2018.

10. S. Klinge, T. Wiegold, G. A. Holzapfel and R. P. Gilbert: *The influence of binder mobility on the viral entry into a cell*, PAMM, 17.1, 197-198, 2018, DOI: 10.1002/pamm.201710068.

Contents

1 Introduction

1.1 Overview on mechanical interfaces and their applications

The description of interfaces is a specific research area in mechanics. A current overview on the physics and chemistry of interfaces is presented in [35]. An extensive overview is provided in [2, 77], covering fundamental physical and mathematical approaches. As a more specific example of classification in mechanics, interfaces can either be modeled as sharp interfaces or diffuse interfaces (with a finite thickness). Regarding the latter and as introduced in [36] and [4], sharp interfaces were described by phase field theory. In addition, interface models can be classified into perfect interface models, not allowing a displacement jump or a traction jump across the interface and into general imperfect interface models, where either a displacement jump (elastic interface model), a traction jump (cohesive interface model) or both (general interface model) are present.
In order to highlight the broad range of applications of interface modeling, some prominent interface examples in engineering applications are presented next. A visualization of these examples is summarized in Fig. 1.1. A well-known case for interfaces is the Stefan problem [123], formulating a classic problem in heat transfer and phase change. It describes the melting or freezing process in a system containing a solid and a liquid phase. Classic applications are the solidification of molten metal or the melting of ice. The system is described by an initial binary temperature distribution, separated by a distinct boundary. Throughout the melting process, both the location of the boundary and its width can be subject to change. Figure 1.1 a) visualizes a system with two initially separated phases and a possible evolution of the interface in space and time. The problem is characterized by the heat equation in combination with a moving or free boundary condition. One of the main aspects is a coupling of the boundary velocity to the heat flux.
Another well-known problem is the description of charged solid surfaces in liquids [69], characterized as electric double layers. This can be experienced on various surfaces, such as metals, oxides and biomembranes. Electric double layers form at surfaces submerged

into a solution and affect the electric potential in its vicinity. A corresponding visualization is given in Fig. 1.1 b). The first layer is the so called Stern layer, characterized by the ions which are bound tightly to the solid surface. The second layer, the diffuse layer, is the region in which the ions mix with the liquid and no longer represent a tight formation. The process is characterized by electrostatic attraction between the surface charge and counterions in the liquid which are balanced by thermal motion. Mathematically, the Poisson-Boltzmann equation is applied for the potential distribution across the double layer, while the Debye length describes the thickness of the diffuse layer, which depends on the ionic strength of the solution.
Still present to this day, interfaces are an elemental part in biology, especially in the human body. They can be found from the nano meter regime up to the centimeter regime. A joint is an example for the larger scale [163]. Joints present a system of constant friction, causing wear to the bone surface. A schematic presentation of the degradation process is presented in fig 1.1 c). The underlying problem is characterized by damage mechanics in combination with contact modeling for a high amount of load steps.
The fourth example resembles a mechanical problem of damage and crack evolution [31]. It has been shown that by introducing a phase-field parameter, the damage evolution can be depicted independent of the underlying discretization of the problem [97]. Figure 1.1 d) shows the typical evolution of a crack in a plate with initial defect, highlighted by the distinct red line. Modeling cracks by means of standard finite element methods often leads to mesh dependency. This pathological effect can be eliminated by regularization methods, e.g., [50, 55, 89].
Independent of the considered problem, different spatial discretization schemes can be used. Some examples include the finite difference method (FDM) [67], finite element methods (FEM) [122] and isogeometric analysis (IGA) [76]. Each presenting unique benefits to approach a given problem, providing customized solutions.

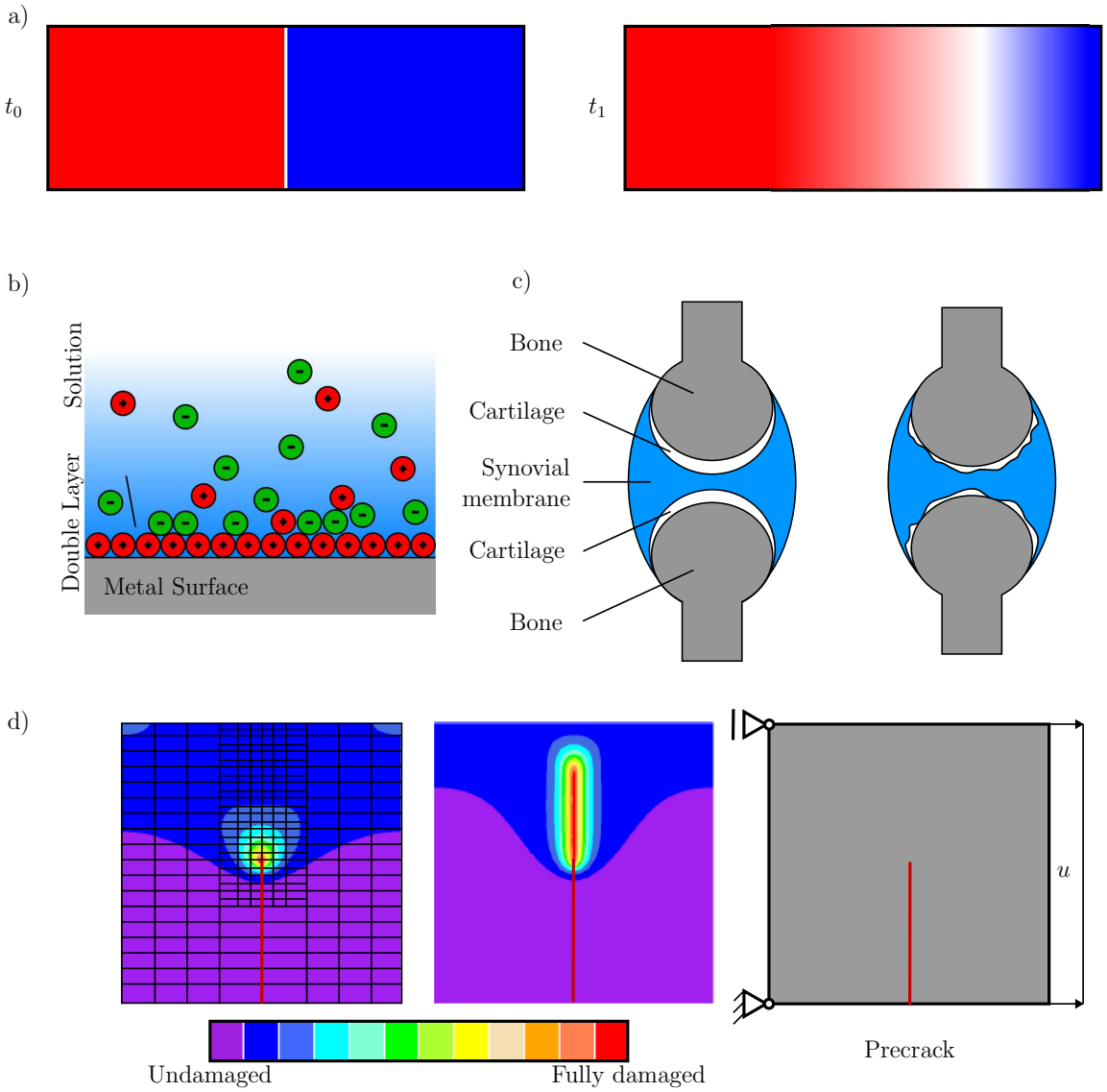

Figure 1.1: Schematic representation of different interface applications. a) Stefan problem, illustrating the temperature evolution in space and time [131]. b) Electric double layer at a metal surface submerged into a solution [150]. c) Simplified representation of a joint, visualizing structural degradation [134]. d) Visualization of a crack evolution in a plate with initial defect, as well as its boundary conditions. The coloration indicates the value of the damage variable. The visualization of the mesh does not correspond to the real discretization and is used here to emphasize the principal of local refinement in the crack path [16].

1.2 Objective of this work

The broad range of applications of interface mechanics and versatility of numerical solutions presents a broad spectrum of possible approaches. This work covers two unique applications and their different modeling approaches. Specific benefits are highlighted and discussed.
The first application describes the viral entry into a cell by means of endocytosis [157]. Different pathways exist for a virus to enter the cell. This work highlights the uptake by receptor-driven endocytosis. The process is characterized in Fig. 1.2. While interfaces appear in various sizes, processes such as the viral uptake into a cell happen in the nano meter regime. While the bodies involved in this process are already of small size, the difference between the virus and cell size is still significant. Therefore, the virus can be modeled as a spherical body, while the cell can be represented by an initially flat surface, in the area relevant to the process. Once the virus is close enough to the cell's surface its receptors start to connect to the cell receptors, creating a distinct contact area. In order to enter the cell the virus requires a local increase in receptor density. The receptors on the cells are free to move within its surface, forming an envelope around the virus until it has entered the cell. This process, similar to the Stefan problem, combines a diffusion process of the cell receptors with a moving boundary problem at the front of the contact area between virus and cell. Furthermore, it combines a biological system with a similar characterization to a Stern-Layer, where the interaction between virus and cell happens at a distinct interface affecting its embedded surroundings.

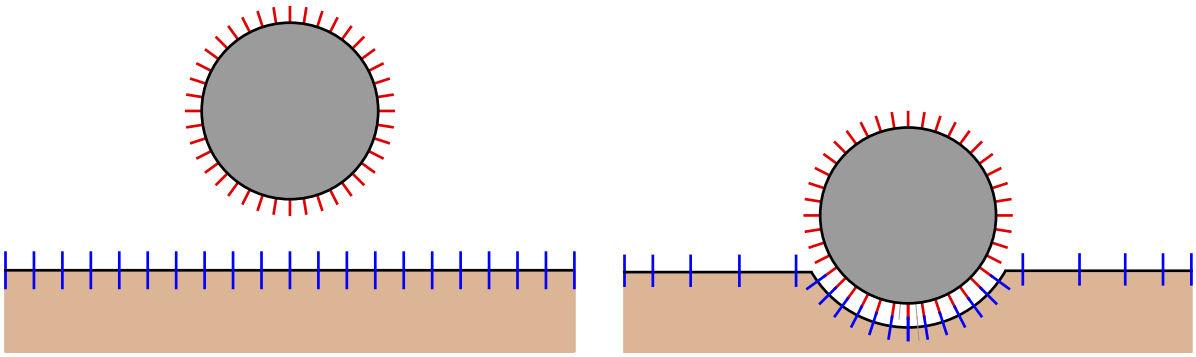

Figure 1.2: Visualization of the viral uptake into a cell by receptor driven endocytosis.

The interface depicts a moving boundary problem at the front of the contact between virus and cell. For this application, a framework based on finite differences is established. The diffusion of receptors on the cell, in combination with two additional conditions describing the conservation of receptors as well as the conservation of energy, describe the underlying process as a nonlinear system of equations. Key points of this work are:

- Moving boundary problem for the simulation of the viral entry

- Heat equation followed by nonlinear boundary conditions

The second application focuses on the sintering of thin walled hollow spheres [156]. Contrary to the viral uptake, sintering can be performed both on large bodies extending several centimeters as well as on small bodies extending just a few micro meters. A variety of phenomena are involved in describing the underlying mechanisms. It is a thermo-mechanically coupled problem, including contact between multiple bodies and often large deformation and different diffusion mechanisms. Figure 1.3 visualizes the different diffusion paths during the sintering process, on the example of two hollow spheres.

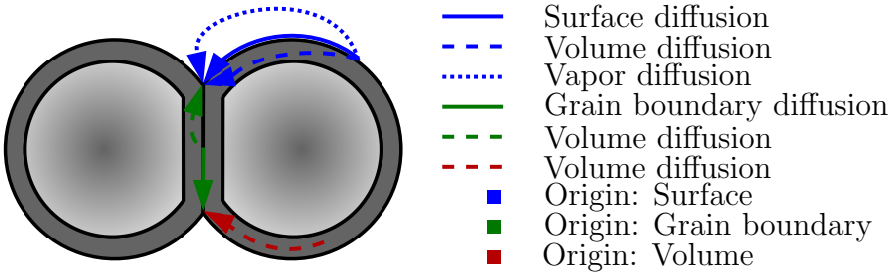

Figure 1.3: Visualization of possible diffusion paths during the sintering process.

The thin walled nature of the spheres motivate their description as shells. Here, a two dimensional shell element, embedded in a three dimensional space, is established on the basis of isogeometric analysis. Key points of this work are:

- Thermo-mechanically coupled problem
- Implementation of a shell element into an IGA framework

The third and final application in this thesis investigates the phase field approach for modeling low-cycle fatigue. For low-cycle fatigue plasticity plays an essential role. Therefore, the phase field approach is coupled to the Armstrong-Frederick (AF) model incorporating kinematic hardening effects. It is especially well suited for describing the ratcheting and Bauschinger effect.

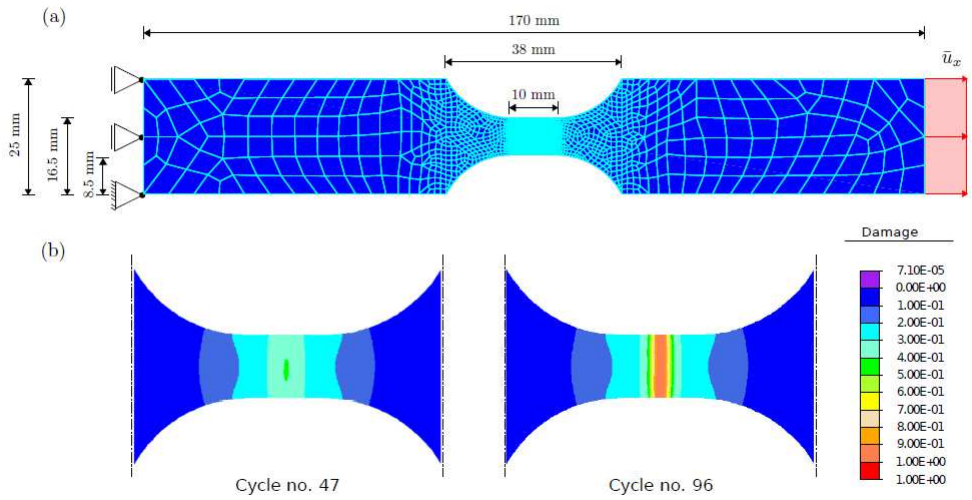

Figure 1.4: Example for the simulation of a classic tensile test specimen under low-cycle fatigue.

Figure 1.4 visualizes the damage evolution in a classic tensile test specimen under cyclic loading. The strain amplitude is kept constant throughout the simulation, highlighting the effect of the plastic model. Key points of this work are:

- Influence of plasticity to low-cycle fatigue
- Legendre transformation to create a coupled formulation

2 Numerical simulation of the viral entry into a cell driven by receptor diffusion

This chapter cites the paper "Numerical simulation of the viral entry into a cell driven by the receptor diffusion" by T. Wiegold, S. Klinge, R. P. Gilbert, G. A. Holzapfel.

Abstract

The present study focuses on the receptor driven endocytosis typical of viral entry into a cell. A locally increased density of receptors at the time of contact between the cell and the virus is necessary in this case. The virus is considered as a substrate with fixed receptors on its surface, whereas the receptors of the host cell are free to move over its membrane, allowing a local change in their concentration. In the contact zone the membrane inflects and forms an envelope around the virus. The created vesicle imports its cargo into the cell. This paper assumes the diffusion equation accompanied by boundary conditions requiring the conservation of binders to describe the process. Moreover, it introduces a condition defining the energy balance at the front of the adhesion zone. The latter yields the upper limit for the for the size of virus which can be engulfed by the cell membrane. The described moving boundary problem in terms of the binder density and the velocity of the adhesion front is well posed and numerically solved by using the finite difference method. The illustrative examples have been chosen to show the influence of the process parameters on the initiation and the duration of the process.

2.1 Introduction

The intense study of cell mechanisms has provided an important insight into the uptake of various substances into a cell including viruses. Diagnosis and therapy of diseases has reached a state in which nanomedicine concerned with devices of nanoscale size is applied. With these, they can deliver low molecular mass compounds, proteins and recombinant DNAs to focal areas of disease. Some examples are polymeric micelles, quantum

dots, liposomes, polymer-drug conjugates, dendrimers, biodegradable nanoparticles, silica nanoparticles, etc. researched in laboratories, undergoing preclinical development, or already used in hospitals [44, 142]. In addition, numerical methods in biomechanics and biomathematics become more relevant. A variety of numerical methods ranging from multiscale finite elemente [78] and isogeometric shell formulations [51] to relaxation dynamics [13] find their application in biomechanics.

The cell is surrounded by a plasma membrane which acts as the interface between the cell and its surrounding environment. However, the membrane is not absolutely impermeable and a transport of particles through the membrane is still possible. Among many different mechanisms, the most common process for this purpose is the so-called endocytosis [65]. The main focus of the investigation of endocytosis has so far been on clathrin-mediated endocytosis (CME). During the CME, proteins create clathrin-coated pits which eventually build whole vesicles [129, 135].

Various aspects of the endocytosis process are investigated in different chemical and biochemical contexts. Amongst others, the total internal reflection illumination with fluorescence correlation spectroscopy is used to measure ligand-receptor kinetic dissociation rate constants [99]. Trafficking phenomena are studied based on internalization experiments utilizing multiscreen assay systems [54]. Furthermore, biomimetic systems of lipid vesicles or supported bilayers with a variety of binder molecules deal with soft adhesion mediated by mobile binders as shown in [56, 111]. The behavior and stability of adhesion complexes are also addressed by using cell doublet [53, 143] and vesicles adhered to supported bilayers [133].

The experimental progress has parallely led to multiple theoretical models. A mathematical framework, based on probabilities for binding rates, introducing a random and a sequential driving mechanism for the receptors is provided in [66]. Discrete stochastic models for specific receptor-ligand adhesion as well as non-equilibrium continuum models for the competition between different modes of junction remodeling under force are developed in [86], whereas a statistical thermodynamic model of viral budding is presented in [146]. Several analytical models for the endocytosis process utilize the description of the Stefan problem, [61, 62] and propose a solution relying on the error and complementary error functions. These methods are particularly applied to the HIV-Virus [139] and Semliki Forest virus [62] but also for the uptake of nanoparticles [164]. Alternatively, Tseng and Huang [144] use the immersed boundary method to simulate the endocytosis and to investigate the resistance of the water film in the contact area.

The current contribution uses the model presented in [61, 62] as a basis, however, it proposes an alternative form of the Stefan supplementary condition where the focus is only set on the energetic aspects of the front itself, and a consideration of the dissipation associated with the receptor transport along the cell membrane is not needed. Different from the previous models, the new formulation yields the upper limit for the size of virus able to enter the cell. Another focus of the paper is the purely numerical solution of the moving boundary problem where no additional assumptions typical of analytical solutions such as the speed factor [61, 62] are necessary. The chosen interpretation of

the problem is advantageous for the fast simulation of various scenarios regarding the process parameters and their influence on the initiation and duration of the process. As a final objective, the paper also introduces the notion of cooperativity [94, 154] into the numerical model and performs a more sophisticated study of the effective receptor distribution on a virus and of its influence on the viral entry into a cell.

This contribution is structured as follows: A general overview of the uptake process is summarized in Sect. 2.2, whereas Sect. 2.3 recapitulates the main aspects of the free energy characteristic for the endocytosis process. After this introductory part, Sect. 2.4 focuses on the definition of boundary and supplementary conditions accompanying the driving diffusion differential equation. The boundary conditions define the flux balance, and supplementary condition represents the energy balance at the adhesion front. Subsequently, Sect. 2.5 discusses the numerical implementation for the 1D case and helical viruses, which is followed by a non-dimensional description of the problem in Sect. 2.6. The paper also deals with a common case of a spherical virus (Sect. 2.7) and extends the basic model by introducing the notion of cooperativity (Sect. 2.8). Finally, Sect. 2.9 gives a comprehensive overview of results and provides a comparison with the experimental observations and numerical results from the literature. The paper finishes with a conclusion and an outlook.

2.2 Description of the uptake process

In a basic view of mechanical adhesive contact between elastic surfaces, two phenomena which have a considerable influence on the underlying process counteract each other. A reduction in the free energy when surfaces with bonding potential come into contact benefits the process, whereas an increase in free energy due to elastic deformation required to fit their shapes counteract the process. In the classic Hertzian theory of elastic deformation [82], two bodies coming into contact deform in the contact area in such a way that they perfectly fit. According to this approach any surface interactions such as Van der Waals forces, which are induced by charge polarization in electrically neutral molecules in close proximity, are excluded. However, these 'non-material' effects have a significant influence on the direct contact interaction [22]. This is illustrated by considering small elastic objects consisting of crystalline materials processed in a controlled environment. Such crystals show the appearance of unfulfilled or dangling chemical bonds distributed over a free surface. Bringing such objects into contact reduces the free energy of the system by forming bonds between the two surfaces. The objects joined in this way will not separate without additional work. Hence, not only compressive traction due to bulk elasticity but also an adhesive or tensile traction contributes to the contact [61]. General investigations of the mechanisms on adhesive contact are presented in [47, 83, 90, 103].

The same effects, both attractive and resisting interactions, appear in the adhesive contact of biological cells. However, due to their characteristic properties compared to engineering materials, significant differences occur in this case. Having a remarkably

lower elastic modulus than engineering materials weakens the influence of the effect of elastic energy variations during contact [61]. Furthermore, cells are characterized by a fluid-like in-plane behavior[124]. This enables the receptors of the cell to move within its membrane, enabling new methods of incorporating free energy variations in the modeling of adhesive contact.

For a long time, electron microscopy has been used to provide valuable insight into the architecture of viruses [43]. Furthermore, fluorescent-labeling of viruses and cellular structures combined with fluorescence microscopy yield more dynamic information for the tracking of a single virus in live cells [34]. In order to obtain 3D geometrical and distributional information, electron tomography has also shown to be a powerful tool [19]. Thus, a large amount of information on the architecture of viruses is already available. For example, a spike protein density of approximately 2800 μm^{-2} is identified for Sars-Cov [24] and the value of approximately 5200 μm^{-2} for an Alphavirus [146]. With regard to the geometry, the investigations have shown that the helical and spherical virus forms are predominant [41].

In order to depict the process of viral entry into a cell, the situation presented in Fig. 2.1 is considered. This 1D situation is suitable to simulate the endocytosis of helical virus into a cell. However, an extension to the rotationally symmetric case and to the simulation of a spherical virus is straightforward (Sect. 2.7). In the initial state, the virus has not yet reached the cell surface (Fig. 2.1a). Upon first contact, the virus gradually connects to the cell (Fig. 2.1b). In order to establish a connection between the virus and the cell, a generic repulsion between their surfaces needs to be overcome.

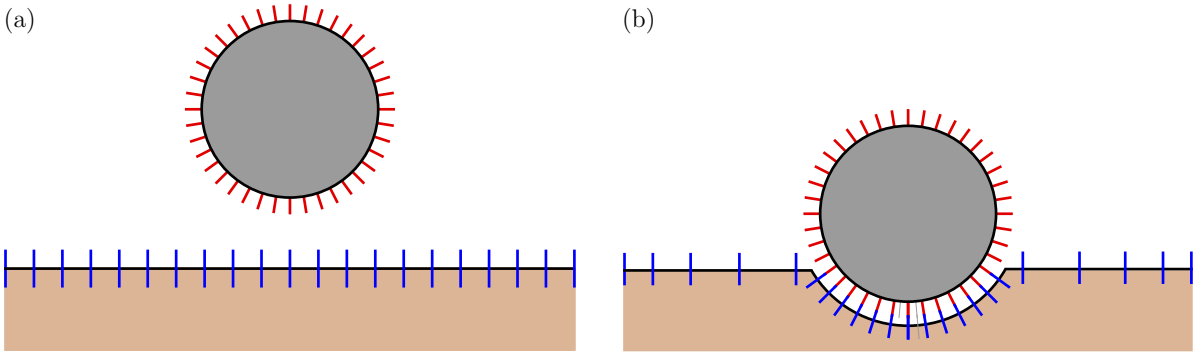

Figure 2.1: a) Initial configuration of the cell surface and the virus in a 2D setup; b) state during the uptake where the virus is partially connected to the cell.

The connection by binding receptors of the virus to receptors of the cell reduces the internal energy of the system. Upon completing a single receptor-ligand bond, the internal energy is reduced by $k\,T\,C_\mathrm{b}$, where k is the Boltzmann constant, T the absolute temperature and C_b the binding energy coefficient.

The quantity driving the uptake process is receptor density ξ. Initially, the density of receptors on the cell surface amount to ξ_0 and the corresponding counterpart, the receptor density on the virus surface, amounts to ξ_rv. In general, it holds that the

density of receptors on the virus is larger than the one on the cell surface and that the virus receptors are fixed, whereas the receptors of the cell are free to move across the membrane. Upon contact, receptors of the cell diffuse over the surface, connect to the receptors of the virus and build an envelope around the virus. At the end of the process the envelope is closed over the virus which has fully entered the cell.

As opposed to metallic or covalent bonds, the bonds created during biological adhesion are relatively weak. Since the cell receptor density is the lower one, in general, it dictates the amount of reduction in the internal energy. Typically, the resisting potential due to generic repulsion exceeds the reduction in internal energy of the initial configuration of the system for a unit area of the membrane at ξ_0. Therefore, additional influences facilitate the creation or dissolving of chemical bonds. Possible influences are catalytic agents, small temperature changes and small mechanical forces. It appears that a local change in receptor density is necessary in order to create an adhesion zone between the virus and the cell. An increasing local receptor density results in a greater reduction in the free energy by completion of each additional bond. When the cell receptors and the virus receptors are close to each other, a permanent interaction is present due to thermal stimulation.

In the framework of chemical rate theory two distinct cases are differentiated [46]. In the area where $\xi < \xi_{\mathrm{eq}}$ holds, the rate of bond breaking exceeds the rate of bond forming, so that no adhesive contact is established. In the area where $\xi > \xi_{\mathrm{eq}}$ holds, the rate of bond forming exceeds the rate of bond breaking, and a strong adhesive contact is established. Condition $\xi = \xi_{\mathrm{eq}}$ defines the chemical equilibrium of the bonding reaction as well as the lower limit for the adhesion to start. Whereas it is known that $\xi_{\mathrm{eq}} > \xi_0$ in the case of cell-virus contact, different assumptions can be made for the exact value of ξ_{eq}. In a limiting case, the chemical equilibrium requires all receptors of the virus to be bonded to the cell membrane such that $\xi_{\mathrm{eq}} = \xi_{\mathrm{rv}}$. It is more likely to expect that the equilibrium density ξ_{eq} is in the range $[\xi_0, \xi_{\mathrm{rv}}]$ and that it might vary during the process. Some of these aspects are considered in Sect. 2.8 on cooperativity, an effect significantly influencing the exact value of ξ_{eq}. However, the initial study is performed for the most restrictive case $\xi_{\mathrm{eq}} = \xi_{\mathrm{rv}}$, which does not influence the generality of the model.

As an illustration, a schematic distribution of receptors over the cell and the virus is depicted in Fig. 2.2a, whereas the corresponding density profile is shown in Fig. 2.2b. In the adhesive zone, the receptor density is constant and amounts to ξ_{eq}. The density starts to grow outside the adhesive zone and, only when far away from it, moves towards the initial density value of the cell ξ_0. Since the size of the cell is magnitudes larger than the virus, we assume the receptor density far away from the adhesion front to stay constant $\lim_{x\to\infty} \xi(x,t) = \xi_0$. Consequently, the flux j of the receptors vanishes so that $\lim_{x\to\infty} j(x,t) = 0$.

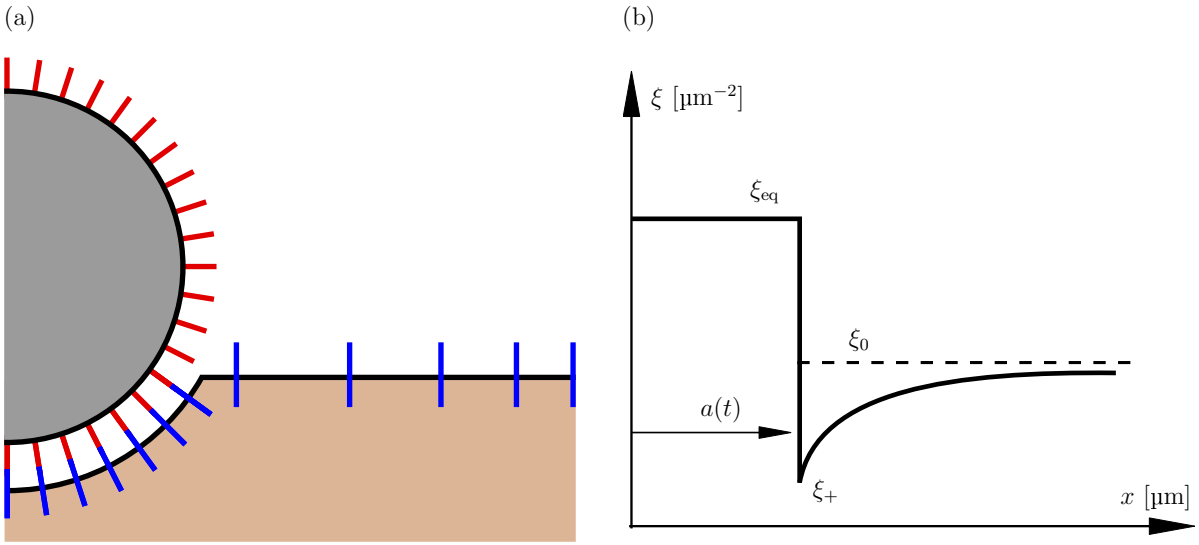

Figure 2.2: a) Schematic diagram for the receptor distribution over the cell and virus surface; b) typical density profile.

One more peculiarity of diagram 2.2b is the front of the adhesion zone where a jump of the receptor density occurs. The position of the front is denoted by a time dependent function $a(t)$. The discontinuous profile is expected since the equilibrium density is high and certainly larger than ξ_0, whereas the receptor density ahead of the front must be lower than ξ_0 in order to stipulate the receptor diffusion. The values typical of the adhesion front play an essential role in the model to be described, and are denoted by the subscript + in the subsequent text. For example, ξ_+ denotes the receptor density at the front.

The previous explanation shows that the whole process is regulated by the diffusion of receptors over the cell surface and their gathering in the adhesion zone. Accordingly, the motion of the receptors will be described by the diffusion differential equation

$$\frac{\partial \xi}{\partial t} = -\frac{\partial j}{\partial x} \tag{2.1}$$

which states that the change of receptor density in time has to be equal to the negative spatial change in the flux. Furthermore, following Fick's first law, the receptor flux j is proportional to the gradient of density, i.e.

$$j = -m \frac{\partial \xi}{\partial x}, \tag{2.2}$$

such that the implementation of Eq. (2.2) into Eq. (2.1) leads to the alternative expression of the diffusion equation

$$\frac{\partial \xi}{\partial t} = m \frac{\partial^2 \xi}{\partial x^2}. \tag{2.3}$$

This equation defines the relation between the temporal and the spatial changes of the receptor density weighted by the mobility parameter m. Its evaluation gives insight into the evolution of receptor density for every point in front of the adhesion zone $a(t) < x < \infty$. Equation (2.3) is a partial differential equation of second order and requires additional boundary conditions in order to determine the complete particular solution. These two conditions will be defined in the upcoming sections.

2.3 Process characterization

In order to define the free energy characteristic of the simulated process, the system including a large number of receptors is treated analogously to the case of an ideal gas with a large number of non-interacting particles N. In such a case, the entropy of a single particle, belonging to a system in equilibrium, is expressed by $k \ln[(A/\Lambda^2)\,(c/N)]$ [61]. Here, A is the considered surface, N/A is the areal density ξ, c is a numerical factor and Λ a molecule length scale [49]. However, the latter two quantities (c and Λ) do not play any role for the description of our process since it does not depend on the absolute entropy but on its change. This change is described with respect to the initial state of the cell with uniform density ξ_0 which is chosen to be the reference state. The relative entropy of a single receptor at density ξ is then described by its difference to the reference state and is calculated according to [61] by

$$k \ln\left(\frac{c}{\xi \Lambda^2}\right) - k \ln\left(\frac{c}{\xi_0 \Lambda^2}\right) = -k \ln\left(\frac{\xi}{\xi_0}\right). \tag{2.4}$$

With the expression for one receptor at hand, and assuming that the gradient in the distribution is small and that the local distribution is indistinguishable from an equilibrium distribution at local density, the free energy E_e per unit area of membrane surface associated to the receptor distribution at absolute temperature T turns into

$$E_\mathrm{e} = k\,T\,\xi \ln\left(\frac{\xi}{\xi_0}\right). \tag{2.5}$$

Moreover, the chemical potential χ is defined as the local change in the free energy per receptor,

$$\chi(x,t) = \frac{\partial E_\mathrm{e}}{\partial \xi} = k\,T \left[\ln\left(\frac{\xi}{\xi_0}\right) + 1\right]. \tag{2.6}$$

Finally, the mean receptor speed is assumed to be proportional to the spatial gradient of the chemical potential, i.e.

$$v_{\mathrm{r}} = -\frac{m}{k\,T}\frac{\partial \chi}{\partial x} = -\frac{m}{\xi}\frac{\partial \xi}{\partial x}, \tag{2.7}$$

where the motion of the receptors is controlled by the mobility parameter m.

2.4 Boundary and supplementary conditions

The full description of the adhesion front motion relies on a problem formulation including the differential equation (2.3) along with two boundary conditions describing the flux at the ends of the domain and along with a supplementary condition.

2.4.1 Flux balance

The boundary conditions on the unbound area are concerned with the quantitative description of the flux of receptors through the adhesive front. Following the Leibniz integration rule of the global form, this condition is derived from Eq. (2.1) as

$$(\xi_{\mathrm{eq}} - \xi_{+})\, v_{+} + j_{+} = 0, \tag{2.8}$$

or by using Fick's first law as

$$(\xi_{\mathrm{eq}} - \xi_{+})\, v_{+} - m \left[\frac{\partial \xi}{\partial x}\right]_{+} = 0. \tag{2.9}$$

Here, the first term denotes the amount of receptors required for the advancement of the front, and the second term denotes the amount of receptors provided by the flux. Both previous formulations depend on the front velocity defined in terms of the front position $v_{+} = \frac{\mathrm{d}\,a}{\mathrm{d}\,t}$. Equation (2.9) is consistent with the assumption (2.7), which can easily be shown as follows. First, the flux is assumed to be proportional to the receptor distribution ξ and the mean receptor velocity v_{r}:

$$j = \xi\, v_{\mathrm{r}}. \tag{2.10}$$

By incorporating Eq. (2.7) into Eq. (2.10), the flux turns into

$$j = -\frac{m}{k\,T}\,\xi\,\frac{\partial \chi}{\partial x} = -m\frac{\partial \xi}{\partial x}, \tag{2.11}$$

as predicted by Fick's first law.

2.4.2 Energy balance

The supplementary condition is provided by considering the energetic aspects of the front motion. The change of the receptor distribution as well as of the membrane shape leads to several contributions to the free energy of the system. However, the crucial observation is that the difference in the energy ahead of and behind the front results in the front motion, which is expressed as follows,

$$E^- - E^+ = E_{\text{kin}}. \tag{2.12}$$

Here, E^- denotes the energy behind the adhesion front, E^+ is the energy ahead of the front and E_{kin} is the kinetic energy of the front itself.

The term related to the energy behind the front is built of three contributions, all denoted by superscript $-$,

$$E^- = E_{\text{b}}^- + E_{\text{e}}^- + E_{\kappa}^-. \tag{2.13}$$

These terms have the following physical meaning: E_{b}^- is the energy related to the binding of receptors, E_{e}^- the energy related to the entropy and E_{κ}^- the energy related to the bending of the membrane. The reduction in the free energy due to the binding of receptors of the cell to receptors of the virus is defined as follows

$$E_{\text{b}}^- = -k\,T\,C_{\text{b}}\,\xi_{\text{eq}}. \tag{2.14}$$

This term is proportional to the reduction of energy caused by a single bond between two receptors $-k\,T\,C_{\text{b}}$, and to the total amount of created bonds ξ_{eq} dictated by the virus. As stated in [61], the binding energy coefficient C_{b} typically takes values in the range $5 < C_{\text{b}} < 35$. The second term describes the energy associated with the entropy of receptors

$$E_{\text{e}}^- = k\,T\,\xi_{\text{eq}} \ln\left(\frac{\xi_{\text{eq}}}{\xi_0}\right), \tag{2.15}$$

which is required to bring the density from its reference value ξ_0 to the density of the virus ξ_{eq}. This term will result in an increase in the free energy since it holds $\xi_0 < \xi_{\text{eq}}$. The third term of (2.13) is concerned with the bending of the membrane caused by the geometry of the virus

$$E_{\kappa}^- = \frac{1}{2}\,k\,T\,B\,\kappa^2. \tag{2.16}$$

Here, a simplified case is considered corresponding to the theory of the bending of a plate. Factor B represents the non-dimensional numerical parameter for the bending stiffness, which is in the range of 10 to 30 and $\kappa = 1/R$ represents the curvature, which

is constant for a spherical virus and which depends on the radius of the virus R. Thus, the whole energy behind the front is then defined by the expression

$$E^- = -k\,T\,C_\mathrm{b}\,\xi_\mathrm{eq} + k\,T\,\xi_\mathrm{eq}\ln\left(\frac{\xi_\mathrm{eq}}{\xi_0}\right) + \frac{1}{2}\,k\,T B\,\kappa^2. \tag{2.17}$$

In the second step we consider the energy ahead of the front, denoted by superscript $+$. Binding between the cell and the virus exclusively takes place in the area behind the front and thus does not have any influence on the energy ahead of the front. However, corresponding parts E_e^+, the energy related to the entropy and E_κ^-, the energy related to the curvature of the membrane remain available. Moreover, a term E_v^+, the energy related to the motion of receptors also has to be taken into consideration. In summary, the following terms can be counted ahead of the front:

$$E^+ = E_\mathrm{e}^+ + E_\kappa^+ + E_\mathrm{v}^+. \tag{2.18}$$

In the present contribution, we assume that the curvature behind the front is much smaller than the one caused by the contact with the virus. This justifies the assumption of a vanishing influence to the energy associated to the bending of the membrane

$$E_\kappa^+ = 0. \tag{2.19}$$

The energy ahead of the front related to the entropy is expressed in the same way as the energy behind the front as

$$E_\mathrm{e}^+ = k\,T\,\xi_+\ln\left(\frac{\xi_+}{\xi_0}\right). \tag{2.20}$$

It describes the energy needed in order to bring the initial receptor density ξ_0 to the value ξ_+. Contrary to the contribution behind the front, this term results in a reduction of the free energy since $\xi_0 > \xi_+$. The contribution due to the motion of the receptors reads

$$E_\mathrm{v}^+ = \frac{1}{2}\,m_\mathrm{r}\,\xi_+\,v_\mathrm{r}^2 = \frac{1}{2}\,m_\mathrm{r}\,\frac{m^2}{\xi_+}\,\left(\frac{\partial \xi_+}{\partial x}\right)^2. \tag{2.21}$$

It represents the kinetic energy of all receptors ahead of the front moving towards the front with their corresponding velocity v_r and the cell receptor mass m_r. With Eqs. (2.19) - (2.21), the total energy ahead of the front is defined by

$$E^+ = k\,T\,\xi_+\ln\left(\frac{\xi_+}{\xi_0}\right) + \frac{1}{2}\,m_\mathrm{r}\,\frac{m^2}{\xi_+}\,\left(\frac{\partial \xi_+}{\partial x}\right)^2. \tag{2.22}$$

Finally, the difference between the energies of the two sides of the front acts as driving force for the front motion. The kinetic energy of the front is then characterized by the mass of the front $m_{\mathrm{rr}}\,\xi_{\mathrm{eq}}$ and the front velocity v_+

$$E_{\mathrm{kin}} = \frac{1}{2}\, m_{\mathrm{rr}}\, \xi_{\mathrm{eq}}\, v_+^2. \tag{2.23}$$

Here, m_{rr} represents the mass of a receptor pair including the cell receptor and the virus receptor which are bonded to each other. Combining Eq. (2.17), (2.22) and (2.23) leads to the expression

$$-\xi_{\mathrm{eq}}\, C_{\mathrm{b}} + \xi_{\mathrm{eq}} \ln\left(\frac{\xi_{\mathrm{eq}}}{\xi_0}\right) + \frac{1}{2} B\kappa^2 - \left[\xi_+ \ln\left(\frac{\xi_+}{\xi_0}\right) + \frac{1}{2}\frac{m_{\mathrm{r}}}{k\,T}\,\frac{m^2}{\xi_+}\,\left(\frac{\partial \xi_+}{\partial x}\right)^2\right] = \frac{1}{2}\,\xi_{\mathrm{eq}} \frac{m_{\mathrm{rr}}}{k\,T}\, v_+^2, \tag{2.24}$$

which is the final form of the supplementary condition and closes the formulation of the moving boundary problem.

2.5 Numerical implementation and results for 1D case and helical viruses

2.5.1 Implementation

In summary, the change of the receptor distribution is described by a system of differential equations consisting of (2.3), (2.9) and (2.24). The finite difference method has been chosen for the solution of the underlying system of differential equations. According to this approach, all derivatives are replaced by expressions dependent on discrete values of the function for the nodes of a chosen lattice. Thus the differential equations are transformed into a system of algebraic equations. An implicit scheme is used, with the following approximations for the derivatives

$$\frac{\partial \xi}{\partial t} \approx \frac{\xi_i^{j+1} - \xi_i^j}{\Delta t}, \quad \frac{\partial \xi}{\partial x} \approx \frac{\xi_i^{j+1} - \xi_{i+1}^{j+1}}{\Delta x}, \quad \frac{\partial^2 \xi}{\partial x^2} \approx \frac{\xi_{i-1}^{j+1} - 2\xi_i^{j+1} + \xi_{i+1}^{j+1}}{\Delta x^2}. \tag{2.25}$$

Here, subscript i denotes the spatial position and superscript j denotes the time. The implementation of relationships (2.25) into the system (2.3), (2.9) and (2.24) leads to the following discretized formulation of the problem:

$$\frac{\xi_i^{j+1} - \xi_i^j}{\Delta t} = m \frac{\xi_{i-1}^{j+1} - 2\xi_i^{j+1} + \xi_{i+1}^{j+1}}{\Delta x^2}, \quad i = 1, ..., p, \quad j = 1, ..., n, \tag{2.26a}$$

$$\left[\xi_{\mathrm{eq}} - \xi_+^{j+1}\right] v_+^{j+1} + m \, \frac{\xi_+^{j+1} - \xi_1^{j+1}}{\Delta x} = 0, \tag{2.26b}$$

$$\left[E^-\right] - \left[\xi_+^{j+1} \ln\left(\frac{\xi_+^{j+1}}{\xi_0}\right) + \frac{1}{2}\frac{m_{\mathrm{r}}}{k\,T}\frac{m^2}{\xi_+^{j+1}}\left(\frac{\xi_1^{j+1} - \xi_+^{j+1}}{\Delta x}\right)^2\right] - \left[\frac{1}{2}\,\xi_{\mathrm{eq}}\frac{m_{\mathrm{rr}}}{k\,T}\;{v_+^{j+1}}^2\right] = 0. \tag{2.26c}$$

In Eq. (2.26a), variable p refers to the total number of points ahead of the front, except the last point where the influence of the flux vanishes and where the receptor density is kept at the initial value ξ_0. Variable n refers to the total number of time steps. Furthermore, the conditions given in Eqs. (2.26b)-(2.26c) are valid at the front. In Eq. (2.26c), E^- is an abbreviation for the contribution defined in (2.17). This term does not depend on the density ξ_i and quantities at the front ξ_+ and v_+, and thus represents a constant during the process.

The solution of system (2.26) yields values for receptor densities ξ_+^{j+1} and ξ_i^{j+1}, $i = 1, ..., p$, and front velocity v_+^{j+1}. The latter is, in postprocessing, used to evaluate the front position in the incremental form: $a^{j+1} = a^j + v_+^{j+1}\Delta\, t$, where $j+1$ and j are two subsequent time steps.

2.5.2 Results

The numerical examples chosen simulate the process of virus uptake into the cell. In the simulations, it is assumed that a helical virus of size $D = 0.05$ µm, comes into contact with a much larger cell such that the cell curvature is negligible (Fig. 2.1). Due to the axial symmetry of the virus, the problem is treated in a 1D representation which assumes the unit width of the active domain. The initial density of cell receptors is set to $\xi_0 = 1000$ µm^{-2}, whereas the initial density of virus receptors is set to $\xi_{\mathrm{eq}} = 4800$ µm^{-2}. Time increment $\Delta t = 1e^{-4}$ s and space increment $\Delta x = 1e^{-3}$ µm are used for the numerical simulations. An overview of the chosen process parameters is given in Table 2.1. These values belong to the corresponding admissible ranges and are also used in [61]. The convergence of results has been checked by varying the time and the space increment. Time increment Δt has been decreased in the interval $\Delta t = 1e^{-3} - 1e^{-5}$ s which has caused a change of results in ξ_+ for maximally 0.3%. The variation of the space increment Δx in range $1e^{-2} - 1e^{-4}$ µm caused the changes in ξ_+ up to 2.5%. For both parameters, decreasing the increment by a constant factor reduces the error successively.

Material parameters			
Receptor density on cell surface	ξ_0	1000	μm^{-2}
Receptor density on virus	ξ_{eq}	4800	μm^{-2}
Receptor mass	m_r	400	kDa
Mass of a receptor pair	m_{rr}	800	kDa
C_b-Parameter	C_b	5	–
Numerical bending stiffness parameter	B	30	–
Curvature of the virus	κ	40	μm^{-1}
Mobility parameter	m	0.5-1	$\mu m^2/s$
Virus diameter	D	0.05	µm

Table 2.1: Process parameters used in simulations.

The first group of simulations studies the change of the cell receptor density during the process and the front motion for the mobility parameter set to $m = 1\ \mu m^2/s$. The density profiles for different time steps during the simulation are presented in Fig. 2.3. The diagrams show a fast decrease in receptor density, particularely at the beginning of the process. After 300 time steps, the density at the front only amounts to $\approx 50\%$ of its initial value. This rapid decline in density at the front slows down in the course of the further process.

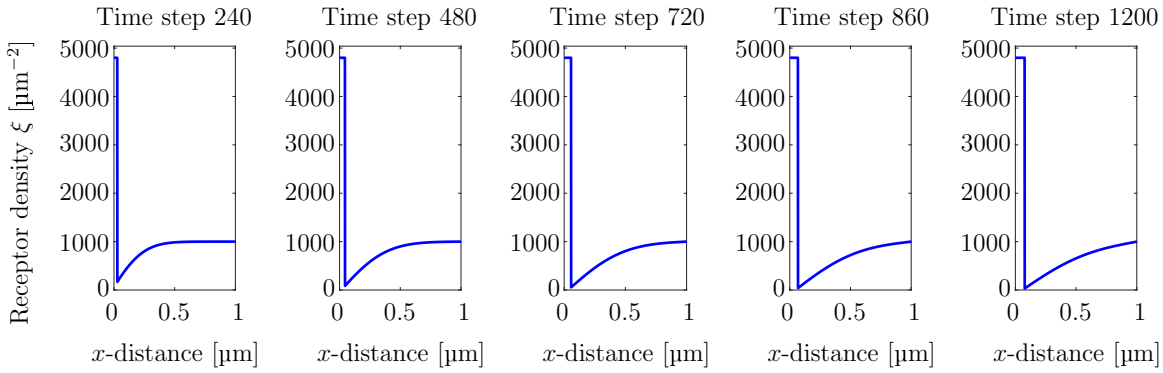

Figure 2.3: Receptor density ξ over the cell surface x for the first 1200 time steps, corresponding to a simulated time of 0.12 s.

Figure 2.4 monitors the advancement of the front and the position of the virus during its entry into the cell in 1D representation.

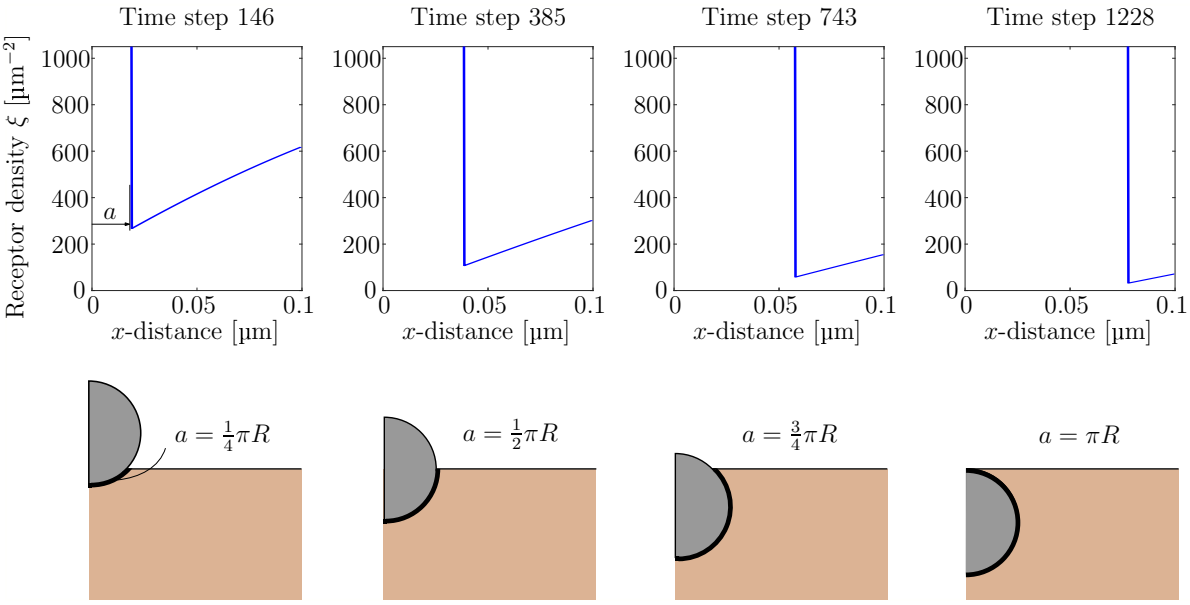

Figure 2.4: Visualization of the front motion and of the formation of the envelope around the virus with diameter $D = 0.05$ µm.

The position of the virus is related to the position of the front through length a, determining the size of contact area. For a helical virus, a 3D visualization is also possible due to the axial symmetry, as shown in Fig. 2.6 which compares the endocytosis of a virus into cells with different receptor mobilities.

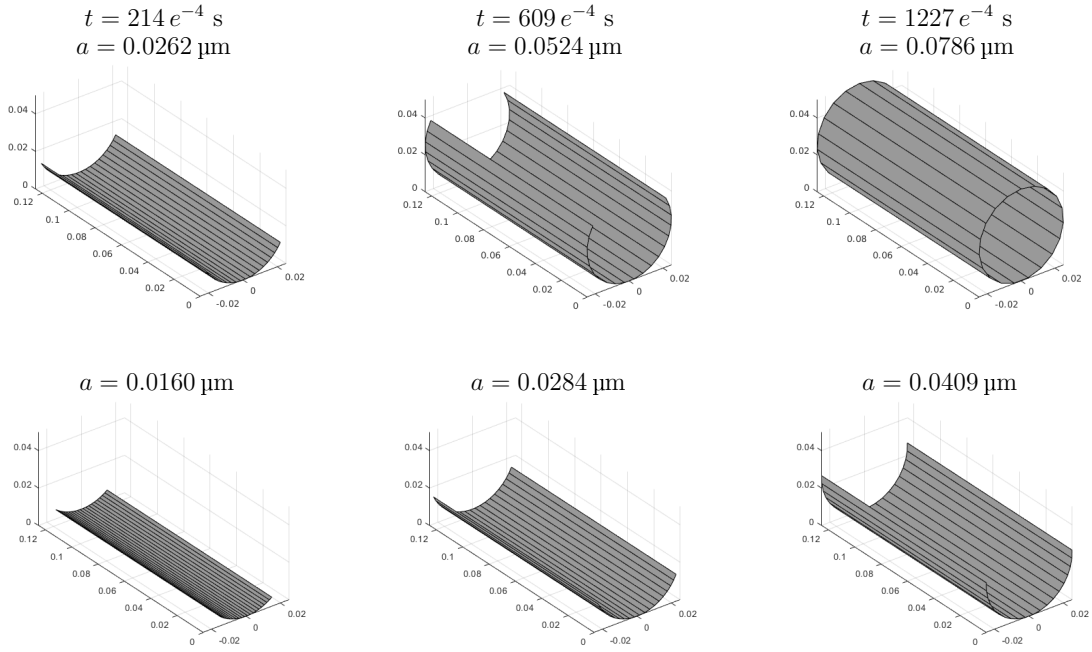

Figure 2.6: Endocytosis of a helical virus. Comparison of the process state at the same time for two different mobilities. The upper row shows results corresponding to a higher mobility $m = 1\,\mu\text{m}^2/\text{s}$. Results presented in the bottom row are related to lower mobility $m = 0.5\,\mu\text{m}^2/\text{s}$.

In the top row, the mobility is set to $m = 1\,\mu\text{m}^2/\text{s}$, whereas half of this value $m = 0.5\,\mu\text{m}^2/\text{s}$ is used in simulations in the lower row. Naturally, the first process is faster and the viral entry is accomplished earlier than in the second case. The increasing number of time steps between the three states indicates the gradual decrease and final stagnation of the velocity of the process, an issue also studied in the following example. The governing equation (2.3) of the process depends on a single process parameter, namely on mobility m. The parameter represents a measure for the capability of receptors to move over the cell surface, and thus is in a direct correlation with the amount of receptors provided for the adhesion with the virus. The influence of the mobility on the velocity of the front and on the receptor density has been studied on the basis of a set of simulations, as shown in Fig. 2.7.

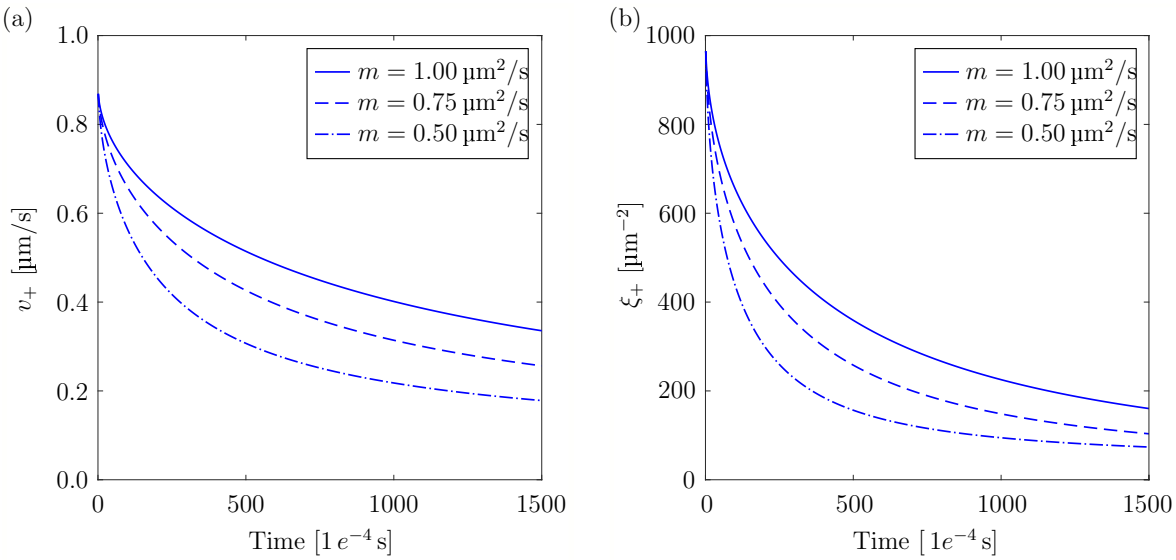

Figure 2.7: a) Velocity of the adhesion front vs. time. b) Evolution of the receptor density at the adhesion front. Mobility is varied in the range $0.5\,\mu m^2/s - 1\,\mu m^2/s$.

Here, mobility parameter m has been varied in the range [0.5 µm^2/s-1 µm^2/s]. Figure 2.7a shows the dependence of velocity v_+ on the mobility and clearly confirms the rapid decrease in velocity at the beginning followed by a stagnation, as already observed in the previous test (Fig. 2.4). The value of the mobility does not affect the form of the velocity diagrams. However, a higher velocity corresponds to a higher mobility. This observation is in agreement with the physical character of the mobility describing the ability of receptors to move towards the adhesion zone. For lower values of m, fewer receptors are provided to connect the cell with the virus. Therefore, the evolution of the adhesion zone and the velocity of the front are slowed down. An analogous trend is observed for the dependency of the receptor density at the front on the mobility shown in Fig. 2.7b.

An important influence on the process is also imposed by the fixed receptor density ξ_{eq} of the virus, initially chosen to dictate the amount of receptors required for the virus-cell connection. The velocity of the adhesion front v_+ for different values of ξ_{eq} is shown in Fig. 2.8a. Here, the receptor density of the cell is set to $\xi_0 = 1000\ \mu m^{-2}$ and the mobility is set to $m = 1\ \mu m^2/s$. The form of the velocity diagrams does not change, although the different constellations are taken into consideration. The velocity of the adhesion front v_+ decreases with increasing density ξ_{eq}, which is to be expected since a larger number of receptors is necessary in order to achieve a front advancement.

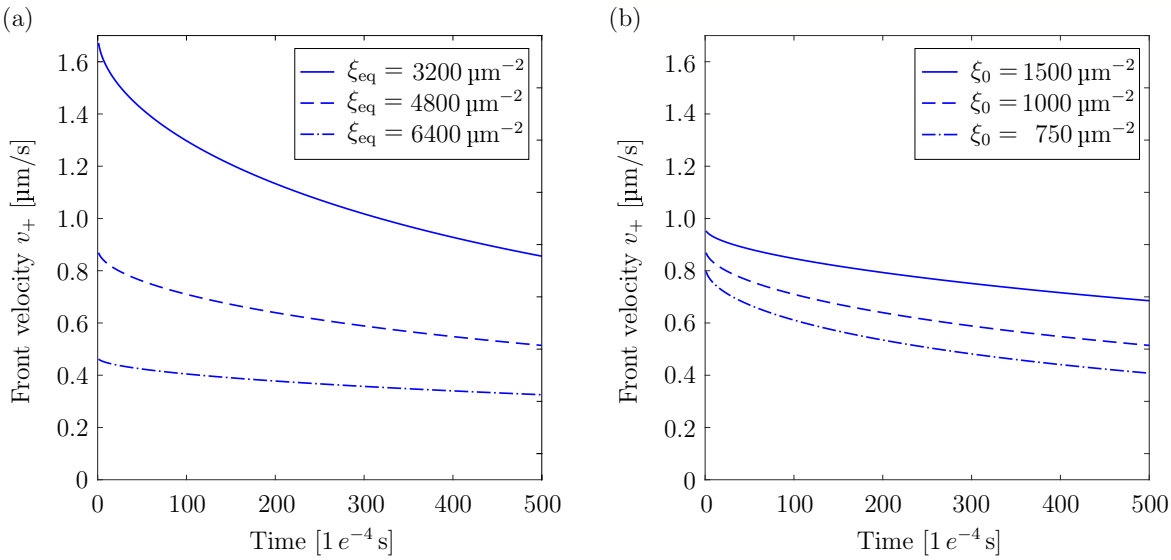

Figure 2.8: a) Evolution of the velocity of the adhesion front for different densities ξ_{eq}. Density ξ_0 is set to 1000 µm^{-2}. b) Evolution of the velocity at the adhesion front front for different initial densities ξ_0. Density ξ_{eq} is set to 4800 µm^{-2}.

Similar simulations are conducted for different values of the initial receptor density ξ_0, while the receptor density of the virus is set to $\xi_{eq} = 4800$ µm^{-2} (Fig. 2.8b). Again, the initial configuration does not affect the form of the diagrams, whereas a larger density ξ_0 corresponds to higher velocities. The required amount of connected receptors has been fixed at a constant value in all the simulations. However, only the initiation of the process requires a higher amount of bonds. Once contact between the cell and the virus has been established, the number of necessary receptors decreases. The amount of bonds required for the contact between the cell and the virus cannot fall below a minimum value. The evolution of the required cell receptor density can be easily implemented in the developed code by assuming ξ_{eq} to be a function of time. The simulations in this case (results not shown here) indicate an accelerated viral entry into the cell as a consequence of the decrease of the required receptor density.

2.6 Nondimensionalization

2.6.1 Derivation of the non-dimensional formulation

In some physical systems, non-dimensionalization is applied to suggest that it is more convenient to measure certain quantities relative to an appropriate unit. These units refer to quantities intrinsic to the system. The non-dimensionalization procedure relies on replacing dimensional quantities by the non-dimensional ones within the differential equation and within the corresponding boundary and supplementary conditions. An

important advantage of the non-dimensional analysis is that it reduces the number of relevant process parameters and thus facilitates the parameter study as performed in the previous section.

The present model for the viral entry includes following dimensional quantities which can be expressed in terms of their non-dimensional counterparts

$$x = l_\mathrm{s}\, x', \qquad t = \tau_\mathrm{s}\, t', \qquad \xi = \xi_\mathrm{s}\, \xi'. \tag{2.27}$$

Here, l_s, τ_s, ξ_s are properly chosen scaling parameters for space, time and density, and the prime symbol denotes the dimensionless quantities. The introduction of transformation (2.27) in differential equation (2.3) yields its non-dimensional form

$$\frac{\partial \xi'}{\partial t'} = \frac{m\,\tau_\mathrm{s}}{l_\mathrm{s}^2} \frac{\partial^2 \xi'}{\partial x'^2}. \tag{2.28}$$

The same procedure can now be applied to the flux-boundary condition (2.9) and the supplementary energy condition (2.24) which, amongst others, depend on front velocity v_+. The latter intrinsically includes the derivative with respect to time, which yields

$$v_+ = \frac{\partial a}{\partial t} = \frac{\partial (l_\mathrm{s}\, a')}{\partial (\tau_\mathrm{s}\, t')} = \frac{l_\mathrm{s}}{\tau_\mathrm{s}} v'_+. \tag{2.29}$$

Bearing in mind transformations (2.27) and intermediate result (2.29), the flux boundary condition and the energetic supplementary condition have the non-dimensional form

$$(\xi'_\mathrm{eq} - \xi'_+)\, v'_+ - \frac{m\,\tau_\mathrm{s}}{l_\mathrm{s}^2} \left[\frac{\partial \xi'}{\partial x'}\right]_+ = 0, \tag{2.30}$$

$$C'_1 - \xi'_+ \ln \xi'_+ - \frac{1}{2}\,\frac{m_\mathrm{r}}{k\,T}\,\frac{m^2}{l_\mathrm{s}^2}\,\frac{1}{\xi'_+} \left(\frac{\partial \xi'_+}{\partial x'}\right)^2 = \frac{1}{2}\,\frac{m_\mathrm{rr}}{k\,T}\,\frac{l_\mathrm{s}^2}{\tau_\mathrm{s}^2}\,\xi'_\mathrm{eq}\, v'^2_+, \tag{2.31}$$

where the following abbreviations apply

$$\xi'_+ = \frac{\xi_+}{\xi_\mathrm{s}}, \qquad \xi'_\mathrm{eq} = \frac{\xi_\mathrm{eq}}{\xi_\mathrm{s}}, \tag{2.32}$$

$$C'_1 = -\xi'_\mathrm{eq}\, C_\mathrm{b} + \xi'_\mathrm{eq} \ln \xi'_\mathrm{eq} + \frac{1}{2} B\, \frac{\kappa^2}{\xi_\mathrm{s}}. \tag{2.33}$$

Previous formulation (2.30)-(2.31) calls upon the introduction of additional non-dimensional process parameters

$$\overline{m} = \frac{m\,\tau_\mathrm{s}}{l_\mathrm{s}^2}, \qquad \overline{m}_\mathrm{r} = \frac{1}{2}\,\frac{m_\mathrm{r}}{k\,T}\,\frac{m^2}{l_\mathrm{s}^2}, \qquad \overline{m}_\mathrm{rr} = \frac{1}{2}\,\frac{m_\mathrm{rr}}{k\,T}\,\frac{l_\mathrm{s}^2}{\tau_\mathrm{s}^2}\,\xi'_\mathrm{eq}. \tag{2.34}$$

where $\overline{m}$ represents the dimensionless mobility, $\overline{m}_\mathrm{r}$ is the non-dimensional cell receptor mass and $\overline{m}_\mathrm{rr}$ the non-dimensional mass of a receptor couple. This short notation yields the final form of the non-dimensional moving boundary problem

$$\frac{\partial \xi'}{\partial t'} = \overline{m}\, \frac{\partial^2 \xi'}{\partial x'^2}, \tag{2.35}$$

$$(\xi'_\mathrm{eq} - \xi'_+)\, v'_+ - \overline{m} \left[\frac{\partial \xi'}{\partial x'}\right]_+ = 0, \tag{2.36}$$

$$C'_1 - \xi'_+ \ln \xi'_+ - \overline{m}_\mathrm{r} \frac{1}{\xi'_+} \left[\frac{\partial \xi'_+}{\partial x'}\right]^2 = \overline{m}_\mathrm{rr}\, v'^2_+ \,. \tag{2.37}$$

2.6.2 Analysis and results

After deriving the non-dimensional formulation of the problem, a further important step is choosing characteristic scaling parameters. Typically, these are adapted to the system properties. In the present case, half of the arclength of the virus is assumed as the characteristic length, namely $l_\mathrm{s} = \pi R$. On the other hand, the characteristic time is chosen as the time necessary to complete the virus uptake at a constant unit velocity $v_0 = 1 \frac{\mu\mathrm{m}}{\mathrm{s}}$. Accordingly, the time scaling parameter reads $\tau_\mathrm{s} = l_\mathrm{s}/v_0$. The initial cell receptor density is chosen as the last scaling parameter, such that it holds $\xi_\mathrm{s} = \xi_0$.

The results for a non-dimensional analysis are presented by examples investigating the influence of non-dimensional parameters $\overline{m}$, $\overline{m}_\mathrm{r}$, $\overline{m}_\mathrm{rr}$, C'_1 and ξ'_eq on the front velocity and front receptor density. To this end, first, the reference values for the scaling parameters are set as follows: $l_\mathrm{s} = \pi R = 0.0785\ \mu\mathrm{m}$ and $\tau_\mathrm{s} = l_\mathrm{s}/v_0 = 0.0785\ \mathrm{s}$. Here, radius $R = 0.025\ \mu\mathrm{m}$ is assumed as the reference virus size. The density scaling parameter takes the value $\xi_\mathrm{s} = \xi_0 = 1000\, \mu\mathrm{m}^{-2}$.

The results of the analysis parameter analysis are presented in Fig. 2.9. They show that the dimensionless mobility $\overline{m}$ has an important influence on the front velocity (Fig. 2.9a), whereas the dimensionless mass $\overline{m}_\mathrm{r}$ mainly influences the front receptor density (Fig. 2.9b). The variation of the dimensionless equilibrium density ξ'_eq has an important influence on both quantities (Fig. 2.9c). The effect of C'_1 is similar to the one of ξ'_eq, whereas the variation of the dimensionless couple mass $\overline{m}_\mathrm{rr}$ hardly affects the results (results not shown here). Amongst others, a higher mobility corresponds to the higher front velocity, whereas higher mass $\overline{m}_\mathrm{r}$ and equilibrium density ξ'_eq cause a higher front density.

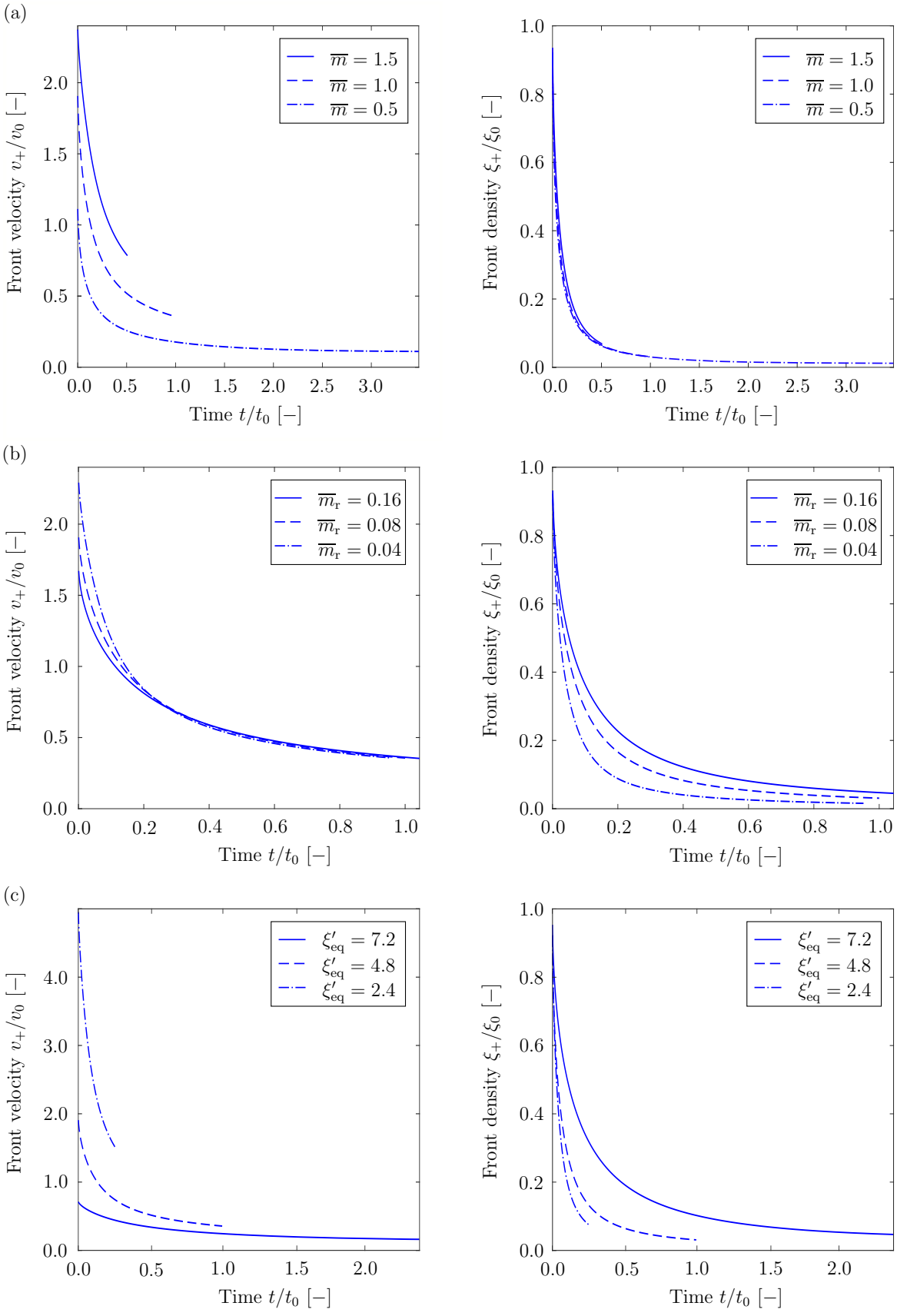

Figure 2.9: The non-dimensional analysis of the front velocity and the front density. (a) The influence of non-dimensional mobility $\overline{m}$. Remaining parameters are kept constant: $\overline{m}_\mathrm{r} = 0.08$, $\overline{m}_\mathrm{rr} = 0.78$, $C'_1 = 7.53$, $\xi'_\mathrm{eq} = 4.8$. (b) The influence of non-dimensional receptor mass $\overline{m}_\mathrm{r}$. Remaining parameters: $\overline{m} = 1.00$, $\overline{m}_\mathrm{rr} = 0.78$, $C'_1 = 7.53$, $\xi'_\mathrm{eq} = 4.8$. (c) The influence of non-dimensional equilibrium density ξ'_eq. Remaining parameters: $\overline{m} = 1.00$, $\overline{m}_\mathrm{r} = 0.08$, $\overline{m}_\mathrm{rr} = 0.78$, $C'_1 = 7.53$.

2.7 Rotationally symmetric case - Spherical virus

Whereas the previous analysis focuses on the 1D formulation applicable for the simulation of helical viruses, the real situation is commonly concerned with the rotationally symmetric geometry and spherical viruses. The problem formulation in this case is slightly different and requires an adaptation of the diffusion equation, whereas the boundary and supplementary conditions remain unchanged. The extension of the diffusion equation implies the introduction of an additional term compensating for the radial dependency. Thus, the differential equation turns into

$$\frac{\partial \xi}{\partial t} - m\frac{\partial^2 \xi}{\partial x^2} - m\frac{1}{x}\frac{\partial \xi}{\partial x} = 0, \tag{2.38}$$

where the last term on the left-hand side is the new contribution. The discretized counterpart of Eq. (2.38) is

$$\frac{\xi_i^{j+1} - \xi_i^j}{\Delta t} - m\frac{\xi_{i-1}^{j+1} - 2\xi_i^{j+1} + \xi_{i+1}^{j+1}}{\Delta x^2} - m\,\frac{1}{x}\,\frac{\xi_{i+1}^{j+1} - \xi_{i-1}^{j+1}}{2\,\Delta x} = 0, \tag{2.39}$$

where $i = 1, ..., p$ is the counter related to the spacial discretization and where $j = 1, ..., n$ is the counter corresponding to the time discretization. Variable x in the last term in (2.39) represents the distance from the first contact point and also can be written in a discretized form as $x = i\Delta\, x$, which leads to a condensed discretization formulation

$$\frac{\xi_i^{j+1} - \xi_i^j}{\Delta t} - \frac{m}{2i\,\Delta x^2}\left[(2i-1)\,\xi_{i-1}^{j+1} - 4i\xi_i^{j+1} + (2i+1)\,\xi_{i+1}^{j+1}\right] = 0\,. \tag{2.40}$$

Finally, the procedure explained in Sect. 2.6.1 provides the non-dimensinonal form of Eq. (2.38):

$$\frac{\partial \xi'}{\partial t'} - \overline{m}\,\frac{\partial^2 \xi'}{\partial x'^2} - \overline{m}\,\frac{1}{x'}\frac{\partial \xi'}{\partial x'} = 0\,. \tag{2.41}$$

The simulation of the virus uptake for a rotationally symmetric case is demonstrated by the example of the Alphavirus and by the process parameters summarized in Tab. 2.1. The achieved results are summarized in Fig. 2.10.

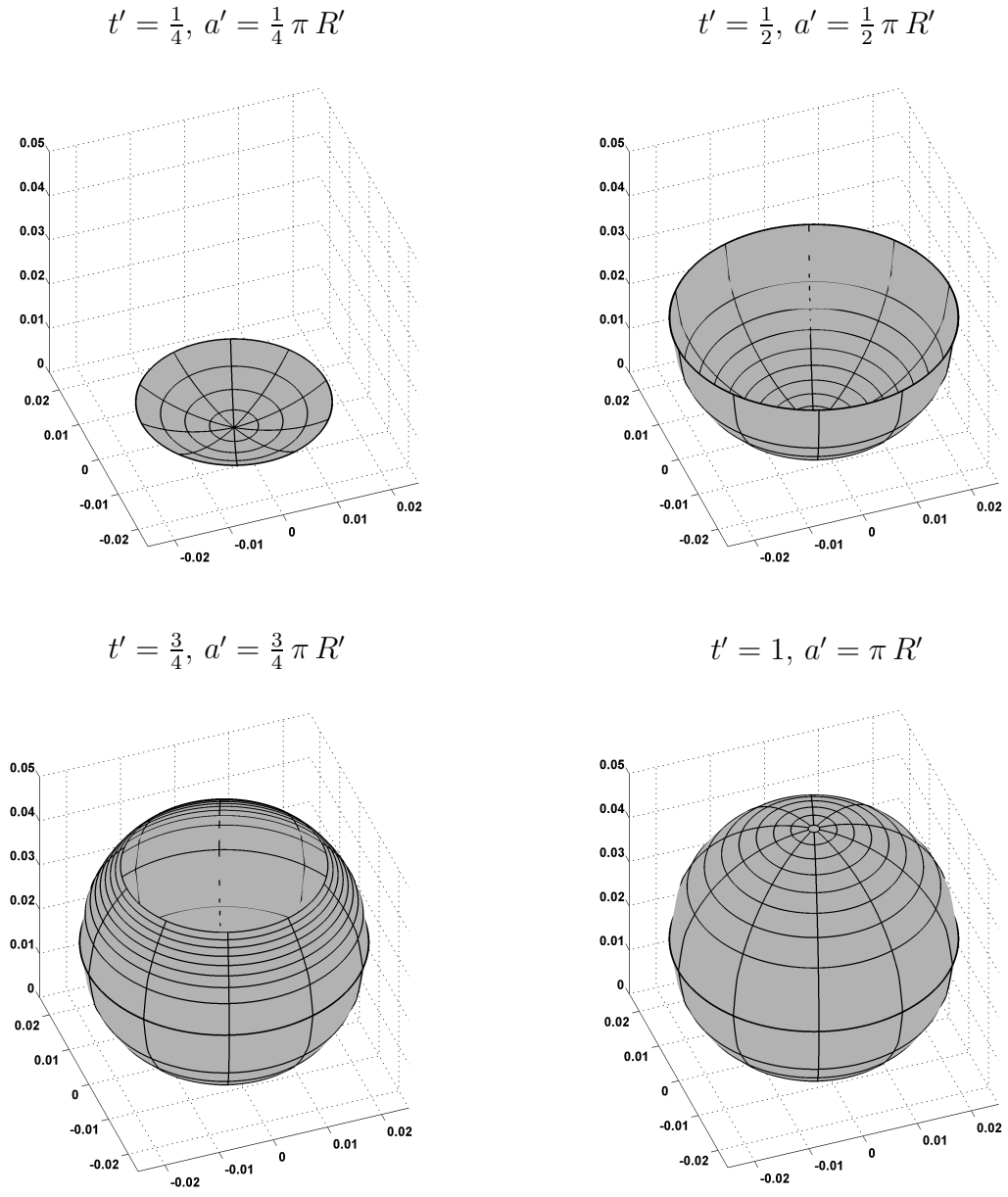

Figure 2.10: The 3D visualization of the endocytosis of a spherical virus with diameter $D = 0.05$ µm.

They show the 3D vesicle that is built during the process of the viral entry. Different to the endocytosis of a helical virus, the process advances at a rather constant rate throughout the simulation. This change in behavior can be explained by providing additional receptors due to the radial dependence. The same argumentation explains the higher velocity of the uptake process by a spherical virus compared to the helical one. For the chosen parameters, the simulations predict a required time in the range

for ultra-fast-endocytosis [152]. This fast behavior is expected, since the mobility has a rather high value. Viruses often connect to receptors with a lower mobility. By reducing mobility to $m = 0.2\ \mu m^2/s$ the time increases and matches values for kiss-and-run-endocytosis [166]. The model predicts a shorter duration of the process than it is typical of the clathrin-mediated-endocytosis (15-20 s) [17].

2.8 Cooperativity

Amongst others, cell adhesion deals with cooperativity, an effect which is explained by considering a patch of unit length depicted in Fig. 2.11.

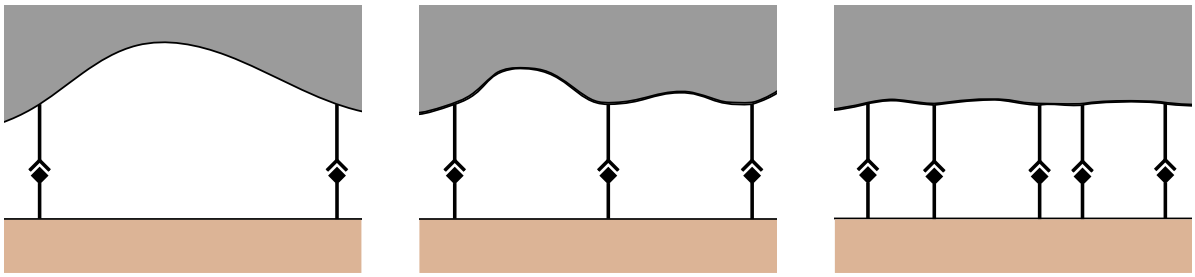

Figure 2.11: Schematic representation of cooperativity during endocytosis (the free receptors are not shown).

As soon as receptors create bonds, they smoothen out the surrounding membrane which makes it easier for additional receptors to create a bond and strengthens the adhesion between the virus and the cell membrane [94, 154]. This effect is known as cooperativity. It has extensively been investigated experimentally and theoretically. Different experiments are performed depending on the state of the adhesion process. The fluorescence recovery experiments are performed in order to analyze the equilibrated contact zone during the process, whereas the micropipette experiments are performed in order to analyze the initial contact. Lipid vesicles with anchored receptor molecules are often used in order to resemble important aspects of cell adhesion.

In order to study the binding cooperativity, two classes of numerical models are considered. The first class describes the membranes as continuous in space with continuous concentration profiles on the membrane [162]. The second class describes the membranes as discrete and the receptors as single molecules [93]. Numerical solutions of the dynamic properties are studied by reaction-diffusion equations in the first class [132] of models and by Monte Carlo simulations in the second class [145]. The information obtained in such a way is complementary to the model presented in this contribution.

The cooperativity changes the amount of receptor bonds that will create an equilibrium state upon connection between the virus and the cell given in [94] according to

$$\xi_{\mathrm{eq\_req}} = c\frac{\kappa_{\mathrm{b}}}{kT} l_{\mathrm{we}}^2 K_{\mathrm{pl}}^2 \xi_{\mathrm{eq}}^2 \xi_0^2. \tag{2.42}$$

Here, $\xi_{\text{eq\_req}}$ is the required amount of receptors that need to bind in order to create adhesion between the virus and the cell. Symbol c denotes a dimensionless prefactor acquired from Monte Carlo simulations, usually ranging between 10 - 15. Furthermore, the effective rigidity κ_{b} can be calculated from the bending rigidities of two apposing membranes as $\kappa_{\text{b}} = \kappa_1\,\kappa_2/(\kappa_1+\kappa_2)$. For the simulations here, it is set to $40\,k\,T$. Quantity l_{we} is the binding range depending on the interaction range of the two binding sites, of the flexibility of their molecules and of the membrane anchoring. It describes the difference between the smallest and the largest local membrane separation at which the receptors can bind. Quantity K_{pl} is the two-dimensional equilibrium constant in the case of two opposing planar, supported membranes within binding separation of the receptor-ligand bonds.

Two illustrative examples are performed in order to analyze the influence of cooperativity for different binding ranges. As in the previous example the initial receptor density of the cell is set to $\xi_0 = 1000\ \mu\text{m}^{-2}$ and the receptor density of the virus is set to $\xi_{\text{eq}} = 4800\ \mu\text{m}^{-2}$. The first group of simulations considers a virus with its lower half covered by receptors with a smaller binding range and its upper half by receptors with a larger binding range. The lower half is characterized by a binding range of $l_{\text{we}} = 1$ nm resulting in the required receptor density $\xi_{\text{eq\_req}} = 2265\ \mu\text{m}^{-2}$, while the upper half is characterized by a binding range of $l_{\text{we}} = 1.2$ nm resulting in the required receptor density $\xi_{\text{eq\_req}} = 3262\ \mu\text{m}^{-2}$. An opposite situation is considered in the second group of simulations presented in Fig. 2.12.

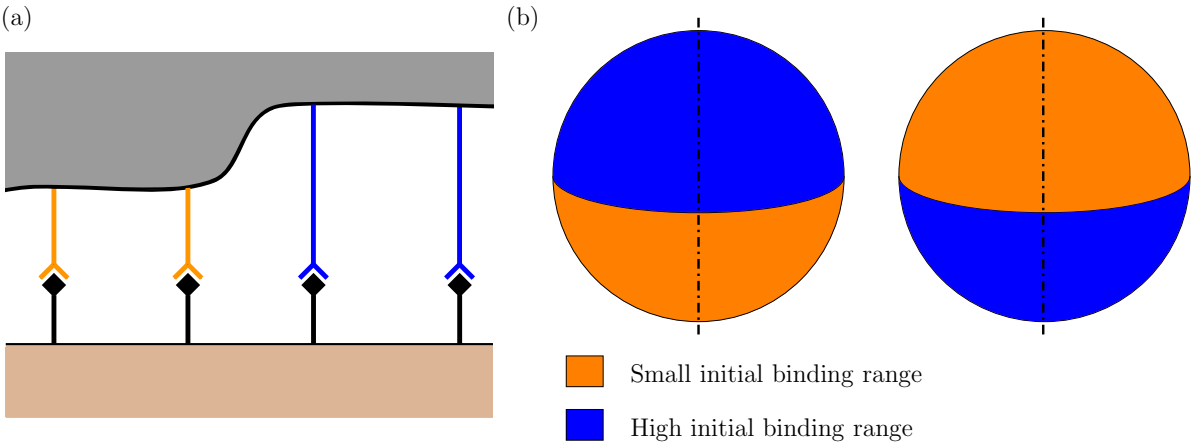

Figure 2.12: (a) Contact with the virus with two kinds of receptors. (b) Spatial distribution of different types of receptors on the virus membrane for two chosen configurations.

Numerical results for the described examples are shown in Fig. 2.13.

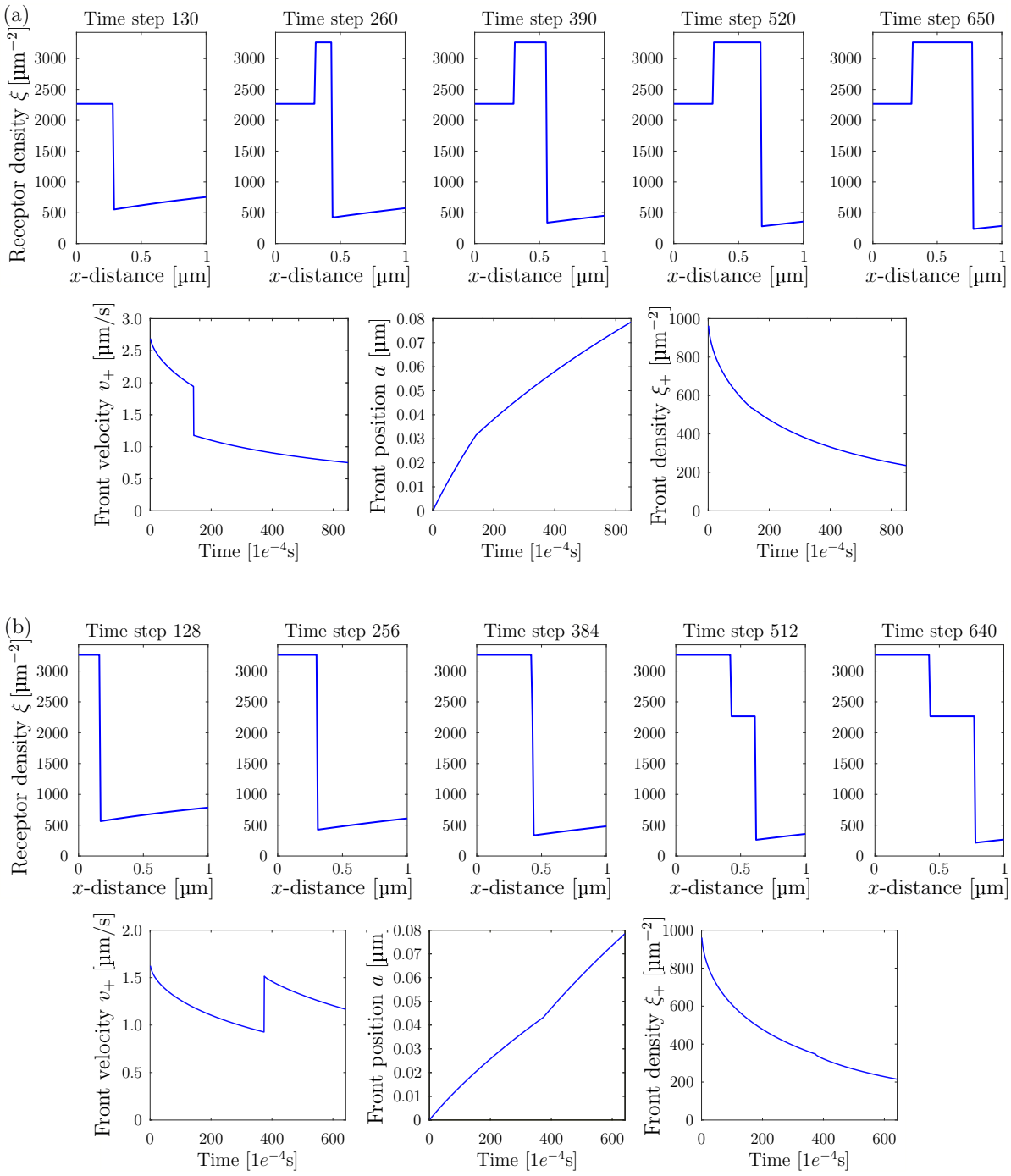

Figure 2.13: (a) Influence of the cooperativity for a smaller binding range in the lower half $\xi_{\text{eq\_req}} = 2265$ µm^{-2} and a larger one in the upper half $\xi_{\text{eq\_req}} = 3262$ µm^{-2}. (b) Influence of the cooperativity for a larger binding range in the lower half $\xi_{\text{eq\_req}} = 3262$ µm^{-2} and a smaller one in the upper half $\xi_{\text{eq\_req}} = 2265$ µm^{-2}. Top row: Receptor density over the cell surface for different time steps. Bottom row: Velocity of the front, position of the front and receptor density at the front over time. Chosen process parameters are $K_{\text{pl}} = 0.55\, e^{-3}$ and $c = 13$.

The transition between the areas with different receptor types manifests itself by either a jump or a kink in the corresponding diagrams. The velocity is affected mostly by the change of the required density. In the area with a smaller binding range less receptors are required, significantly increasing the velocity of the process. The diagrams for the second setup show similar results to the first setup, however, the change from the lower to the upper half is significantly delayed. Here, the initial velocity is much higher in the first case such that the virus is almost enclosed at the time step 400. Contrary to this, the velocity at the end of the process is higher in the second case. Consequently, both viruses need approximately 600 time steps for their entry into the cell. Exact values are 611 and 622 time steps for the first and second example respectively. The values do not exactly match due to the different velocities at the beginning of the process and due to the transition between regions with different receptors.

2.9 Discussion

The model developed gives insight into some specific features of the process and enables its profound analysis in the context of impeding and hindering the viral entry. Amongst others, it enables a study of the position of the front and its velocity during the process, an analysis of the admissible values for the radius and of the duration of the process depending on different process parameters. The study presented uses the parameters listed in Tab. 2.1, if not stated otherwise.

2.9.1 Front position and velocity

The position of the front and its velocity are two characteristic indicators of the viral entry, giving insight into the current state of the process and enabling the estimation of its total duration. The evolution of these indicators (Fig. 2.14) shows that the front advances continuously during the process, whereas its velocity decreases with the strongest decline in the beginning, and an almost constant value at the end of the simulation. Similar behavior is shown in the work by Freund und Lin [61].

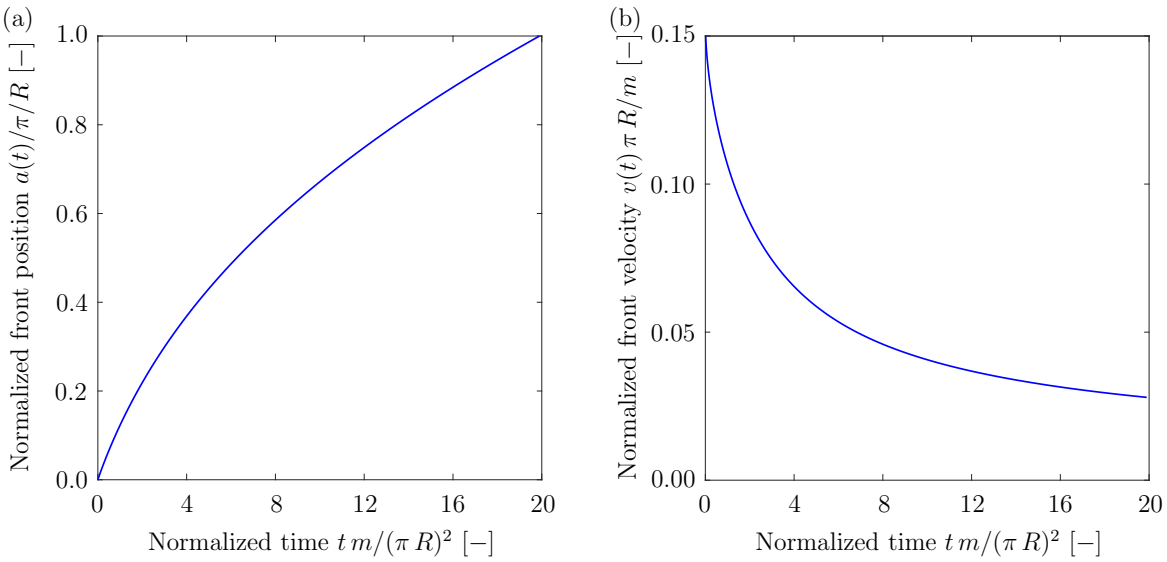

Figure 2.14: Normalized front position (a) and normalized front velocity (b) versus scaled time.

However, while the overall trends in both works are the same, some interesting phenomena can be identified with regard to the limiting behavior. The current model experiences a weaker decline in the velocity resulting in an almost constant velocity towards the end of the simulation, which yields a linear advancing of the front. However, the velocity in [61] moves towards zero which causes the process to experience almost no progress towards the end.

2.9.2 Virus radius

Apart from the front position and velocity, the virus radius also gives important information on the process, especially with regard to its initiation. This part of the analysis relies on the consequences of the energy balance (2.24). Since the right-hand side of this equation represents the kinetic energy, it directly follows that the difference between the energy behind and ahead of the front on the left-hand side has to be non-negative. In the beginning of the process, when the density distribution is uniform and the front has not yet been established, the energy ahead of the front does not contribute to the total amount. Therefore, the part of the energy behind the front can be seen as an initial barrier that must be overcome in order to start the process. A study of the limiting case, where the front velocity approaches to zero, yields the expression for the maximal radius

$$R_{\max} = \sqrt{\frac{B}{2}} \Bigg/ \sqrt{\xi_{\mathrm{eq}}\, C_{\mathrm{b}} - \xi_{\mathrm{eq}} \ln\left(\frac{\xi_{\mathrm{eq}}}{\xi_0}\right)} \tag{2.43}$$

under the condition that

$$C_\mathrm{b} - \ln\left(\frac{\xi_\mathrm{eq}}{\xi_0}\right) > 0. \tag{2.44}$$

By assuming the short notation for the receptor density ratio $\tilde{\xi} = \frac{\xi_0}{\xi_\mathrm{eq}}$, the value for the critical density ratio results in

$$\tilde{\xi}_\mathrm{crit} = e^{-C_\mathrm{b}}. \tag{2.45}$$

It is important to mention that the receptor density ratio is limited from both sides. On one hand, it holds $\tilde{\xi} = \frac{\xi_0}{\xi_\mathrm{eq}} \leq 1$ since $\xi_0 \leq \xi_\mathrm{eq}$. On the other hand, it holds $\tilde{\xi} > \tilde{\xi}_\mathrm{crit}$ due to the condition (2.44). The expressions (2.43) and (2.45) are now used to study the values of maximum radius. These results are shown in Fig. 2.15a, where the receptor density ratio is varied in the admissible semi-open range $(\tilde{\xi}_\mathrm{crit}, 1]$.

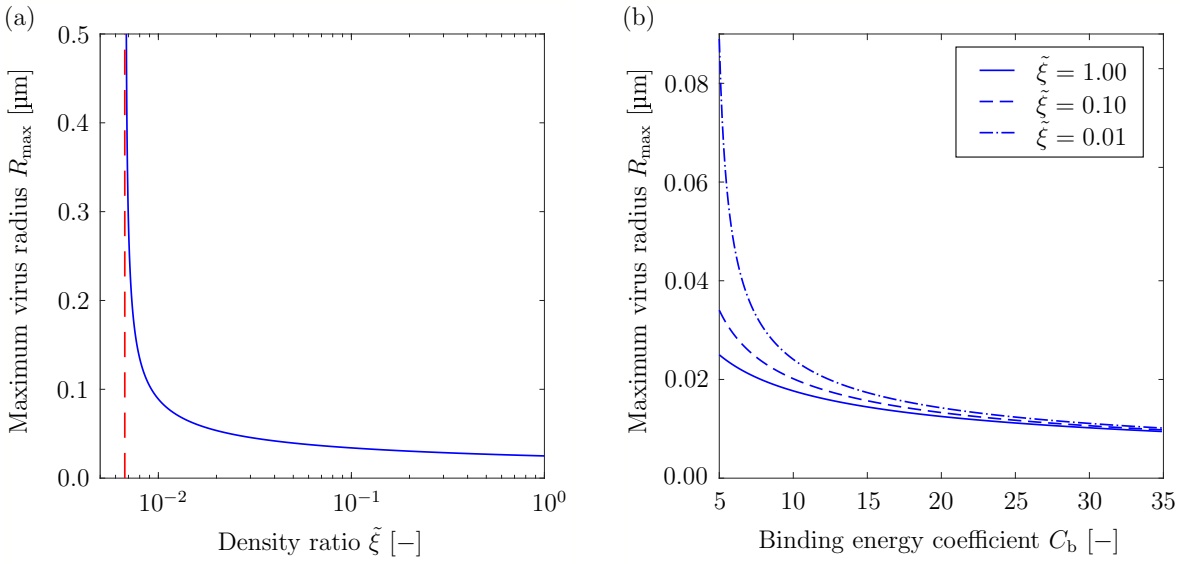

Figure 2.15: (a) Maximum virus radius versus receptor density ratio $\tilde{\xi}$. The vertical dashed line represents the critical value $\tilde{\xi}_\mathrm{crit}$. (b) The maximum virus radius versus the binding energy coefficient C_b for different receptor density ratios $\tilde{\xi}$.

Here, the red dashed line indicates the critical value $\tilde{\xi}_\mathrm{crit}$ according to Eq. (2.45). The correlation between the radius and the density ratio has also been studied in the works by Gao et al. [62]. They derive similar expressions for the limiting radius and the critical density ratio, however, their model provides the expression for the minimal radius. In the present study as well as in [62], the maximum radius increases rapidly as $\tilde{\xi}$ approaches its critical value. This quantity (2.43) also depends on the binding energy coefficient C_b which is studied in Fig. 2.15b for three different values of the receptor density ratio. Here, the lower line corresponds to the higher ratio ($\tilde{\xi} = 1$), and the

upper line to the lower ratio ($\tilde{\xi} = 0.01$). Whereas a noticeable difference of the radius is to be seen for smaller values of C_b, which becomes less pronounced as its value increases.

2.9.3 Entry duration

A significant aspect of the virus entry is the duration of the complete process as well as its dependence on different process parameters. The viral uptake via endocytosis ranges through different time scales. Ultra-fast-endocytosis takes 50-300 ms [152], while kiss-and-run-endocytosis takes approximately 1 s [166]. In the presented model, several parameters have a significant influence on the required time for the process. Three major parameters are the radius of the virus, the receptor density ratio and the mobility of the receptors. Figure 2.16 shows the influence which each of these parameters has on the required time. The influence of the radius (Fig. 2.16a) is analyzed for three different density ratios.

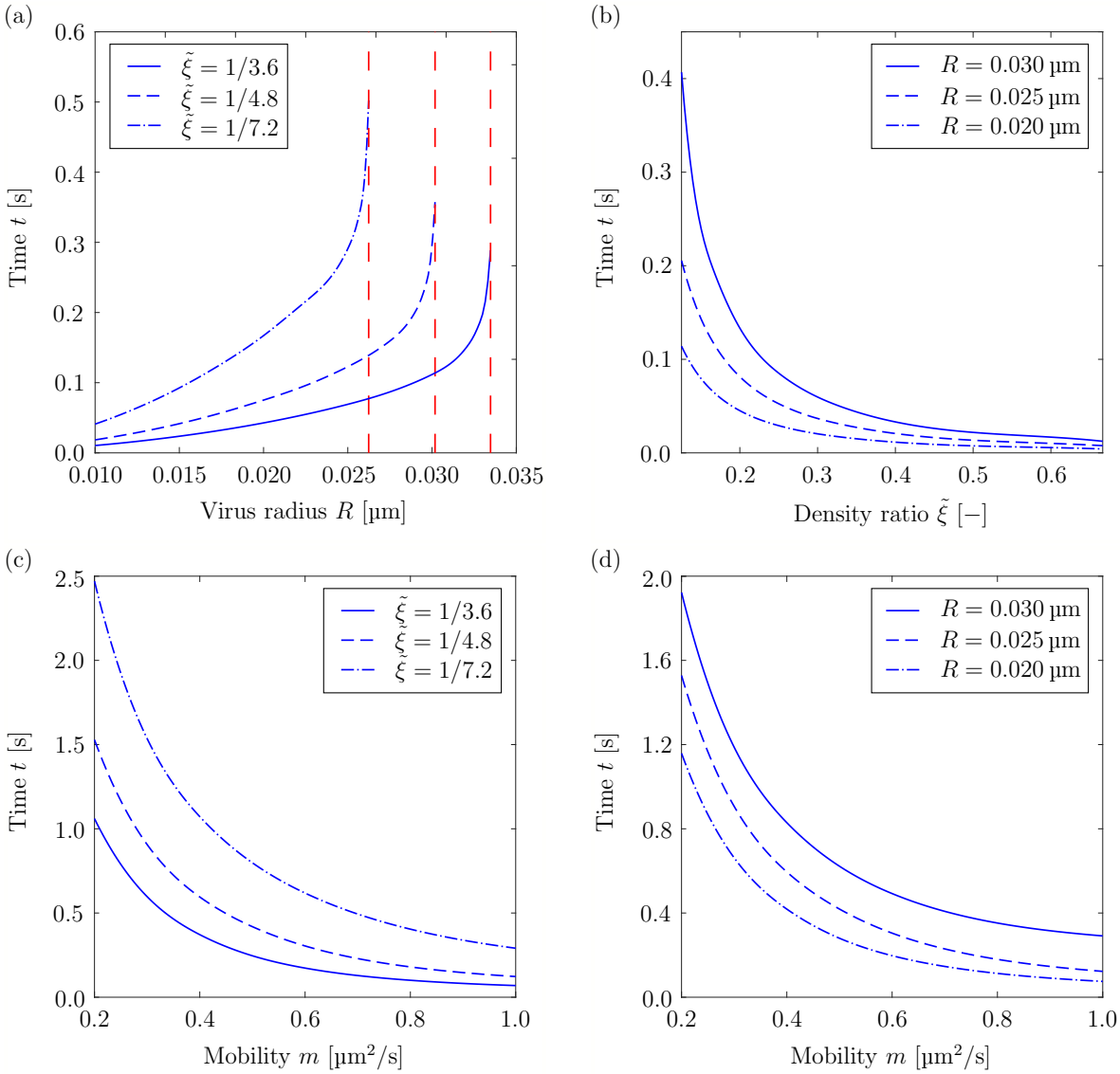

Figure 2.16: (a) Duration of the process depending on the virus radius for different receptor density ratios $\tilde{\xi}$. Vertical dashed lines indicate the maximum radii for particular critical receptor density ratios. (b) Duration of the process dependent on the receptor density ratio $\tilde{\xi}$ for different virus size R. (c) Process duration versus mobility parameter m for different receptor density ratios $\tilde{\xi}$. (d) Process duration versus mobility m for different virus size R.

The red dashed lines correspond to the maximum radius determined according to Eq. (2.43). All curves show an increasing trend with the highest value for the maximum radius. The curve with a smaller value for $\tilde{\xi}$ indicates an increase in time, due to the higher difference in the receptor density available and required. In Fig. 2.16b, the time depending on the density ratio for different radii is shown. A longer process time is

required for larger radii. The difference between the curves is small for larger ratios and becomes more significant as the ratio becomes smaller.

Finally, Fig. 2.16c and 2.16d both show the influence of the mobility on the required time. The curves in Fig. 2.16c corresponds to different density ratios and indicate that lower density ratios are related to the higher time requirements. The difference between the curves for the different densities is more pronounced as the mobility takes smaller values. A similar behavior is presented in Fig. 2.16d, where the curves correspond to different radii. In both cases a decrease in the mobility causes an increase in the required time, which can be expected since a larger m enables the receptors to move more rapidly to the adhesion zone. An analysis of the influence of the radius and of the density ratio to the required time is also presented in the works by Gao et al. [62]. This research group also shows a strong increase in the required time for an increasing radius but proposes a minimum value for the radius. Furthermore, contribution [62] shows a rapid increase in the required time when the radius comes close to the minimum value, whereas the current model does not predict such a behavior. Similar to the results which are shown in Fig. 2.16b, Gao et al. [62] observe a strong decrease in the required time for decreasing density ratios with an upper limit at $\tilde{\xi} = 1$.

2.9.4 Cooperativity

A more comprehensive study of the uptake process also requires the data on cooperativity (Sec. 2.8) to be included in the model. The influence of this factor is demonstrated on the basis of two examples dealing with the effects of the binding range l_{we}. The required receptor density Eq. (2.42) in combination with the equation for the radius Eq. (2.43) provides a relation between the binding range and the limiting radius. The corresponding results are presented in Fig. 2.17a where the single curves are related to different receptor densities of the virus.

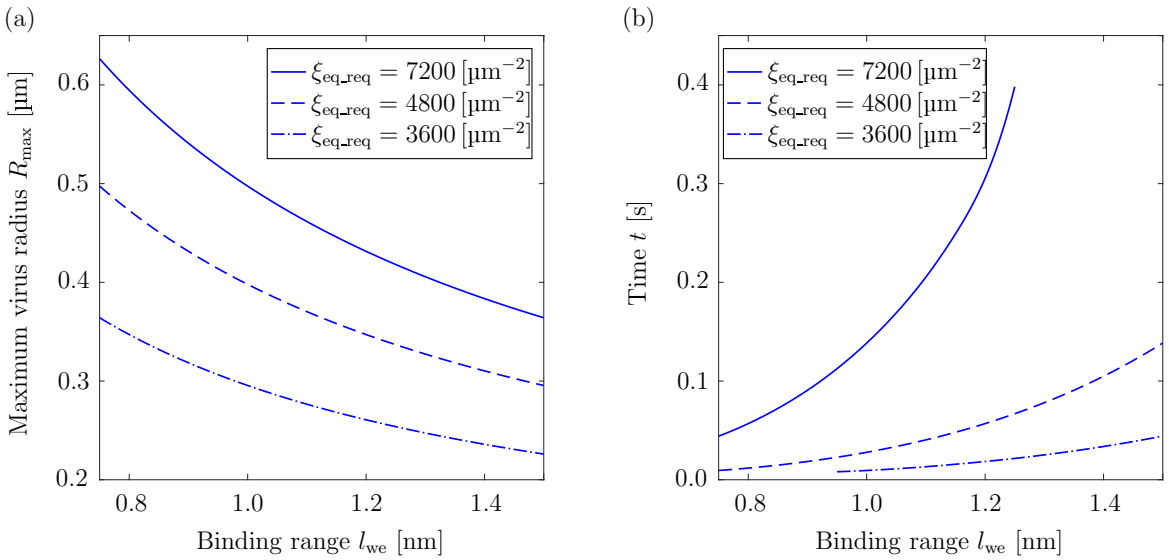

Figure 2.17: (a) Maximal virus radius depending on the binding range l_{we} for given required receptor density ξ_{eq_req}. (b) Process duration depending on the binding range l_{we} for given required receptor density ξ_{eq_req}.

As already shown in Fig. 2.8b, a smaller receptor density of the virus benefits the process, resulting in a larger possible radius.

Furthermore, the influence of the binding range l_{we} on the required density (2.42) and indirectly on the duration of the process is presented in Fig. 2.17b. Again, the three curves correspond to different receptor densities of the virus. For the upper curve, corresponding to $\xi_{eq} = 7200$ µm^{-2}, a large binding range hinders the begin of the process, since the required density ξ_{eq_req} becomes to be too high. On the contrary, the lower curve corresponding to $\xi_{eq} = 3600$ µm^{-2}, shows a lower threshold for the process to take place. Here, the duration of the process strongly depends on the binding range itself and prefers lower values in order to complete the process quickly. However, for an extremely small l_{we}, the number of virus and cell receptors coming into contact is not sufficient and the process cannot start.

2.9.5 Interaction of selected parameters

The discussion of results closes by presenting the interaction of selected process parameters and their influence on the initiation and duration of the process. Figure 2.18a shows the combination of the initial receptor density ξ_0 and mobility m, and shows a strong increase in the required time for the parameters chosen.

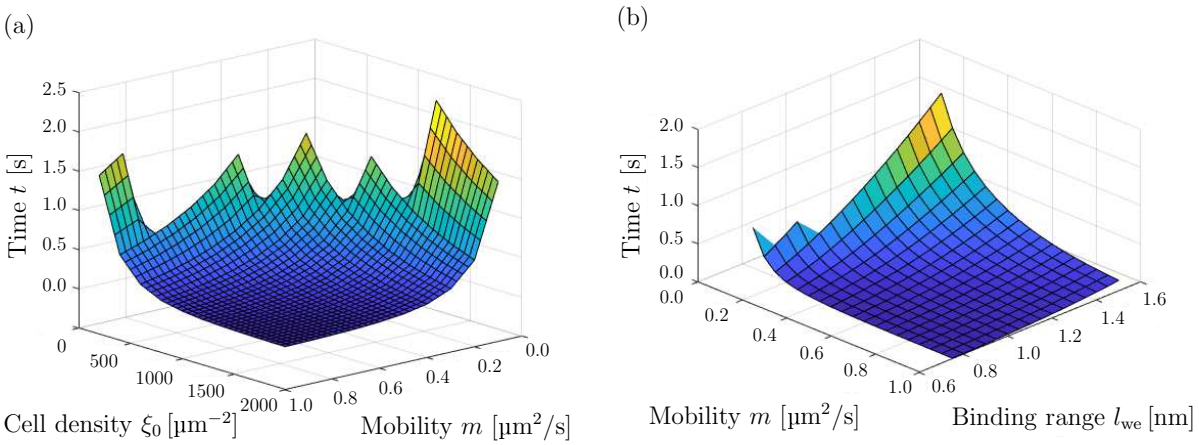

Figure 2.18: (a) Process duration depending on mobility m and the initial receptor density ξ_0. (b) Process duration depending on mobility m and the binding range l_{we}. Plots also show the admissibility ranges for chosen parameter sets.

If both parameters take small values, the process does not start, but once this threshold is surpassed the required time drops rapidly regardless of which parameter is changed. Especially the area with small values for the mobility is interesting, since it is not uncommon for viruses to attach to cell receptors with small mobilities. Some typical examples are the HIV-virus connecting to a receptor with mobility $m = 0.05$ µm^2/s [64] or the Semliki Forest virus connecting to a receptor with $m = 0.01$ µm^2/s [62].

Finally, Fig. 2.18b shows a range of combinations for mobility m and binding range l_{we} in which the process takes place. The influence of the binding range on the required time is weak, compared to the influence of the mobility, and becomes more noticeable for smaller values of the mobility.

2.10 Conclusion and outlook

The present study focuses on the investigation of the viral entry driven by the receptor diffusion using the finite difference method as simulation technique. An approach based on the consideration of the energetic aspects yields a formulation providing a well-posed description of the endocytosis process. The motion of the receptors is described by the diffusion differential equation accompanied by two boundary conditions dealing with the flux balance at the ends of the considered area. In addition, a supplementary condition is introduced to define the energy balance at the adhesion front.

The model developed shows several important features: the definition of the supplementary condition only depends on the quantities at the front, and the numerical simulation of the problem bypasses the introduction of assumptions typical of an analytical solution. The approach is highly efficient with regard to time and computer capacity, such that a fast simulation of different scenarios and a profound study of process parameters are possible. Here, the influences and the interaction of mobility,

receptor densities, virus size and receptor cooperativity play a central role. Their analysis, for example, yields data on the admissible regions, the upper limit of the size of the virus able to enter the cell and the estimation of the process duration. Amongst others, the analysis shows that the process duration strongly increases when a virus size approaches a critical value and that extremly high and low values of binding range have an impeding influence on the process initiation.

The results presented in this work pertain to a helical and a spherical virus penetrating a flat cell surface, which enables the taking of advantage of the axial and rotational symmetry and perform simulations in a two dimensional setup. However, an extension to a three dimensional setup has to be taken into account in order to analyze the receptor distribution for a non-spherical virus or a non-homogeneous receptor density of the cell. Furthermore, additional contributions, for example, caused by bending of the cell ahead of the front, can be considered in the energetic supplementary condition. Alternative expressions for bending lipid bilayers can also be introduced in order to carry out more realistic simulations.

3 Shell element embedded into an IGA framework

This chapter cites the paper "Non-linear thermo-mechanical modeling of hollow sphere shells using isogeometric analysis" by T. Wiegold, P. Kurzeja, S. Klinge, J. Mosler.

Abstract

Isogeometric analysis is employed in a finite-element framework to analyze the thermo-mechanical response of curved shells. A mathematical formulation is first derived from the generalized viewpoint of deformational mechanics with higher gradients and then linked to classic shell theory. This formulation extends classic shell theory, since it also covers additional deformation modes such as those related to in-plane gradient-elasticity. The finite element formulation of this model is based on the isogeometric analysis in combination with NURBS and especially allows an accurate representation of curved geometries. The first numerical example is a single hollow thermo-elastic sphere. Various transient thermal and mechanical boundary conditions trigger deformation modes that range from kinks to oblate shapes and wrinkles. Two sintered hollow spheroids are then used as a representative minimal system for hollow-sphere structures that are known for their opportunities in light-weight design and thermal insulation. Sinter radius and spheroid (aspect) radius can distinctively tune density, stiffness and thermal conduction, which mainly depends on whether wall stretching or bending dominates. While the isogeometric analysis remains beneficial to accurately capture the curved features, the spheroids' two principal curvatures and the curvature of the sinter area yield competing requirements for the resolution of the isogeometric discretization.

3.1 Introduction

The present work aims at utilizing isogeometric analysis for the thermo-mechanical, nonlinear description of shells by the example of sintered hollow spheres. The numerical modeling of shells is a key challenge in engineering that covers, amongst others, light-weight design, composite strength and instability problems [5, 38]. Shell structures are moreover ubiquitous in engineered and biological systems, e.g., involving solid and fluid

mechanics [125], the human blood cell [37], lipid bilayers [72] or gas bubble acoustics [73]. The present focus will be on nonlinear solid elasticity coupled to temperature as an extra field. It motivates the example of sintered hollow spheres, as their high porosity allows light weight and their large interfacial areas — sintered and free ones — determine their elastic and thermal performance [96]. They can be produced from metals and alloys by powder metallurgical processes [87], can be embedded in a host matrix [11] or appear in jetting of microspheres [141]. The thin walls of hollow sphere structures moreover allow for a higher range of elastic deformation than their bulk counterparts.

The mathematical description of shells yielded well-established models that are now also found as derivations in a new context, for instance, shells of Kirchhoff-Love type in a Cosserat framework [138] or Koiter-type shells from the viewpoint of nonlinear elasticity [136]. Accordingly, the present treatise also aims at connecting two research streams with typically different notations, i.e., the deformation measures of stretching and bending in classic shell theory as well as more general higher-gradient deformational mechanics. This connection shall support the understanding of the different formalisms and their own contributions to the scope of shell modeling [63, 79, 80, 124, 126]. Furthermore, the analogies between the different frameworks – shell theory vs. higher-gradient continuum models – highlight the intrinsic assumptions of classic shell theories and also show consistent extensions of them.

Several possibilities emerged for the numerical modeling of mechanical interfaces and shells in particular. Most notably are special shell elements in nonlinear finite element simulations [23, 39, 75] that complement the scope of applications covered by diffuse interface models [20, 158], level-set descriptions [165], fracture evolution [57] and general/imperfect interfaces [71, 81]. A very promising variant for shells has been established in the form of isogeometric analysis (IGA). It mostly uses shape functions of Non-Uniform Rational B-Splines (NURBS) that can provide a very accurate description of curved shapes and enables C^1-continuity across element boundaries. This is particularly usefull for shells with prominent curvature features. While NURBS were already established [118] and commonly used in computer aided design for some time, IGA was first introduced in [76]. A comprehensive overview can be found in [114]. IGA has already been analyzed and applied for a variety of applications involving spheres, such as large deformation contact problems [45], non-linear anisotropy [127], phase-field models [21] with damage [120], inflation [126] and lipid bilayers [124], to name a few.

With the promising IGA approach at hand, the present goal is the extension towards a consistent nonlinear, thermo-mechanically coupled framework. Adding the temperature field to the mechanical behavior shall explore new possibilities for the numerically efficient description of systems with complex curvature and temperature evolution. This is tested for the example of sintered hollow sphere structures that combine the challenges of thin walled, curved geometries with applications in light-weight, high-strength design and thermal insulation. The novel aspects particularly include:

- a thermo-mechanically coupled framework embedded into an IGA environment

- derivation of the shell formulation from higher-order deformational mechanics
- analysis of the non-linear response of single hollow spheres to various thermo-mechanical boundary conditions
- evolution of a generalized sinter process considering early-stage necking
- thermo-elastic parameter study of two sintered spheroids

The kinematics as well as the balance laws for the underlying problem are derived first from higher-order deformational mechanics in Chapter 3.2. The prototype material model and its constitutive relations are then presented in Chapter 3.3. Chapter 3.4 highlights the framework for the finite element method (FEM) as well as the calculation of the shape functions and their derivatives in context of IGA. Numerical examples of a single and two sintered, hollow spheroids are presented in Chapter 3.5 with respect to their thermo-elastic response to different transient loads. Chapter 3.6 concludes with implications for the IGA modeling technique and the sintered system.

3.2 Kinematics and balance laws

This section summarizes the kinematics as well as the balance laws suitable for the modeling of thin hollow spheres. While a geometrically exact description for shells undergoing finite stretching and bending is presented in Subsection 3.2.1, the balance laws associated with a thermomechanically coupled setting are provided in Subsection 3.2.2. Particular attention is paid to the differences and similarities between classical shell theory and higher-order constitutive models [81], where the second gradient of the deformation mapping is also included in the (Helmholtz) energy.

3.2.1 Kinematics

3.2.1.1 Geometry of a shell

In the following, the hollow spheres to be analyzed are geometrically approximated as two-dimensional manifolds embedded in the three-dimensional Euclidean surrounding space, i.e., as shells. Accordingly, they can be described by curvilinear coordinates ξ^α with $\alpha = 1, 2$, see Fig. 3.1. For instance, points belonging to the undeformed configuration $\mathcal{S}_0$ are parameterized as

$$\boldsymbol{X} = \boldsymbol{X}\left(\xi^\alpha\right) \in \mathcal{S}_0, \tag{3.1}$$

while their counterparts in the deformed configuration $\mathcal{S}$ are

$$\boldsymbol{x} = \boldsymbol{x}\left(\xi^\alpha\right) \in \mathcal{S}. \tag{3.2}$$

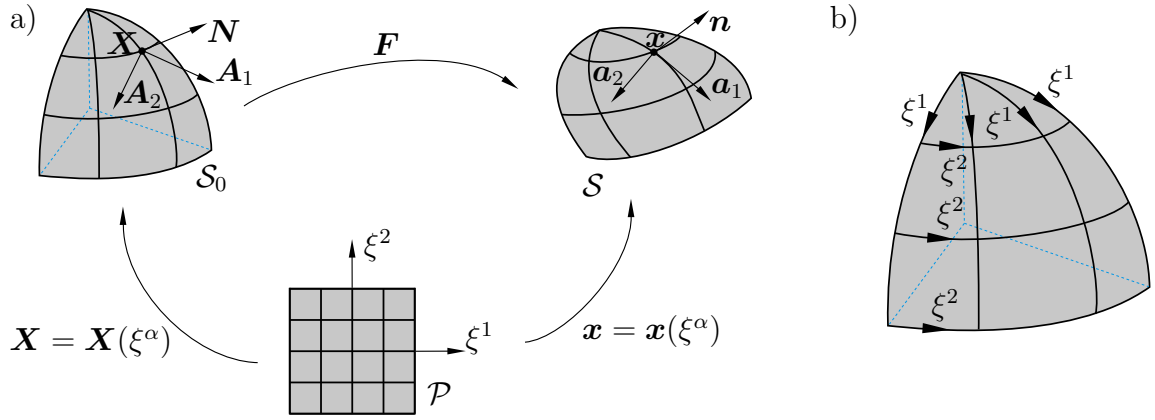

Figure 3.1: a) Mapping between the reference configuration $\mathcal{S}_0$ and current configuration $\mathcal{S}$. The curvilinear coordinates describing the shell are defined in the parameter space $\mathcal{P}$. b) Representation of the curvilinear coordinates projected onto the 3D euclidean space.

As a consequence, a specific material point can be uniquely identified by its coordinates ξ^α. Based on Eqs. (3.1) and (3.2) co-variant tangent vectors

$$\boldsymbol{A}_\alpha := \frac{\partial \boldsymbol{X}}{\partial \xi^\alpha} =: \boldsymbol{X}_{,\alpha}, \qquad \boldsymbol{a}_\alpha := \frac{\partial \boldsymbol{x}}{\partial \xi^\alpha} =: \boldsymbol{x}_{,\alpha} \tag{3.3}$$

can be introduced. Their dual contra-variant counterparts $\boldsymbol{A}^\alpha$ and $\boldsymbol{a}^\alpha$ are defined in standard manner, i.e., by

$$\boldsymbol{A}^\alpha \cdot \boldsymbol{A}_\beta = \delta^\alpha_\beta, \qquad \boldsymbol{a}^\alpha \cdot \boldsymbol{a}_\beta = \delta^\alpha_\beta \tag{3.4}$$

where δ^α_β is the Kronecker-delta. Finally, the normal vectors $\boldsymbol{N}$ on $\mathcal{S}_0$ and $\boldsymbol{n}$ on $\mathcal{S}$ are computed as

$$\boldsymbol{N} = \frac{\boldsymbol{A}_1 \times \boldsymbol{A}_2}{||\boldsymbol{A}_1 \times \boldsymbol{A}_2||} \qquad \text{and} \qquad \boldsymbol{n} = \frac{\boldsymbol{a}_1 \times \boldsymbol{a}_2}{||\boldsymbol{a}_1 \times \boldsymbol{a}_2||}. \tag{3.5}$$

Since shells — and the hollow spheres to be analyzed in this paper — can be subjected to either stretching or bending, measures for the curvature are also introduced. One such measure is the second-order curvature tensor. Depending on the configuration under consideration, this tensor reads either

$$\boldsymbol{B} = \underbrace{[\boldsymbol{N} \cdot \boldsymbol{A}_{\alpha,\beta}]}_{=: B_{\alpha\beta}} \boldsymbol{A}^\alpha \otimes \boldsymbol{A}^\beta \quad \text{or} \quad \boldsymbol{b} = \underbrace{[\boldsymbol{n} \cdot \boldsymbol{a}_{\alpha,\beta}]}_{=: b_{\alpha\beta}} \boldsymbol{a}^\alpha \otimes \boldsymbol{a}^\beta. \tag{3.6}$$

Again, $(\bullet)_{,\alpha}$ denotes the partial derivative of $(\bullet)$ with respect to coordinate ξ^α. Accordingly,

$$\boldsymbol{A}_{\alpha,\beta} := \frac{\partial \boldsymbol{A}_\alpha}{\partial \xi^\beta} = \boldsymbol{X}_{,\alpha\beta} = \boldsymbol{A}_{\beta,\alpha} \quad \text{and} \quad \boldsymbol{a}_{\alpha,\beta} := \frac{\partial \boldsymbol{a}_\alpha}{\partial \xi^\beta} = \boldsymbol{x}_{,\alpha\beta} = \boldsymbol{a}_{\beta,\alpha}. \tag{3.7}$$

3.2.1.2 Deformation of a shell

The deformation map $\boldsymbol{\varphi}$ connects material point ξ_0^α from the undeformed reference configuration $\boldsymbol{X}(\xi_0^\beta)$ to its deformed counterpart $\boldsymbol{x}_0(\xi_0^\beta)$. Based on Eqs. (3.1) and (3.2), one thus may write

$$\boldsymbol{\varphi} = \boldsymbol{x} \circ \boldsymbol{X}^{-1} \tag{3.8}$$

where $\boldsymbol{X}^{-1}$ is the inverse function of Eq. (3.1) and $\circ$ denotes the composition of functions. Line elements are mapped between both configurations by the deformation gradient

$$\boldsymbol{F} = \frac{\partial \boldsymbol{x}}{\partial \xi^\alpha} \otimes \frac{\partial \xi^\alpha}{\partial \boldsymbol{X}} = \boldsymbol{a}_\alpha \otimes \boldsymbol{A}^\alpha =: \mathrm{GRAD}_{\mathcal{S}_0} \boldsymbol{x}. \tag{3.9}$$

$\boldsymbol{F}$ is a rank-2-tensor that maps only tangent vectors. Evidently, $\boldsymbol{F}$ is the surface gradient of $\boldsymbol{x}$. In order to capture bending effects, the gradient of the deformation gradient

$$\begin{aligned} \mathbb{F} := \boldsymbol{F}_{,\beta} \otimes \boldsymbol{A}^{\beta} &= \boldsymbol{a}_{\alpha,\beta} \otimes \boldsymbol{A}^{\alpha} \otimes \boldsymbol{A}^{\beta} + \boldsymbol{a}_{\alpha} \otimes \boldsymbol{A}^{\alpha}_{,\beta} \otimes \boldsymbol{A}^{\beta} = \mathrm{GRAD}_{\mathcal{S}_0}\mathrm{GRAD}_{\mathcal{S}_0}\boldsymbol{x} \\ &=: \mathbb{F}^{(1)}(\boldsymbol{x}_{,\alpha,\beta}) + \mathbb{F}^{(2)}(\boldsymbol{x}_{,\alpha}) \end{aligned} \tag{3.10}$$

is also introduced. While the first term $\mathbb{F}^{(1)}$ depends on the second derivative of the deformed configuration, the second term $\mathbb{F}^{(2)}$ depends only on the first derivative. Due to identities

$$\boldsymbol{F} \cdot \boldsymbol{A}_{\alpha} = \boldsymbol{a}_{\alpha}, \quad \boldsymbol{F}^{-T} \cdot \boldsymbol{A}^{\alpha} = \boldsymbol{a}^{\alpha}, \quad \boldsymbol{n} = \boldsymbol{n}(\boldsymbol{a}_{\alpha}) \quad \text{and} \quad b_{\alpha\beta} = \boldsymbol{n} \cdot \mathbb{F} : [\boldsymbol{A}_{\alpha} \otimes \boldsymbol{A}_{\beta}] \tag{3.11}$$

together with Eq. $(3.5)_2$, it can be seen that curvature tensor $(3.6)_2$ associated with the deformed configuration can also be written in terms of the deformation gradient and the gradient of the deformation gradient, i.e.,

$$\boldsymbol{b} = \boldsymbol{b}(\boldsymbol{F}, \mathbb{F}). \tag{3.12}$$

3.2.1.3 Observer-invariant deformation measures

According to the previous section, deformation gradient $\boldsymbol{F}$ (Eq. (3.9)) and its gradient $\mathbb{F}$ (Eq. (3.10)) allow to capture stretching as well as bending effects of thin hollow spheres. However, since such variables are not invariant with respect to an observer transformation, they are not well-suited for defining Helmholtz energies. For instance and focusing on a first-order theory (only the first derivative of the deformation map is considered), the deformation gradient usually enters the Helmholtz energy through the right Cauchy-Green tensor

$$\boldsymbol{C} = \boldsymbol{F}^{T} \cdot \boldsymbol{F} = a_{\alpha\beta}\, \boldsymbol{A}^{\alpha} \otimes \boldsymbol{A}^{\beta}. \tag{3.13}$$

In the same line of thought, a fourth-order Cauchy-Green-like tensor

$$\mathbb{C} := \mathbb{F}^{T} \cdot \mathbb{F} \tag{3.14}$$

and a third-order Cauchy-Green-like tensor

$$\mathcal{C} := \boldsymbol{F}^{T} \cdot \mathbb{F} \tag{3.15}$$

are also defined. Instead of $\mathcal{C} = \boldsymbol{F}^T \cdot \mathbb{F}$, $\tilde{\mathcal{C}} = \boldsymbol{F}^{-1} \cdot \mathbb{F}$ is also often considered, cf. [26]. Tensors (3.13)–(3.15) represent a basis for deriving frame-indifferent (Helmholtz) energies. To be more precise,

$$\Psi = \Psi(\boldsymbol{F}, \mathbb{F}) \text{ is frame-indifferent, if and only if, } \Psi = \Psi(\boldsymbol{C}, \mathcal{C}, \mathbb{C}). \tag{3.16}$$

A less general, but frequently employed, family of frame-indifferent energies reads

$$\Psi = \Psi(a_{\alpha\beta}, b_{\alpha\beta}). \tag{3.17}$$

This function is to be understood in such a way that only the deformation-dependent variables are its arguments (vectors $\boldsymbol{A}^\beta$ are deformation-independent). It can be seen from Eq. (3.13) and Eq. (3.11) that parametrization (3.17) implies an energy of the type (3.16). The opposite implication, however, is not true. For instance, terms like $\boldsymbol{a}_{\alpha,\beta} \cdot \boldsymbol{a}_{\gamma,\delta}$ capturing in-plane gradient-elasticity are not included in the family of energies (3.17).

3.2.2 Balance laws for shells and second-order continua

3.2.2.1 Balance of linear momentum

If the temperature is fixed, as a starting point, the hyperelastic hollow spheres to be analyzed represent a conservative system. For this reason, balance of linear momentum can be naturally derived from the Euler-Lagrange equations of the underlying energy.

Description in terms of $a_{\alpha\beta}$ and $b_{\alpha\beta}$ Based on description (3.17) – which is the most common description for shell theory – the total energy of a hollow sphere can be written for a fixed temperature field as

$$I(\boldsymbol{x}) := \int_{\mathcal{S}_0} \Psi(a_{\alpha\beta}, b_{\alpha\beta}, \theta)|_{\theta=\text{const}} \, \mathrm{d}A - \int_{\mathcal{S}_0} \boldsymbol{f} \cdot \boldsymbol{u} \, \mathrm{d}A. \tag{3.18}$$

Here, θ is the (constant) temperature field, Ψ is the Helmholtz energy and $\boldsymbol{f}$ are prescribed area-specific dead loads. It bears emphasis that forces could also be applied at the boundary $\partial\mathcal{S}_0$. Furthermore, the theory would also account for prescribed bending moments. However, since such loads will not be considered within the numerical examples, the respective terms have been removed from the energy for the sake of brevity. Finally, it is noted that according to Eq. (3.18), Ψ is assumed to be area-specific with regard to the undeformed configuration.

In line with [125], the stationary condition associated with energy (3.18) reads

$$\int_{\mathcal{S}_0} \frac{1}{2} \, \delta a_{\alpha\beta} \tau^{\alpha\beta} \mathrm{d}A + \int_{\mathcal{S}_0} \delta b_{\alpha\beta} M^{\alpha\beta} \mathrm{d}A - \int_{\mathcal{S}_0} \delta \boldsymbol{x} \cdot \boldsymbol{f} \mathrm{d}A = 0 \quad \forall \delta \boldsymbol{x} \tag{3.19}$$

where $\delta(\bullet)$ denotes the variation of $(\bullet)$ with respect to $\boldsymbol{x}$, $\tau^{\alpha\beta} = 2\partial\Psi/\partial a_{\alpha\beta}$ are the coefficients of the Kirchhoff stress tensor $\boldsymbol{\tau} = \tau^{\alpha\beta}\,\boldsymbol{a}_\alpha \otimes \boldsymbol{a}_\beta$ (likewise of the second Piola-Kirchhoff stress tensor $\boldsymbol{S} = \tau^{\alpha\beta}\,\boldsymbol{A}_\alpha \otimes \boldsymbol{A}_\beta$ and the first Piola-Kirchhoff stress tensor $\boldsymbol{P} = \tau^{\alpha\beta}\boldsymbol{a}_\alpha \otimes \boldsymbol{A}_\beta$) and $M^{\alpha\beta}$ are the coordinates of the momentum tensor $\boldsymbol{m} = \partial\Psi/\partial\boldsymbol{b} = M^{\alpha\beta}\,\boldsymbol{a}_\alpha \otimes \boldsymbol{a}_\beta$. According to Eq. (3.19), both in-plane deformations ($a_{\alpha\beta}$) as well as bending-induced deformations ($b_{\alpha\beta}$) contribute to the energy.

Description in terms of $\boldsymbol{F}$ and $\mathbb{F}$ Energies depending on $a_{\alpha\beta}$ and $b_{\alpha\beta}$ are most natural from a structural engineering point of view, cf. [40]. By way of contrast, if shells are interpreted as higher-gradient continua, a description in terms of $\boldsymbol{F}$ and $\mathbb{F}$ represents the most frequent choice, cf. [80]. Furthermore, such a description is also more general, since it also covers in-plane gradient-elasticity, see Section 3.2.1.3. For this reason, it is discussed here. In this case, the total energy of a hollow sphere can be written for a fixed temperature field as (compare to Eq. (3.18))

$$I(\boldsymbol{x}) := \int_{\mathcal{S}_0} \Psi(\boldsymbol{F}, \mathbb{F}, \theta)|_{\theta=\text{const}}\, \mathrm{d}A - \int_{\mathcal{S}_0} \boldsymbol{f}\cdot\boldsymbol{x}\, \mathrm{d}A. \tag{3.20}$$

Clearly, Ψ has to be frame-indifferent, cf. Section 3.2.1.3.

Denoting the generalized stresses energetically dual to $\boldsymbol{F}$ and $\mathbb{F}$, respectively, as

$$\boldsymbol{P} := \frac{\partial\Psi}{\partial\boldsymbol{F}} \qquad \text{and} \qquad \mathbb{P} := \frac{\partial\Psi}{\partial\mathbb{F}}, \tag{3.21}$$

the stationary condition of energy (3.20) reads

$$\int_{\mathcal{S}_0} [\boldsymbol{P} : \delta\boldsymbol{F} + \mathbb{P} \therefore \delta\mathbb{F}]\, \mathrm{d}A - \int_{\mathcal{S}_0} \boldsymbol{f}\cdot\delta\boldsymbol{x}\, \mathrm{d}A = 0 \quad \forall\delta\boldsymbol{x}. \tag{3.22}$$

Again, $\delta(\bullet)$ denotes the variation of $(\bullet)$ with respect to $\boldsymbol{x}$ and $\therefore$ is the triple contraction. Applying the (surface) divergence-theorem (with $[\delta\boldsymbol{x}\cdot\boldsymbol{P}]_\alpha \cdot \boldsymbol{A}^\alpha =: \mathrm{DIV}_{\mathcal{S}_0}[\delta\boldsymbol{x}\cdot\boldsymbol{P}] = \boldsymbol{P} : \delta\boldsymbol{F} + \delta\boldsymbol{x}\cdot\mathrm{DIV}_{\mathcal{S}_0}\boldsymbol{P}$), together with the Gauss-theorem to the first term in Eq. (3.22) once and to the second term in Eq. (3.22) twice and localizing the resulting equation, yields the strong form

$$\mathrm{DIV}_{\mathcal{S}_0}\mathrm{DIV}_{\mathcal{S}_0}\mathbb{P} - \mathrm{DIV}_{\mathcal{S}_0}\boldsymbol{P} - \boldsymbol{f} = \boldsymbol{0} \quad \forall\boldsymbol{X} \in \mathcal{S}_0, \tag{3.23}$$

$$-[\mathrm{DIV}_{\mathcal{S}_0}\boldsymbol{P}]\cdot\hat{\boldsymbol{N}} - \mathrm{DIV}_{\mathcal{S}_0}[\boldsymbol{P}\cdot\hat{\boldsymbol{N}}] + \boldsymbol{P}\cdot\hat{\boldsymbol{N}} = \boldsymbol{0} \quad \forall\boldsymbol{X} \in \partial\mathcal{S}_0. \tag{3.24}$$

It has been used within the derivations that $\boldsymbol{F}$ and $\mathbb{F}$ as well as their energetically dual counterparts $\boldsymbol{P}$ and $\mathbb{P}$ are superficial in the sense of [70]. The vector $\hat{\boldsymbol{N}}$ denotes the superficial unit normal at the surface boundary $\partial\mathcal{S}_0$ pointing outwards. Further details can also be found in [80] where identity $\hat{S}(\bullet) = \mathrm{DIV}_{\mathcal{S}_0}(\bullet)$ holds for superficial tensors.

According to Eq. (3.23), it can indeed be seen that the balance laws are associated with a higher-order continuum model.

Since a description in terms of $\boldsymbol{F}$ and $\mathbb{F}$ is more general than a description depending on $a_{\alpha\beta}$ and $b_{\alpha\beta}$, the first will be considered in the following.

Relation between both descriptions The coefficients $a_{\alpha\beta}$ of the metric tensor can evidently be computed from variables $\boldsymbol{F}$ and $\mathbb{F}$ as

$$a_{\alpha\beta} = [\boldsymbol{A}_\alpha \otimes \boldsymbol{A}_\beta] : \boldsymbol{C} = [\boldsymbol{A}_\alpha \otimes \boldsymbol{A}_\beta] : \left[\boldsymbol{F}^T \cdot \boldsymbol{F}\right], \tag{3.25}$$

while the coefficients $b_{\alpha\beta}$ of the curvature tensor are given by Eq. $(3.11)_4$. Both variables are invariant with respect to an observer transformation and thus, energies based on these variable are automatically frame-indifferent. By computing the variations of $a_{\alpha\beta}$ and $b_{\alpha\beta}$, inserting the result into weak form (3.19) and finally, by comparing this equation to weak form (3.22), one can derive expressions for generalized stresses $\boldsymbol{P}$ and $\mathbb{P}$ in terms of $\tau^{\alpha\beta}$ and $M^{\alpha\beta}$. For instance, the first term in Eq. (3.19) yields

$$\frac{1}{2}\,\tau^{\alpha\beta}\,\delta a_{\alpha\beta} = \tau^{\alpha\beta}\,[\boldsymbol{a}_\alpha \otimes \boldsymbol{A}_\beta] : \delta\boldsymbol{F} \quad \Rightarrow \quad \boldsymbol{P}^{(1)} := \tau^{\alpha\beta}\,\boldsymbol{a}_\alpha \otimes \boldsymbol{A}_\beta. \tag{3.26}$$

Likewise, the second term in Eq. (3.19) leads to

$$M^{\alpha\beta}\,\delta b_{\alpha\beta} = \underbrace{M^{\alpha\beta}\,\left[\boldsymbol{n} \otimes \boldsymbol{A}^\alpha \otimes \boldsymbol{A}^\beta\right]}_{=\,\mathbb{P}} \therefore \delta\mathbb{F} + \underbrace{M^{\alpha\beta}\,[\boldsymbol{A}_\beta \otimes \boldsymbol{A}_\alpha] : \mathbb{F}^T \cdot \delta\boldsymbol{n}}_{\boldsymbol{P}^{(2)} \,:\, \delta\boldsymbol{F}} \tag{3.27}$$

where $\delta\boldsymbol{n}$ is the variation of the normal vector with respect to the deformed configuration and the transposed $\mathbb{F}^T$ is defined by reversing the order of the involved basis vectors. According to Eq. (B.1) in [117],

$$\frac{\partial \boldsymbol{n}}{\partial \boldsymbol{a}_\beta} = -\boldsymbol{a}^\beta \otimes \boldsymbol{n}. \tag{3.28}$$

As a consequence, the variation of the normal vector can be written as (see also [81] (B.33))

$$\delta\boldsymbol{n} = \frac{\partial \boldsymbol{n}}{\partial \boldsymbol{a}_\beta} \cdot \delta\boldsymbol{a}_\beta = -\left[\boldsymbol{a}^\beta \otimes \boldsymbol{n} \otimes \boldsymbol{A}_\beta\right] : \delta\boldsymbol{F} \tag{3.29}$$

and the first Piola-Kirchhoff-type stress tensor $\boldsymbol{P}^{(2)}$ in Eq. (3.27) results in

$$\boldsymbol{P}^{(2)} = -M^{\alpha\beta}\,[\boldsymbol{A}_\beta \otimes \boldsymbol{A}_\alpha] : \mathbb{F}^T \cdot [\boldsymbol{a}^\gamma \otimes \boldsymbol{n} \otimes \boldsymbol{A}_\gamma]\,. \tag{3.30}$$

In summary, a description of the mechanical problem in terms of shell-like quantities $a_{\alpha\beta}$ and $b_{\alpha\beta}$ is equivalent to a description in terms of $\boldsymbol{F}$ and $\mathbb{F}$ by choosing

$$\begin{aligned}
\boldsymbol{P} &= \boldsymbol{P}^{(1)} + \boldsymbol{P}^{(2)} \\
\boldsymbol{P}^{(1)} &= \tau^{\alpha\beta}\, \boldsymbol{a}_\alpha \otimes \boldsymbol{A}_\beta \\
\boldsymbol{P}^{(2)} &= -M^{\alpha\beta}\, [\boldsymbol{A}_\beta \otimes \boldsymbol{A}_\alpha] : \mathbb{F}^T \cdot [\boldsymbol{a}^\gamma \otimes \boldsymbol{n} \otimes \boldsymbol{A}_\gamma] \\
&= -M^{\alpha\beta}\, \left[\boldsymbol{a}_{\alpha,\beta} \cdot \boldsymbol{a}^\gamma + \boldsymbol{A}_\alpha \cdot \boldsymbol{A}^\gamma_{,\beta}\right] \boldsymbol{n} \otimes \boldsymbol{A}_\gamma \\
\mathbb{P} &= M^{\alpha\beta}\, \left[\boldsymbol{n} \otimes \boldsymbol{A}^\alpha \otimes \boldsymbol{A}^\beta\right]
\end{aligned} \tag{3.31}$$

for given shell-like generalized stresses $\tau^{\alpha\beta}$ and $M^{\alpha\beta}$.

3.2.2.2 Balance of angular momentum

Since both energies (3.16) and (3.17) are frame-indifferent, they are invariant with respect to a superposed rigid body motion. As shown, e.g., in [117], this property automatically ensures balance of angular momentum – point-wise.

3.2.2.3 Energy balance

Considering the more general description in terms of $\boldsymbol{F}$ and $\mathbb{F}$, the first law of thermodynamics applied to the presented modeling framework of thin hollow spheres reads

$$\int_{\mathcal{S}_0} \rho_0\, r \,\mathrm{d}A - \int_{\partial\mathcal{S}_0} \boldsymbol{J} \cdot \hat{\boldsymbol{N}} \,\mathrm{d}S + \int_{\mathcal{S}_0} \underbrace{\boldsymbol{P} : \dot{\boldsymbol{F}} + \mathbb{P} \therefore \dot{\mathbb{F}}}_{=\mathcal{P}} \,\mathrm{d}A - \int_{\mathcal{S}_0} \dot{u} \,\mathrm{d}A = 0. \tag{3.32}$$

Here, r is the mass-specific heat source, $\boldsymbol{J}$ is the heat flux, $\mathcal{P}$ is the (generalized) stress power, u is the volume-specific internal energy and the superposed dot represents the material time derivative. Since heat conduction is only considered within the tangent plane of $\mathcal{S}_0$, $\boldsymbol{J} = J^\alpha\, \boldsymbol{A}_\alpha$ holds. Accordingly, the heat flux vector is superficial ($\boldsymbol{J} \cdot \boldsymbol{N} = 0$) and thus, application of Gauss-theorem yields

$$\int_{\partial\mathcal{S}_0} \boldsymbol{J} \cdot \hat{\boldsymbol{N}} \,\mathrm{d}S = \int_{\mathcal{S}_0} \mathrm{DIV}_{\mathcal{S}_0} \boldsymbol{J} \,\mathrm{d}A. \tag{3.33}$$

Alternatively, one may write $\mathrm{DIV}_{\mathcal{S}_0} \boldsymbol{J} = (J^\alpha\, \boldsymbol{A}_\alpha)_{,\beta} \cdot \boldsymbol{A}^\beta = J^\alpha_{,\alpha} + J^\alpha\, (\boldsymbol{A}_{\alpha,\beta} \cdot \boldsymbol{A}^\beta)$ showing that the surface divergence is the covariant derivative of the heat flux.

The Helmholtz energy is related to internal energy u and entropy N (being energetically dual to the temperature θ) as

$$\Psi = u - \theta\, N. \tag{3.34}$$

Inserting this relation and Eq. (3.33) into Eq. (3.32), yields the strong form

$$\rho_0\, r - \mathrm{DIV}_{\mathcal{S}_0}\boldsymbol{J} + \frac{\partial^2\Psi}{\partial\theta^2}\,\dot{\theta}\,\theta + \frac{\partial^2\Psi}{\partial\theta\partial\boldsymbol{F}} : \dot{\boldsymbol{F}}\,\theta + \frac{\partial^2\Psi}{\partial\theta\partial\mathbb{F}} \therefore \dot{\mathbb{F}}\,\theta = 0. \tag{3.35}$$

While the third term in Eq. (3.35) is related to the heat capacity, the fourth as well as the fifth term correspond to structural heating. The fifth term is neglected in the following. Multiplying the strong form (3.35) by test function $\delta\theta$, integration over the body and applying the surface divergence theorem as well as the Gauss-theorem finally yields the weak form

$$\begin{aligned} 0 = &\int_{\mathcal{S}_0} \rho_0\, r\, \delta\theta \,\mathrm{d}A - \int_{\partial\mathcal{S}_0} \boldsymbol{J}\cdot\hat{\boldsymbol{N}}\,\delta\theta\,\mathrm{d}S + \int_{\mathcal{S}_0} \boldsymbol{J}\cdot\mathrm{GRAD}_{\mathcal{S}_0}\delta\theta\,\mathrm{d}A \\ &+ \int_{\mathcal{S}_0}\left[\frac{\partial^2\Psi}{\partial\theta^2}\,\dot{\theta}\,\theta + \frac{\partial^2\Psi}{\partial\theta\partial\boldsymbol{F}} : \dot{\boldsymbol{F}}\,\theta\right]\delta\theta\,\mathrm{d}A \quad \forall\delta\theta. \end{aligned} \tag{3.36}$$

3.3 Constitutive model

The modeling framework is completed by choosing a suitable constitutive model on the basis of a proper Helmholtz energy $\Psi = \Psi(\boldsymbol{F}, \mathbb{F}, \theta)$. As far as the Helmholtz energy is concerned, the family of energies

$$\Psi(\boldsymbol{F}, \mathbb{F}, \theta) = \Psi^{\mathrm{m}}(\boldsymbol{F}, \mathbb{F}) + \Psi^{\theta}(\theta) + \Psi^{\mathrm{c}}(\boldsymbol{F}, \theta) \tag{3.37}$$

is considered. Here, Ψ^{m} is a purely mechanical part, Ψ^{θ} is a purely thermal part and Ψ^{c} is related to the coupling of both fields.

Mechanical part $\Psi^{\mathrm{m}}(\boldsymbol{F}, \mathbb{F})$ is further decomposed into membrane $(\bullet)_{\mathrm{mem}}$ and bending contributions $(\bullet)_{\mathrm{ben}}$, i.e.,

$$\Psi^{\mathrm{m}} = \Psi^{\mathrm{m}}_{\mathrm{mem}}(\boldsymbol{F}) + \Psi^{\mathrm{m}}_{\mathrm{ben}}(\boldsymbol{F}, \mathbb{F}). \tag{3.38}$$

Frame-indifference of energy (3.38) is guaranteed and the comparison with classical shell theory is made possible by choosing generalized strain-like variables

$$\begin{array}{llll} \boldsymbol{E} & = \boldsymbol{E}(\boldsymbol{F}) & = \dfrac{1}{2}\left(\boldsymbol{F}^T\cdot\boldsymbol{F} - \boldsymbol{1}\right) & = \dfrac{1}{2}\left(a_{\alpha\beta} - A_{\alpha\beta}\right)\boldsymbol{A}^{\alpha}\otimes\boldsymbol{A}^{\beta} \\ \boldsymbol{K} & = \boldsymbol{K}(\boldsymbol{F}, \mathbb{F}) & = \boldsymbol{F}^{-T}\cdot\boldsymbol{b}\cdot\boldsymbol{F}^{-1} - \boldsymbol{B} & = \left(b_{\alpha\beta} - B_{\alpha\beta}\right)\boldsymbol{A}^{\alpha}\otimes\boldsymbol{A}^{\beta} \end{array} \tag{3.39}$$

i.e., the surface Green-Lagrange strain tensor $\boldsymbol{E}$ and the relative curvature tensor $\boldsymbol{K}$. Both variables are defined with respect to the undeformed configuration. Due to the

definition of the relative curvature tensor (see Eq. $(3.39)_2$), relation $\delta \boldsymbol{K} \cdot \boldsymbol{M} = \delta b_{\alpha\beta}\, M^{\alpha\beta}$ holds true and coordinates

$$M^{\alpha\beta} = \frac{\partial \Psi^{\mathrm{m}}_{\mathrm{ben}}}{\partial K_{\alpha\beta}} = \frac{\partial \Psi^{\mathrm{m}}_{\mathrm{ben}}}{\partial b_{\alpha\beta}} \tag{3.40}$$

are indeed dual to the coordinates of curvature tensor $\boldsymbol{b}$. Coordinates $M^{\alpha\beta}$, in turn, allow to compute generalized stresses $\boldsymbol{P}^{(2)}$ and $\mathbb{P}$, cf. Eqs. (3.31). The specific mechanical energy contribution considered for the present analysis is based on the classic (plane-stress) Saint-Venant-Kirchhoff model as presented in [40, 52, 136] and reads

$$\Psi^{\mathrm{m}} = \Psi^{\mathrm{m}}_{\mathrm{mem}} + \Psi^{\mathrm{m}}_{\mathrm{ben}} = \frac{1}{2}\, \boldsymbol{E} : \mathbb{C} : \boldsymbol{E} + \frac{1}{2}\, \boldsymbol{K} : \mathbb{D} : \boldsymbol{K}. \tag{3.41}$$

The fourth order tensors can be defined via the familiar structure based on Lamé constants

$$\mathbb{C} = \lambda \boldsymbol{I} \otimes \boldsymbol{I} + 2\mu\, (\boldsymbol{I} \otimes \boldsymbol{I})^{\mathrm{s}} \quad \text{and} \quad \mathbb{D} = \frac{s^2}{12}\mathbb{C}, \tag{3.42}$$

with s denoting the shell thickness and $(\boldsymbol{I} \otimes \boldsymbol{I})^{\mathrm{s}} : \boldsymbol{V} = \mathrm{sym}(\boldsymbol{V})$, with arbitrary second order tensor $\boldsymbol{V}$. By taking into account plane-stress conditions [40, 52, 137], the incorporated Lamé constants, λ and μ, relate to the ones of 3D bulk materials, $\tilde{\lambda}$ and $\tilde{\mu}$, as

$$\lambda = s\frac{2\,\tilde{\lambda}\tilde{\mu}}{\tilde{\lambda} + 2\,\tilde{\mu}} \quad \text{and} \quad \mu = s\,\tilde{\mu}. \tag{3.43}$$

Next, coupling energy Ψ^{c} is introduced. It is motivated by the three-dimensional ansatz in [25], where it reads $\Psi^{\mathrm{c}} = -3\,\alpha\,[\theta - \theta_e]\; K \mathrm{tr}\left(\tilde{\boldsymbol{E}}\right)\, s$. For the present plane-stress situation, the coupling energy becomes

$$\Psi^{\mathrm{c}} = -c_1(\theta - \theta_e)\mathrm{tr}(\boldsymbol{E}) - \frac{1}{2}c_2(\theta - \theta_e)^2 \tag{3.44}$$

with

$$c_1 = s\frac{2\,\tilde{\mu}}{\tilde{\lambda} + 2\,\tilde{\mu}} 3\,\alpha \left(\tilde{\lambda} + \frac{2}{3}\,\tilde{\mu}\right) \quad \text{and} \quad c_2 = s\,\frac{9\,\alpha^2}{\tilde{\lambda} + 2\,\tilde{\mu}} \left(\tilde{\lambda} + \frac{2}{3}\,\tilde{\mu}\right)^2. \tag{3.45}$$

Here, α denotes the thermal expansion coefficient. The coupling energy (3.44) gives rise to the additional contribution of the stress tensor

$$\boldsymbol{P}^{(1)\mathrm{c}} := \frac{\partial \Psi^{\mathrm{c}}}{\partial \boldsymbol{F}} = -c_1(\theta - \theta_e)\boldsymbol{F} \tag{3.46}$$

as well as to the structural heating term

$$\frac{\partial^2 \Psi^{\mathrm{c}}}{\partial \boldsymbol{F} \partial \theta} = -c_1 \boldsymbol{F}. \tag{3.47}$$

Finally, the purely thermal part of the Helmholtz energy is chosen as

$$\Psi^{\theta}(\theta) = c_{\mathrm{d}} \left[\theta - \theta_e\right] - c_{\mathrm{d}}\, \theta \ln\left(\frac{\theta}{\theta_e}\right). \tag{3.48}$$

It enters the first law of thermodynamics through the derivative

$$\frac{\partial^2 \Psi^{\theta}}{\partial \theta^2} = c_{\mathrm{d}} \frac{1}{\theta}. \tag{3.49}$$

The constitutive framework is completed by assuming a Fourier-type model for heat conduction, i.e.,

$$\boldsymbol{J} = -k\, \mathrm{GRAD}_{\mathcal{S}_0} \theta = -k\, \theta_{\alpha}\, \boldsymbol{A}^{\alpha} \tag{3.50}$$

where k is the (constant) thermal conductivity.

A summary of the complete model is finally given. While the weak form of equilibrium is computed as

$$\begin{array}{lcl} 0 & = & \displaystyle\int_{\mathcal{S}_0} \left[\boldsymbol{P} : \delta \boldsymbol{F} + \mathbb{P} \therefore \delta \mathbb{F}\right] \mathrm{d}A - \int_{\mathcal{S}_0} \boldsymbol{f} \cdot \delta \boldsymbol{x}\, \mathrm{d}A \quad \forall \delta \boldsymbol{x} \\ \boldsymbol{P} & = & \boldsymbol{P}^{(1)\mathrm{m}} + \boldsymbol{P}^{(1)\mathrm{c}} + \boldsymbol{P}^{(2)} = \text{Eq. (3.54)} + \text{Eq. (3.46)} + \text{Eq. (3.31)}_3 \\ \mathbb{P} & = & \text{Eq. (3.31)}_4 \\ M^{\alpha\beta} & = & \text{Eq. (3.55)}, \end{array} \tag{3.51}$$

the first law of thermodynamics takes the format

$$\begin{array}{lcl} 0 & = & \displaystyle\int_{\mathcal{S}_0} \rho_0\, r\, \delta\theta\, \mathrm{d}A - \int_{\partial \mathcal{S}_0} \boldsymbol{J} \cdot \hat{\boldsymbol{N}}\, \delta\theta\, \mathrm{d}S + \int_{\mathcal{S}_0} \boldsymbol{J} \cdot \mathrm{GRAD}_{\mathcal{S}_0} \delta\theta\, \mathrm{d}A \\ & & \displaystyle + \int_{\mathcal{S}_0} \left[\frac{\partial^2 \Psi}{\partial \theta^2}\, \dot{\theta}\, \theta + \frac{\partial^2 \Psi}{\partial \theta \partial \boldsymbol{F}} : \dot{\boldsymbol{F}}\, \theta\right] \delta\theta\, \mathrm{d}A \quad \forall \delta\theta \\ \boldsymbol{J} & = & \text{Eq. (3.50)} \\ \dfrac{\partial^2 \Psi}{\partial \theta^2}\, \theta & = & c_{\mathrm{d}} \text{ (see Eq. (3.49))} \\ \dfrac{\partial^2 \Psi}{\partial \theta \partial \boldsymbol{F}} & = & \text{Eq. (3.47)}. \end{array} \tag{3.52}$$

The complete prototype energy and generalized stress tensors of the present analysis write

$$\begin{aligned}\Psi\left(\boldsymbol{E},\boldsymbol{K},\theta\right) = \frac{1}{2}\,\boldsymbol{E}:\mathbb{C}:\boldsymbol{E} + \frac{1}{2}\,\boldsymbol{K}:\mathbb{D}:\boldsymbol{K} \\ -c_1(\theta-\theta_e)\mathrm{tr}(\boldsymbol{E}) - \frac{1}{2}c_2(\theta-\theta_e)^2 \\ +c_\mathrm{d}\left[\theta-\theta_e\right] - c_\mathrm{d}\,\theta\ln\left(\frac{\theta}{\theta_e}\right),\end{aligned} \tag{3.53}$$

$$\begin{aligned}\boldsymbol{P} := \frac{\partial\Psi}{\partial\boldsymbol{F}} &= \lambda\,\mathrm{tr}(\boldsymbol{E})\,\boldsymbol{F} + 2\,\mu\,\boldsymbol{F}\cdot\boldsymbol{E} - c_1(\theta-\theta_e)\boldsymbol{F} \\ &= \underbrace{\left[\lambda\,E^\gamma_\gamma\,A^{\alpha\beta} + 2\,\mu\,E^{\alpha\beta} - c_1(\theta-\theta_e)A^{\alpha\beta}\right]}_{=\,\tau^{\alpha\beta}}\boldsymbol{a}_\alpha\otimes\boldsymbol{A}_\beta\end{aligned} \tag{3.54}$$

and

$$\boldsymbol{M} = \frac{\partial\Psi}{\partial\boldsymbol{K}} = \frac{s^2}{12}\left[\lambda\,\mathrm{tr}(\boldsymbol{K})\,\boldsymbol{1} + 2\,\mu\,\boldsymbol{K}\right] = \underbrace{\frac{s^2}{12}\left[\lambda\,K^\gamma_\gamma\,A^{\alpha\beta} + 2\,\mu\,K^{\alpha\beta}\right]}_{=\,M^{\alpha\beta}}\boldsymbol{A}_\alpha\otimes\boldsymbol{A}_\beta. \tag{3.55}$$

3.4 Numerical implementation

The finite-element implementation of the model, as summarized in Eqs. (3.51) and (3.52), is discussed in this section.

3.4.1 Bubnov-Galerkin method and isoparametric approach

In line with the Bubnov-Galerkin method, primary field $\boldsymbol{x}$ and its test function $\delta\boldsymbol{x}$ are interpolated by means of the same shape functions. Accordingly, ansatz

$$\boldsymbol{x} = \sum_{i=1}^{n} N^{(i)}\boldsymbol{x}_e^{(i)} = \boldsymbol{N}\,\boldsymbol{x}_e \qquad \delta\boldsymbol{x} = \sum_{i=1}^{n} N^{(i)}\delta\boldsymbol{x}_e^{(i)} = \boldsymbol{N}\,\delta\boldsymbol{x}_e \tag{3.56}$$

is made for each finite element (or patch). Here, $N^{(i)}$ is the shape function of node i (vector $\boldsymbol{N}$ contains all shape functions) and $\boldsymbol{x}_e^{(i)}$ is the coordinate of node i with respect to the deformed configuration (vector $\boldsymbol{x}_e$ contains the coordinates of all nodes). The same notation also applies to field $\delta\boldsymbol{x}$. Identical shape functions are also applied for interpolating the temperature field as well as its test functions, i.e.,

$$\theta = \sum_{i=1}^{n} N^{(i)}\theta_e^{(i)} = \boldsymbol{N}\,\boldsymbol{\theta}_e \qquad \delta\theta = \sum_{i=1}^{n} N^{(i)}\delta\theta_e^{(i)} = \boldsymbol{N}\,\delta\boldsymbol{\theta}_e. \tag{3.57}$$

Following an isoparametric approach, the undeformed reference configuration is also interpolated by shape functions $N^{(i)}$.

Based on ansatz (3.56) and (3.57), the gradients within weak form (3.51) and (3.52) are approximated in standard fashion. For instance,

$$\begin{aligned} \boldsymbol{F} &= \sum_{i=1}^{n} \boldsymbol{x}_e^{(i)} \otimes \mathrm{GRAD}_{\mathcal{S}_0} N^{(i)}, \quad \mathrm{GRAD}_{\mathcal{S}_0}\theta = \sum_{i=1}^{n} \theta_e^{(i)} \,\mathrm{GRAD}_{\mathcal{S}_0} N^{(i)}, \\ \mathbb{F} &= \sum_{i=1}^{n} \boldsymbol{x}_e^{(i)} \otimes \mathrm{GRAD}^2_{\mathcal{S}_0} N^{(i)}, \end{aligned} \tag{3.58}$$

where $\mathrm{GRAD}^2_{\mathcal{S}_0}(\bullet) = \mathrm{GRAD}_{\mathcal{S}_0}\mathrm{GRAD}_{\mathcal{S}_0}(\bullet)$ is the second surface gradient. The same procedure is also applied to the virtual fields, e.g.,

$$\delta\boldsymbol{F} = \sum_{i=1}^{n} \delta\boldsymbol{x}_e^{(i)} \otimes \mathrm{GRAD}_{\mathcal{S}_0} N^{(i)}, \quad \mathrm{GRAD}_{\mathcal{S}_0}\delta\theta = \sum_{i=1}^{n} \delta\theta_e^{(i)} \,\mathrm{GRAD}_{\mathcal{S}_0} N^{(i)}. \tag{3.59}$$

Clearly, shape functions $N^{(i)}$ are usually not defined with respect to physical coordinate $\boldsymbol{X}$. In order to derive gradients such as $\mathrm{GRAD}_{\mathcal{S}_0} N^{(i)}$, one has to apply the chain rule in combination with the isoparametric concept.

3.4.2 Time discretization

The derivation of the problem at hand has been carried out in a time-continuous manner. Its implementation is performed in a time-discrete manner, where the rates of variables $\bullet$ are approximated by first-order differences in time as

$$\dot{\bullet} = \frac{\bullet_{n+1} - \bullet_n}{\Delta t}. \tag{3.60}$$

Here, index $n+1$ refers to the unknown time step and n to the last known one. No artificial damping or stabilization has been used for the present parameter settings of the thermal diffusion-dominated thermo-elastic problems.

The formation of sintering contacts and necking has been determined by a pseudo-time evolution parametrized in terms of the evolving sinter radius. The sinter contact radius r is assumed to grow strictly monotonic in time t (not necessarily linear) and hence uniquely determines the updated contact conditions. The detailed implementation of the contact formulation is provided below along with the description of the sintering process.

3.4.3 IGA

Due to the consideration of curvature effects, the second derivative of the spacial coordinates is required. There are multiple ways to achieve this, such as mixed-element formulations, each presenting their own set of advantages and disadvantages. This paper follows the approach using NURBS as shape functions. This concept was first introduced by Hughes et al. [76] and fosters the goal of bridging the interface between Finite Element Analysis (FEA) and Computer Aided Design (CAD). Some of the benefits of NURBS are a geometrically accurate representation of curved geometries, various mesh refinement strategies without CAD regeneration, and an inherent fulfillment of C^1-continuity across element boundaries. NURBS $R_{ij}(\xi,\eta)$ are defined in the parameter space of shells as

$$R_{ij}(\xi,\eta) = \frac{w_{ij}\, N_i(\xi)\; M_j(\eta)}{\sum_{k,l} w_{kl}\, N_k(\xi)\; M_l(\eta)}.$$

The B-Splines N and M are defined recursively here, for instance for N, as

$$N_{i,0}(\xi) = \begin{cases} 1 & \text{if} \quad \xi_i \leq \xi < \xi_{i+1}, \\ 0 & \text{otherwise} \end{cases} \tag{3.61}$$

$$N_{i,p}(\xi) = \frac{\xi - \xi_i}{\xi_{i+p} - \xi_i} N_{i,p-1}(\xi) + \frac{\xi_{i+p+1} - \xi}{\xi_{i+p+1} - \xi_{i+1}} N_{i+1,p-1}(\xi). \tag{3.62}$$

Their polynomial degree p and the multiplicity of m entries at each node dictate the C^{p-m}-continuity. The range of possible geometries covered by conventional B-Splines can be increased by introducing further control points with weights $w_{i,j}$.

3.4.4 Sintering process and contact formulation

As motivated before, the thermomechanical framework will be studied by the example of sintered hollow spheres. The impact of the sintered geometry on the thermoelastic properties is of primary interest. Yet the sintering process itself must be captured beforehand. Given the generally vast amount of possible materials, the present simulation uses a generalized description until the early stage of necking. Particular attention is also given to the numerical realization in the proposed framework.

Sintering involves multiple transport paths of matter, for instance, surface diffusion, grain-boundary diffusion, volume diffusion or vapor transport [14, 84, 119], see Fig. 3.2 a). Surface tension and curvature are among the driving processes that lead to the classical Frenkel's model [148] for sintering and various extensions. The time scale determining the growth of the sintered interface, however, depends on the dominating paths and mechanisms. Polymer powders, for example, show three resulting stages of sintering kinetics [6]. The initial stationary contact is a balance between surface tension and repulsion by elasticity. Subsequently, the contact area grows due to inter-surface adhesion and visco-elastic deformation. Finally, the classical Frenkel theory is

approached for larger contact areas with surface tension as a driving process of dissipative viscous flow.

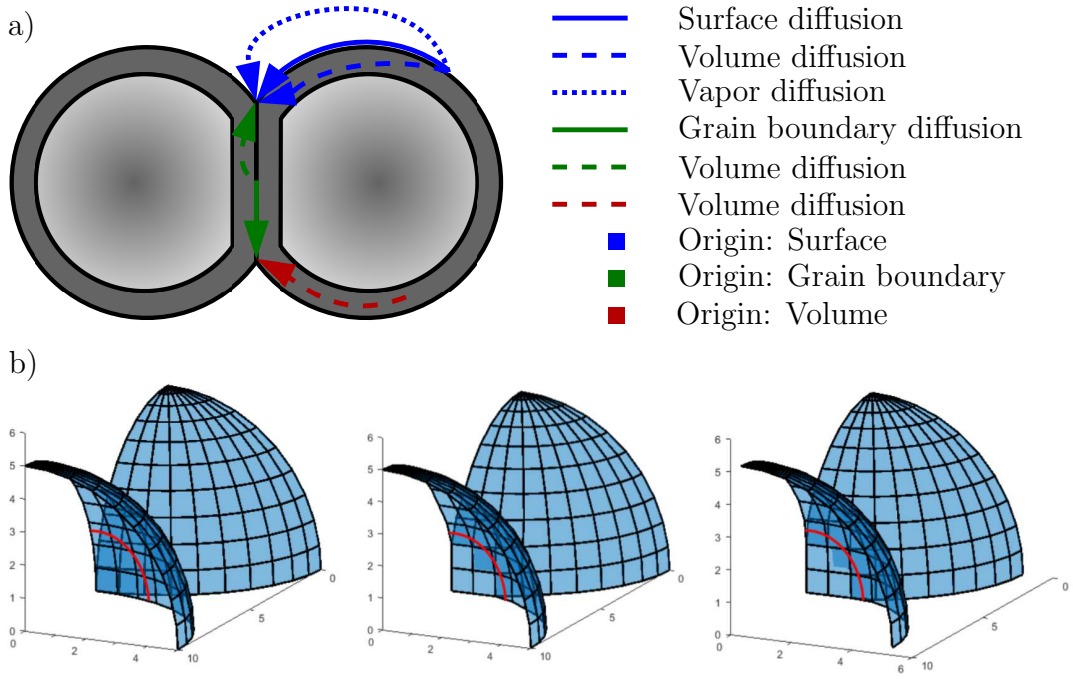

Figure 3.2: a) Visualization of possible diffusion paths during the sintering process.
b) Visualization of the sintering process. Identification of contact elements, establishing contact between these elements and relaxation of the system.

The present focus is characterized by early-stage sintering of hollow spheres that yields to necking. This implies three notable assumptions in agreement with the fabrication of light-weight structures [11, 87] and the relative motion of particles [149]. Firstly, the mass reduction due to diffusive transport is negligible such that the thickness and material parameters can be assumed to remain constant. Secondly, the characteristic diffusion length differs from solid particles and is assumed to be less dominated by volume diffusion. Thirdly, this early stage of sintering can be captured by a single characteristic time scale. We thus assume that the sintering evolution of the contact radius $r(t)$ can be captured by the generalized form of [119]

$$\left(\frac{r(t)}{R_0}\right)^n = B\, R_0^{-m} t. \tag{3.63}$$

R_0 is the initial radius of the spheres, and B, n and m are constants as provided in [119] for various sintering mechanisms. They can depend on material, temperature and thickness, amongst others and are yet rarely available for sintering processes of thin or slender bodies.

Numerically, the sintering process is first employed artificially before mechanical and thermal loading is applied to the sintered system, see Figure 3.2 b). For this reason, the contact radius is explicitly dictated by numerical stability until the desired sinter radius r_0 is reached (with an implicit pseudo time and implicit scaling via B, m and n according to (3.63)). Once reaching the end radius r_0, the artificial sintering process stops. The system relaxes into its new reference configuration for the subsequent thermo-mechanical analysis.

To be more precise in terms of the numerical implementation, the radius $r(t)$ of the contact area is first calculated for a new pseudo time step and all elements lying inside this radius are identified. Subsequently, all control points belonging to these inner elements are moved into the sinter plane by the IGA framework. The sinter surface is defined by three control points $\boldsymbol{x}_1$, $\boldsymbol{x}_2$ and $\boldsymbol{x}_3$. The displacement of all other points $\boldsymbol{x}_a$ in the sinter area is then linked to the motion of three reference points using two scaling factors f_1 and f_2 as

$$[\boldsymbol{x}_2 - \boldsymbol{x}_1, \boldsymbol{x}_3 - \boldsymbol{x}_1] \begin{bmatrix} f_1 \\ f_2 \end{bmatrix} + \boldsymbol{x}_1 = \boldsymbol{x}_a, \quad (1 - f_1 - f_2)\, \boldsymbol{x}_1 + f_1\, \boldsymbol{x}_2 + f_2\, \boldsymbol{x}_3 - \boldsymbol{x}_a = \boldsymbol{0}. \tag{3.64}$$

It preserves the relative motion inside the once established sinter surface. The newly added points are then constrained to only relax within the established plane (mimicking diffusion with negligible pre-stresses), while a new mechanical equilibrium state is computed. As the sinter surface can however move as a whole, e.g. during thermal expansion or stretching, its orientation is first determined by connecting the spheroid's centers. A translation in this direction $\boldsymbol{n}_c$ (i.e. the sinter surface normal direction) is described by an offset vector $\Delta\boldsymbol{x}_{\text{offset}}$. For any control point $\boldsymbol{x}_n$, the normal translation is dictated by an offset with respect to the initial point of sphere contact $\boldsymbol{x}_c$ as

$$\Delta\boldsymbol{x}_{\text{offset}} = [\boldsymbol{n}_c \cdot (\boldsymbol{x}_c - \boldsymbol{x}_n)]\, \boldsymbol{n}_c. \tag{3.65}$$

The established set of linear constrains is imposed on the system by eliminating dependent variables, following [153]. Here, all constraints are generated consecutively, e.g. C^1-continuity and sintering constraints, and linear dependencies are finally resolved by Gauss-Jordan elimination. The sinter surface effectively couples the elastic resistance of the two adjacent walls. Further assuming a relatively small distance within and across the sinter area (thin-wall assumption and early-stage necking), the temperature of two adjacent points is equilibrated instantly within the pseudo time step. It shall moreover be noted that the initial problems start with symmetric spheroids and matching control points on either side of a potential sinter surface. Symmetry conditions are used wherever possible in the following problems. They are not used, though, when they become unsuitable to study buckling modes or shrinking and growing of adjacent spheres. The handling of mismatching discretizations is straightforward by interpolating the temperature based on the primary control points presented before.

3.4.5 Benchmarking and mesh convergence

Two mechanical problems are used to benchmark and to assess the mesh convergence of the proposed framework, respectively. First, a square plate with side lengths $a = b = 12\,[\mathrm{mm}]$ and flexural rigidity $D = E\,s^3/12\,(1-\nu^2) \approx 2465.58\,[\mathrm{N\,mm}]$ under sinusoidal pressure shall serve as a well-established benchmark problem [52], see Fig. 3.3. The pressure is applied in the x-y plane of the reference configuration as

$$p(x,y) = p_0 \sin\left(\frac{\pi\,x}{a}\right) \sin\left(\frac{\pi\,y}{b}\right). \tag{3.66}$$

and yields a maximum deflection (cf. the analytical solution in [147]) of

$$w = \frac{p_0}{\pi^4\,D\,\left(\frac{1}{a^2}+\frac{1}{b^2}\right)^2} \sin\left(\frac{\pi\,x}{a}\right) \sin\left(\frac{\pi\,y}{b}\right) \tag{3.67}$$

as the main reference value. The simulations show converge towards the same maximum deflection for tested polynomial degrees of degree two and three even for coarse discretizations. Numerically, the relative error is $\approx 3\%$ for a coarse 3×3 discretization and polynomial degree of two, dropping to less than 1% for a 6×6 discretization. For a polynomial degree of three, the coarse 3×3 discretization already archieves a relative error of less than 1%. For a more suitable 10×10 NURBS discretization that is comparable with the later simulations, the relative error between the numerical and the analytical solution is below 0.12%.

In anticipation of the later examples, mesh convergence is also studied for two already sintered spheres under tension. It is less common but particularly serves as a characteristic basis for the subsequent investigations. The spheres have a radius of $R = 2.5$ mm and the contact radius between them is $r = 0.55$ mm, see Fig. 3.4 a). A homogeneous mesh is employed with discretizations between 10×10 and 40×40, increased by increments of 5×5. The force-displacement curves and the final force values (Fig. 3.4 b) and c)) tend to converge but not monotonically. The alternating behaviour can be explained by the initially coarse discretization of the sinter area. The sinter area is discretized by only one element for the coarsest case and does not refine by the same steps as the spheres. Focusing hence only on more accurate approximations of the sinter area, the deviation between the finer discretizations (30×30 to 40×40) remains in the range of a few percent. The subsequent examples are therefore set up with discretizations of at least that range or finer.

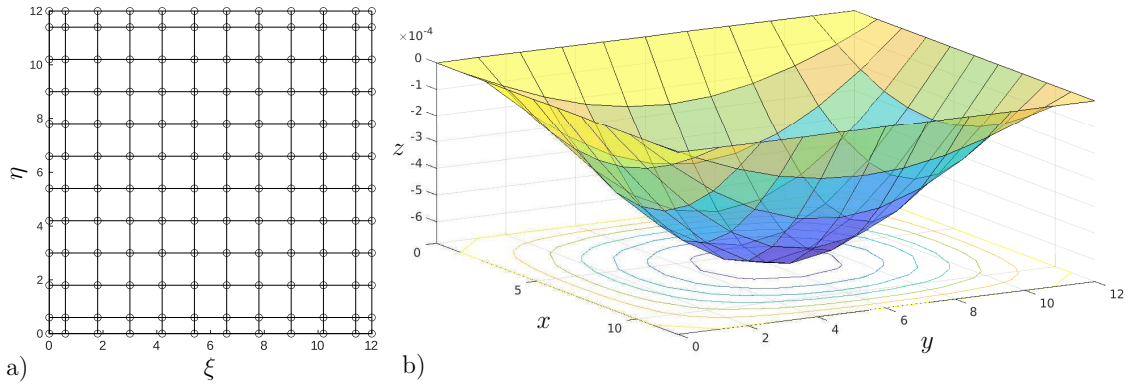

Figure 3.3: Square plate under sinusoidal pressure. a) Homogeneous 10×10 discretization, presented in parameter space. b) Deformed configuration in Cartesian coordinates.

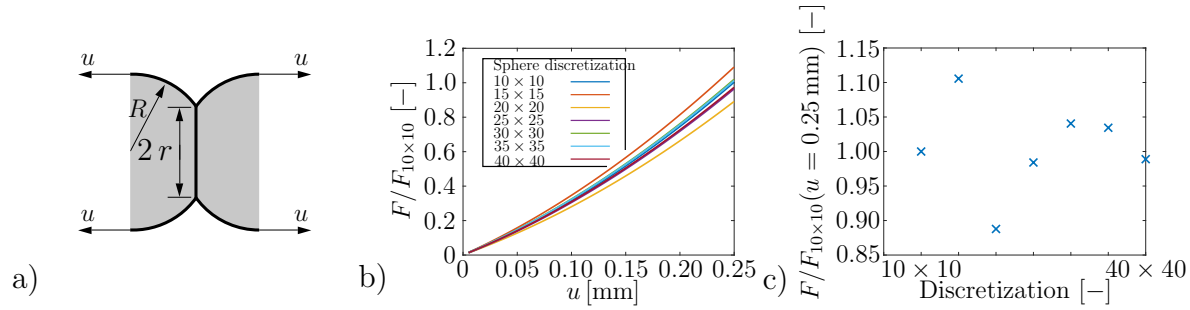

Figure 3.4: a) Schematic setup of a tensile test on two hollow spheres after sintering. b) Force-displacement curves normalized by the force of the 10×10 discretization, c) forces at final displacement for different discretizations normalized by the force of the 10×10 discretization.

3.5 Numerical examples of thermo-mechanically loaded hollow spheres

The presented framework is applied to hollow spheres as an illustrative example for the thermo-mechanical interactions with large strains. A first group of examples analyzes a single hollow sphere under various boundary conditions in Section 3.5.1. A second group of examples investigates the response of hollow sphere pairs after sintering in Section 3.5.2, with a focus on particular opportunities and limitations of the IGA description. While the problem is clearly motivated by metallic hollow sphere structures, the analysis spans a wider range of dimensionless parameter variations to better highlight the individual, competing thermo-elastic influences and to generally assess the capabilities and limitations of the numerical framework.

3.5.1 Single hollow spheres in various confinements

3.5.1.1 Boundary value problems and numerical setup of the single hollow sphere

The basic setting consists of a single hollow sphere to investigate its thermal expansion in various confinements, see Fig. 3.5 for a visualization. In all cases, the boundary conditions are chosen such that rigid body motions are suppressed. The translation at the lowest point of the sphere is fixed in all directions. The highest point of the sphere is constrained in x and y direction, still allowing the sphere to increase and decrease in size. Finally, a third point in the x-z-plane is constrained in its y translation, prohibiting the rotation of the sphere. Combinations of point and line loads mimic adjacent spheres or other bodies that may constrain the sphere thermally or mechanically. The temperature of the equinoctial line ($\theta_e(t)$) is first raised while other regions are subsequently cooled ($\theta_c(t)$) and optionally fixed. More specifically, the load steps are over time t

thermal boundary conditions

- $t_0 \rightarrow t_1$: initial heating at its equinoctial line until equilibrium
- $t_1 \rightarrow t_2$: temperature constant at equinoctial line, but cooling at specified regions
  - at four points
  - or at two rings
- $t_2 \rightarrow t_{\text{end}}$: all temperatures kept constant until thermo-mechanical equilibrium is reached

mechanical boundary conditions

- $t_0 \rightarrow t_{\text{end}}$: variations of mechanical boundary conditions at cooled regions for entire duration
  - no additionally prescribed displacement
  - additional fixation in vertical z-direction
  - additional fixation in all x,y,z-directions

The variations of the cooling positions (four points vs. two rings) and three displacement conditions (none vs. z-direction vs. x,y,z-direction) yield six different combinations. All prescribed temperature changes moreover occur linearly in time.

The thickness-to-radius ratio is $s_0/R_0 = 1/100$. Symmetry is employed for the simulations by considering eighths of the total sphere, also cf. Fig. 3.1 b). C^1-continuity is ensured for the symmetry boundary conditions. All elements are quadratic and the eighth batch of the sphere is discretized by 34×34 elements with a time stepping of $\Delta t = 1/10$ seconds. It shall be emphasized that the ξ^2-parametrization collapses in the uppermost point, which is why singularities are captured numerically, e.g., by evaluating terms of stresses or their orientations only close to the singular apex. With a focus on the capabilities of the IGA-based modeling approach, the set of parameters is chosen to trigger the different mechanical and thermal responses with equal sensitivity. Detailed numerical values of the material parameters are provided in Tab. 3.1.

Parameter	Symbol	Value	Unit
Young's Modulus (bulk)	E	1.2e6	[kg m^{-1} s^{-2}]
Poisson's ratio (bulk)	ν	0.3	[-]
Wall thickness	s	0.1	[mm]
First 2D Lamé parameter	λ	39.6	[kg s^{-2}]
Second 2D Lamé parameter	μ	46.2	[kg s^{-2}]
Thermal conductivity	κ	1	[kg m K^{-1} s^{-3}]
Heat capacity	c_d	0.01	[J K^{-1}]
Thermal expansion	α	6e-3	[K^{-1}]
Coupling parameter	c_1	1.03	[kg s^{-2} K^{-1}]
Coupling Parameter	c_2	0.01	[kg s^{-2} K^{-2}]

Table 3.1: Material parameters used for the simulations of the hollow spheres.

The $J_2^{\boldsymbol{E}}$ invariant of strains $\boldsymbol{E}$ will be chosen for illustration in Fig. 3.5, because of its distinguishable appearance in the resulting deformation fields and its relevance for locating regions prone to plastic yielding in later applications (in line with J_2 von Mises plasticity). It is moreover evaluated at three points in thickness direction, the inner sphere surface, the middle and the outer surface. The strain distribution in thickness direction $\xi^3 \in [-s/2; s/2]$ is approximated for that reason by following [91] as

$$E_{\alpha\beta} = E^{*1}_{\alpha\beta} + \xi^3 E^{*2}_{\alpha\beta} + (\xi^3)^2 E^{*3}_{\alpha\beta} \tag{3.68}$$

with

$$E^{*1}_{\alpha\beta} = \frac{1}{2}(\boldsymbol{a}_\alpha \cdot \boldsymbol{a}_\beta - \boldsymbol{A}_\alpha \cdot \boldsymbol{A}_\beta), \tag{3.69}$$

$$E^{*2}_{\alpha\beta} = \frac{1}{2}(\boldsymbol{a}_\alpha \cdot \boldsymbol{n}_{,\beta} + \boldsymbol{a}_\beta \cdot \boldsymbol{n}_{,\alpha} - \boldsymbol{A}_\alpha \cdot \boldsymbol{N}_{,\beta} + \boldsymbol{A}_\beta \cdot \boldsymbol{N}_{,\alpha}), \tag{3.70}$$

$$E^{*3}_{\alpha\beta} = \frac{1}{2}(\boldsymbol{n}_{,\alpha} \cdot \boldsymbol{n}_{,\beta} - \boldsymbol{N}_{,\alpha} \cdot \boldsymbol{N}_{,\beta}). \tag{3.71}$$

For the current settings, the last term in (3.68) is negligibly small due to the thin-walled geometry.

3.5.1.2 Resulting deformation of thermo-mechanically loaded single hollow spheres

The sphere first expands during the initial heating at the equinoctial line and then adapts to the various boundary conditions in the quasi-static setting without inertial effects, see Fig. 3.5 for the boundary conditions and final temperature and strain fields. A subsequent cooling at four points results in local stress concentrations that flatten the initially spherical shape (first row in Fig. 3.5). Adding displacement boundary conditions to the four points results in slight kinks (second and third row in Fig. 3.5), because the fixation counteracts the contraction induced by the decreased temperature. The $J_2^{\boldsymbol{E}}$ values accordingly show concentrations around these points.
A cooling of the top and bottom poles and an overall oblate shape emerges if the cooling is distributed along circumferential lines (fourth row in Fig. 3.5). When fixed in z-direction, the top and bottom poles are even allowed to contract into practically flat ends. It results in a ton-like shape, for which the cooled lines seperate the distinctive thermal fields of cool caps and a warmer mantle. The $J_2^{\boldsymbol{E}}$ values increase particularly at the regions of largest curvature, the equator and the kinked transition to the flat top and bottom. Buckling is even observed for cooled circumferential lines in case their displacements are fixed in all directions. It becomes noticable in the form of wrinkles [151] and alternating inner and outer strain fields that match the employed symmetry conditions of the present setup. Such severe deformations are unique for thin shells when compared to bulk spheres. It can make them candidates for scenarios where large deformations are needed, for instance, as parts of soft actuators [68]. These predictions benefit from the geometric accuracy of the IGA method within a geometrically non-linear framework to capture a single hollow sphere in different thermo-mechanical environments.

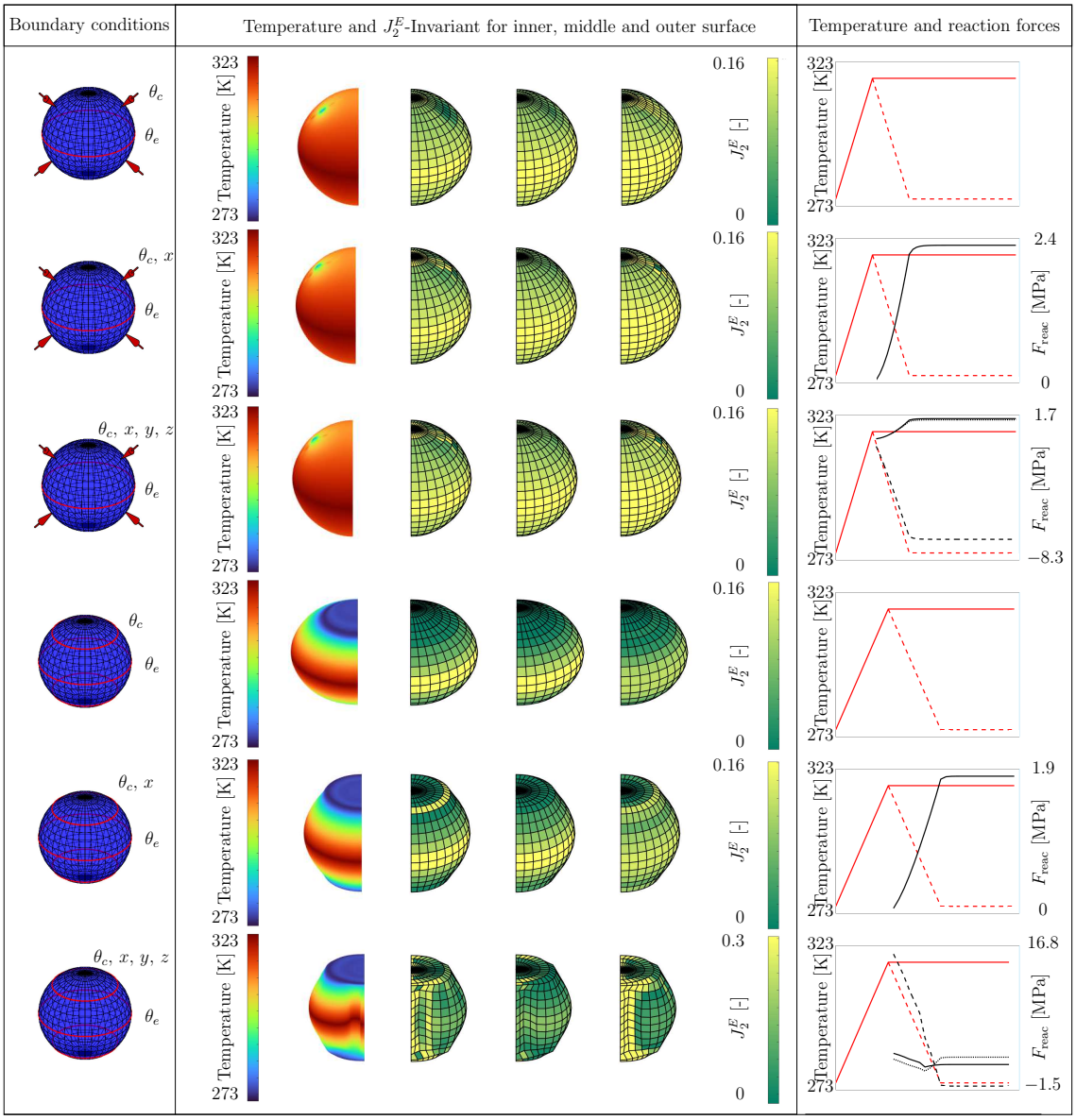

Figure 3.5: Single hollow spheres in various confinements: boundary conditions, temperature and strain fields, and temperature with reaction forces at prescribed boundaries. The last column shows the temperature evolution at the equinoctal line (solid red), the additional boundary condition (dashed red line) and for the reaction forces at one control point of the boundary conditions in x, y, z direction (dotted, dashed, solid black line), if applicable.

3.5.2 Thermo-elastic behavior of two sintered hollow spheres

3.5.2.1 Boundary value problem and numerical setup of two sintered hollow spheres

Following well-known benchmark studies of two sintered particles, we continue by the investigation of the thermo-mechanical response of two sintered hollow spheres. This scenario allows to assess the capabilities of an IGA formulation even better due to the more complex geometric combination of a flat sintered surface with the curved spheres. The sinter process is first simulated to obtain the starting system, before the mechanical and then the thermal response is analyzed. The implementation details and discussions follow in the next subsections. The starting point are two spheres with a thickness-to-radius ratio of $s_0/R_0 = 1/50$. Compared to the single hollow sphere above, this ratio is doubled to better distinguish the individual thermo-mechanical responses. Otherwise, the material parameters are the same as in the previous simulations, see Tab. 3.1.

Special emphasis is put on two new geometric variations, namely, the sintered contact area and the aspect ratio of the former spheres. In terms of dimensionless numbers, we will vary the ratio of sinter radius to sphere radius r_0/R_0 and the aspect ratio of sphere radius to elongated radius R_0/L_0, see Fig. 3.6 a). L_0 changes the initial spheres into spheroids.

3.5.2.2 Mechanical response of two sintered hollow spheres

The stiffness of two sintered hollow spheres is first analyzed from tensile tests loaded along their sinter axis. It connects to the benchmark problem already depicted in Fig. 3.4 a) and can serve as a representative volume element (RVE) of a perfectly periodic packing. Hollow spheres can be candidates for light-weight design, which is why the relationship between the effective density and the tensile stiffness shall be the mechanical values of interest, here. For this reason, we vary the sphere radius $R_0 \in \{2.5, 5.0, 7.5\}$ [mm] and the sinter radius by the ratio of $r_0/R_0 \in \{0.10, 0.15, 0.20\}$. Both radii can be controlled parameters during fabrication for the resulting density and the stiffness. The density is defined as the mass of the hollow spheres in relation to the bounding box in the sintered configuration and normalized with respect to the material's density. The effective tensile stiffness of the sintered system is defined as the starting derivative of the force-displacement curve. These variables are made dimensionless by combinations of Young's modulus E, radius R_0 and elongated radius L_0, see Fig 3.6.

Two main characteristics can be recovered for the present settings, when comparing the impact of initial sphere radius (R_0 is constant along dotted lines in Fig 3.6 c)) and that of the sinter radius (ratio r_0/R_0 is constant along dashed lines). On the one hand, the sinter radius has a stronger impact on the initial stiffness than the sphere radius (slope of dotted lines significantly larger than the dashed lines). On the other hand,

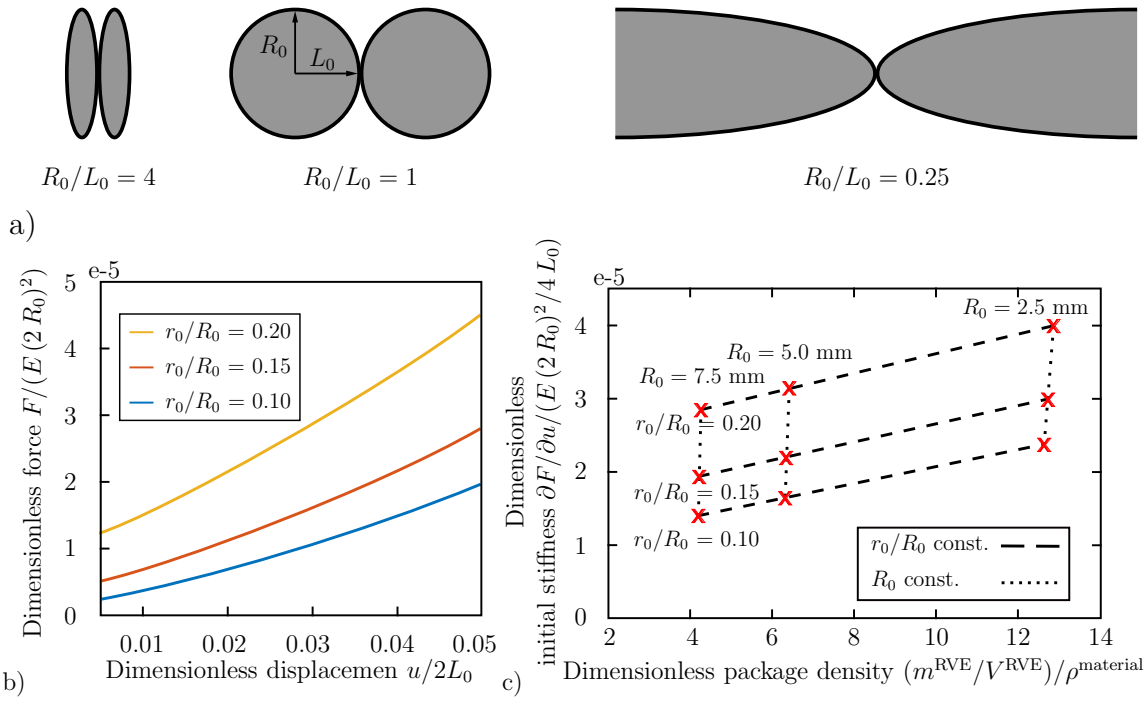

Figure 3.6: Two sintered hollow spheres: a) Visualization of different aspect ratios of the spheroids. b) Force-displacement curves for different ratios of sinter radius to sphere radius. c) Linearized stiffness over density for different sphere and contact radii.

the sphere radius mainly dictates the density of the structure. It is thus advised to use larger ratios of sinter radius to sphere radius (r_0/R_0) to achieve light-weight, high-stiffness structures. The distinct sensitivities moreover indicate that sinter radius and sphere radius are candidates for specifically tuning the stiffness and density, respectively. These findings also do not change qualitatively when taking into account the non-linear response of the present prototype model.

Altering the aspect ratio R_0/L_0 of the spheres shows that longer spheres increase the stiffness, when keeping the reference radius R_0 constant, see Fig. 3.7. This can be explained by a higher resistance against stretching for the elongated spheroids based on in-plane elasticity, while shorter ones tend to yield by a bending motion. This interface-related competition of deformation mechanisms is unique to hollow spheres and matches the decomposition into membrane and bending contribution in the theoretical derivation in (3.38). The largest sensitivity in terms of stiffness occurs for the spherical shape. This region coincides with the greatest changes in curvature and thus marks the transition from bending to stretching in the mechanically loaded regions. A saturation is reached for strongly elongated spheroids, though, that are expected to be dominated by the in-plane stretching resistance of the two longest sides. Very similar trends are observed for all three variations of the sinter radius and of the reference sphere radius in Fig. 3.7. A linear log-log relationship between stiffness and aspect ratio can even be well approximated for aspect ratios $1/4 \leq R_0/L_0 \leq 2/1$. The coefficients of determination

for the linear regression lie above 95 % for all settings, see Tab. 3.2. These results thus show that an anisotropic design can be favorable along a wider design space if the load direction is known.

From a numerical perspective, it is worth noting that the IGA shows great potential for exploiting the geometric approximation capabilities. The NURBS-based shape functions with C^1-continuity allow an efficient geometry study with few elements. Three geometric features govern the present system: the left/right curvature of the spheroids ($\approx 1/R_0$), their top/bottom curvature ($\approx 1/L_0$) and the size of the sinter area (curvature $\approx 1/r_0$). The shorter spheroids $L_0 > R_0$ benefited the most from the present discretization that is equally distributed in all circumferential directions, because the changing top/bottom curvature still remained well approximated with the chosen polynomial degrees. The elongated spheroids ($L_0 > R_0$) were approximated by more elements per side than necessary (and hence less efficiently), because a finer overall resolution was already dictated by the sinter radius. The curvature of the sinter area dominated the resolution requirement of the sphere curvature due to $r_0/L_0 \ll 1$. Future extensions may be based on these observations to locally adapt to the different requirements of the sinter area and the curvature of the spheroids.

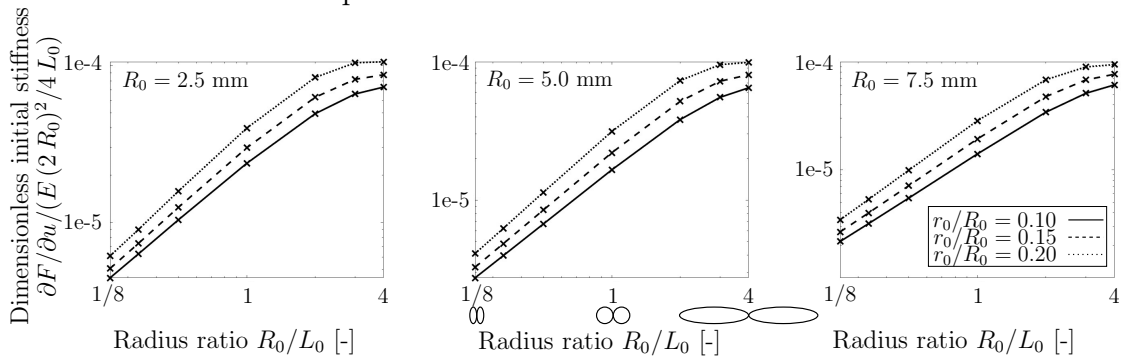

Figure 3.7: Two sintered hollow spheres: Initial stiffness over aspect ratio R_0/L_0 on a log-log-scale.

	$r_0/R_0 = 0.10$	$r_0/R_0 = 0.15$	$r_0/R_0 = 0.20$
$R_0 = 2.5\,\text{mm}$	2.4202 e-5 (0.9935)	3.0640 e-5 (0.9895)	4.0859 e-5 (0.9856)
$R_0 = 5.0\,\text{mm}$	1.8197 e-5 (0.9776)	2.4479 e-5 (0.9712)	3.4573 e-5 (0.9677)
$R_0 = 7.5\,\text{mm}$	1.6061 e-5 (0.9671)	2.2256 e-5 (0.9611)	3.2017 e-5 (0.9607)

Table 3.2: Two sintered hollow spheres: Slope and coefficient of determination (in brackets) for linear regression of the log-log domain of aspect ratio and stiffness between $1/4 \leq R_0/L_0 \leq 2/1$ in Fig. 3.7.

3.5.2.3 Thermal response of two sintered hollow spheres

The system of two sintered hollow spheres is eventually investigated for changing temperatures. The ratio of sinter radius to sphere radius is 0.5/5 and the ratio of thickness

to sphere radius is $s_0/R_0 = 0.1/5$. Further geometric variations are omitted, because they do not change the qualitative results and in order to focus on the thermally induced response. Instead, we employ three different boundary conditions to examine: freely expanding spheres, constrained spheres and spheres with a tensile pre-deformation, cf. Fig. 3.8. The boundary conditions are applied to the bisectors of the spheres. This allows to better illustrate the temperature and stress fields around the sinter contact. Moreover, the top and bottom are subject to C^1 symmetry conditions (or a horizontal tangent of the geometry) as they would be imposed by contact in a confinement or packing. The temperature is fixed on the circumferential right boundary and raised by 5 K on the left one. The key values of interest are the temperature distribution and the $J_2^{\boldsymbol{S}}$ stress invariant as a complementary alternative to the previously monitored strain values (again, in line with von Mises yield stress).

The freely deforming setting shows an anticipated expansion of the heated side and thus an increase of the radius (top of Fig. 3.8). A small portion of this expansion is mechanically transferred to the right sphere via the sintering contact, even though no thermal changes would induce an expansion at the right boundary. In agreement with the single sphere response in Fig. 3.5, the stresses are just weakly effected at the free area of the spheres, while the strongest influence is observed at curved features. The latter occur at the sinter area and the left boundary condition, which mimics contact with a confinement by C^1-continuity and competes with the thermally induced expansion.

When restricting the horizontal displacement, the temperature-induced inflation causes a much stronger evolution of the sintered area (middle of Fig. 3.8). This also induces large curvature changes and thus bending effects with significantly larger stress values. A denser packing due to mechanical constraints hence induces larger pre-stresses in contact zones and the sintered regions, which can impose a potential risk for production and operation of hollow-sphere sructures.

When applying a longitudinal displacement prior to heating, the spheres contract laterally (bottom of Fig. 3.8). The induced stress fields are hence comparably larger due to pre-stretching than due to temperature changes, which makes a quantitative comparison more difficult. The stretching yields a stress localization at the initially sintered area. Despite the mechanically higher stress impact, however, the subsequent heating still causes the left sphere to exceed its initial radius at the left edge. Also still in agreement with the previous findings, the pre-stretched conditions again affect the stress evolution especially at the contact and sintered regions, which are most prone to plastic yield or potential structural failure.

3.6 Conclusion

Motivated by the capabilities of the emerging IGA approach, a thermo-mechanically coupled finite element framework was developed for finite deformations of shells. Its derivation connected the more general higher-gradient deformational mechanics to clas-

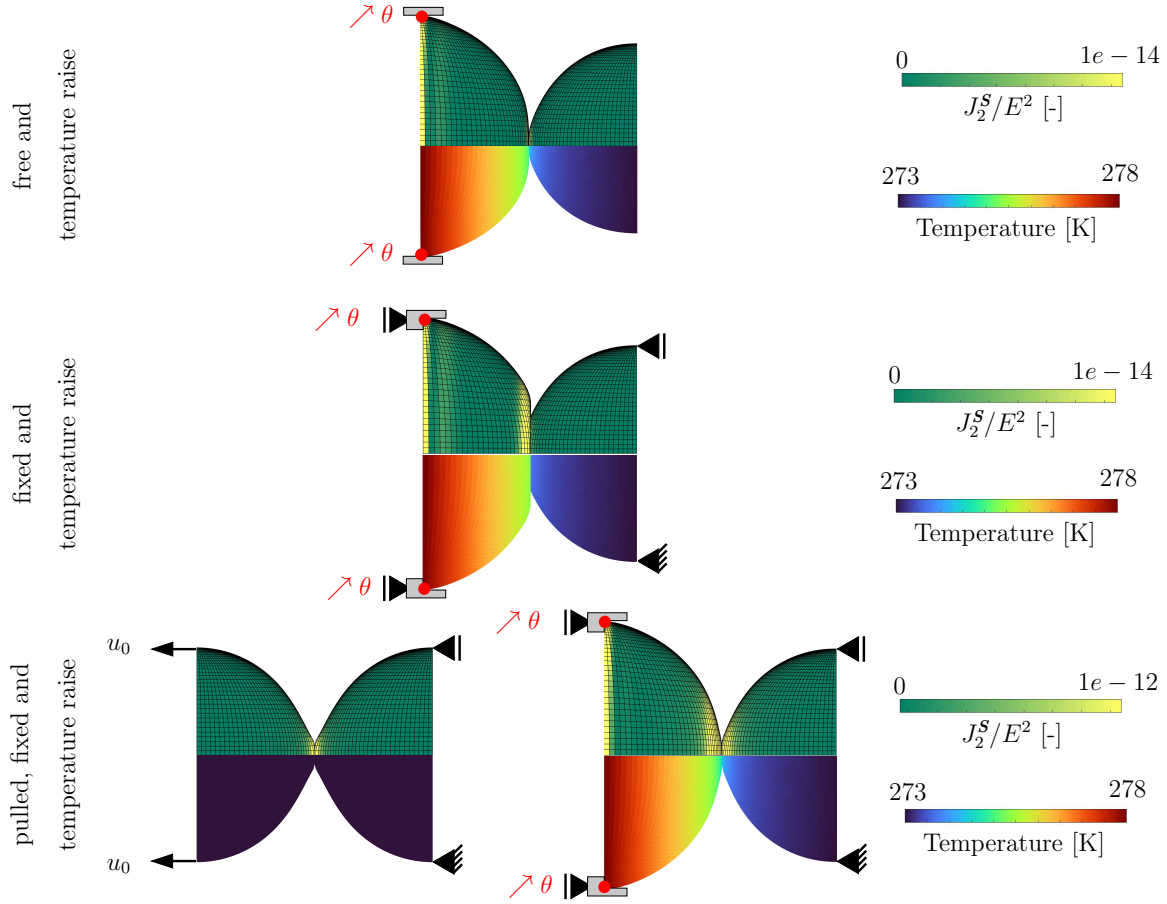

Figure 3.8: Two sintered hollow spheres: Temperature fields and stress invariant J_2^S normalized by E^2 subject to a temperature raise under different constraints.

sic shell theory and subsequently allowed for an efficient IGA description of thermoelastic shells. The simulation of a single sphere under transient mechanical and thermal boundary conditions showed that even a moderate number of patches predicts the complex deformation patterns of kinking or wrinkling well within the IGA framework. The sintered stage of two spheroids with varying aspect ratios has been simulated by mimicking the contact evolution of a generalized pseudo-sinter process. The sintered spheroid pair shows an elastic resistance that ranges between wall stretching (stiffer) and bending (softer), depending on aspect ratio and load orientation. Stresses especially concentrate at confinement zones and the sintered regions, where bending perturbations are often induced by the coupled thermal and mechanical stimuli.

It should be noted that the IGA not only allows to easily vary material coefficients, but also variations of curvature features without the need of relevant remeshing. Such efficient geometric variations can hence strongly support future design studies of hollow sphere structures in terms of stiffness, density and stress peaks during thermal expansion. From the viewpoint of thermomechanical modeling, future work shall focus on

inelastic material behavior and adaptive mesh refinement of regions with largest curvature. Experimental benchmarks will be moreover required to account for the unique diffusion times in practical thin-sphere sintering. The present work aims at providing a numerical basis for an efficient further exploration of hollow curved structures.

4 Coupling of the phase field approach to the Armstrong-Frederick model for the simulation of ductile damage under cyclic load

This chapter cites the paper "Coupling of the phase field approach to the Armstrong-Frederick model for the simulation of ductile damage under cyclic load" by S. Aygün, T. Wiegold and S. Klinge.

Abstract

The present contribution proposes a thermodynamically consistent model for the simulation of the ductile damage. The model couples the phase field method of fracture to the Armstrong-Frederick plasticity model with kinematic hardening. The latter is particularly suitable for simulating the material behavior under a cyclic load. The model relies on the minimum principle of the dissipation potential. However, the application of this approach is challenging since potentials of coupled methods are defined in different spaces: The dissipation potential of the phase field model is expressed in terms of rates of internal variables, whereas the Armstrong-Frederick model proposes a formulation depending on thermodynamic forces. For this reason, a unique formulation requires the Legendre transformation of one of the potentials. The present work performs the transformation of the Armstrong-Frederick potential, such that final formulation is only expressed in the space of rates of internal variables. With the assumption for the free energy and the joint dissipation potential at hand, the derivation of evolution equations is straightforward. The application of the model is illustrated by selected numerical examples studying the material response for different load constellations and sample geometries. The paper provides a comparison with the experimental results as well.

4.1 Introduction

Fatigue failure significantly influences the safety measures during the service life of engineering structures. It particularly holds for structures subjected to alternate loading with high amplitudes, which is an often situation when speaking of transportation vehicles. Dependent on the number of cycles and load amplitude, the interplay of the brittle and ductile failure takes place.However, the present contribution focuses on the low cycle fatigue where the role of plasticity is essential. The high complexity of the ductile damage under the cyclic load strongly motivates the virtual testing of materials on the basis of the computer simulations. The present work envisages a coupling of the phase field method of fracture to the Armstrong-Frederick model of plasticity with the kinematic hardening to this end.

The base for the phase field model of fracture has been set in the work by Francfort and Marigo [58] proposing the formulation of brittle fracture based solely on Griffith's idea of competition between elastic and fracture energy. This work initiated a large group of further contributions related to the numerical implementation of the concept proposed (Bourdin and Chambolle, [29]; Negri and Paolini, [113]; Fraternali, [59]; Schmidt et al., [130]). Amongst others, Ambrosio-Tortorelli regularizations have become ubiquitous (Ambrosio and Tortorelli, [10], [9]; Bourdin et al., [30]). These approaches are nowadays known as phase-field models of fracture and share several common features with the approaches resulting from Ginzburg-Landau models for phase transition (Karma et al., [85]). These regularizations have been applied to a wide variety of fracture problems including fracture of thermal and drying cracks (Maurini et al., [104]; Bourdin et al., [33]), ferro-magnetic and piezo-electric materials (Abdollahi and Arias, [1]; Wilson et al., [160]) and hydraulic fracturing (Bourdin et al., [32]; Wheeler et al., [155]; Wilson and Landis, [159]). These models also been enhanced to account for cohesive effects (Crismale and Lazzaroni, [42]; Freddi and Iurlano, [60]), ductile behavior (Alessi et al., [3]; Miehe et al., [107]; Ambati et al., [7]), large deformations (Ambati et al., [8]; Miehe et al., [108]; Borden et al., [28]), quasi-brittle damage (Narayan and Anand, [112]) and anisotropy (Li et al., [98]).

Some of previous works have also considered coupling of plasticity to the phase field method (Alessi et al., [3]; Ambati et al., [7],[8]; Borden et al., [28]; Miehe et al., [108], [107]). However, the current contribution will focus more precisely on the plasticity under the cyclic load where the Armstrong- Frederick model is a widely accepted concept (Bari and Hassan, [18]; Khan and Jackson, [88]; Kobayashi and Ohno, [92]; Puzrin and Houlsby, [121]). Some of the works in this field deal with so-called generalized representations, where either the classical Armstrong-Frederick model is extended to include several Armstrong-Frederick terms (Bari and Hassan, [18]), or where the application of multiple yield surfaces is envisaged (Puzrin and Houlsby, [121]). Another frequently used variant of the Armstrong-Frederick model has been presented by Ohno and Wang ([116]) and by Kobayashi and Ohno ([92]). The effects of the kinematic hardening are

nowadays also investigated within the framework of large deformations (Lührs et al., [102]; Svendsen et al., [140]; Lion, [100]; Mollica et al., [109]).

The Armstrong-Frederick model coupled to the phase field method is a promising approach inheriting the advantages of both incorporated techniques. However, the numerical implementation of this coupled approach brings with it several challenges such as the definition of a unique framework for both setups, the derivation of coupled evolution equations, the distinction between the tension and compression mode and certainly the development of the computationally efficient algorithm. Some of these issues are discussed in the present contribution which is structured as follows. An overview on the phase field method of fracture is presented in Sect. 4.2, whereas Sect. 4.3 introduces the Armstrong-Frederick model of plasticity. Furthermore, the Armstrong-Frederick evolution equations are derived by using two versions of the minimum principle of dissipation potential (Sects. 4.4 and 4.5). The concept for the coupling of two methods is presented in Sect. 4.6 and complemented by explaining the scheme for the calculation of the plasticity multiplier on the basis of the consistency condition (Sect. 4.7). Details on the numerical implementation including the global part and the material point part are presented in Sect. 4.8. Eventually, the paper also includes numerical examples simulating the tests with the uniformly increasing and the cyclic load. The contribution finishes with conclusions and an outlook.

4.2 Diffusive crack topology

The derivation of the coupled method requires a short recapitulation of separate approaches, which is done in two subsequent sections. Sect. 4.2 provides an overview of the phase field method, whereas Sect. 4.3 focuses on the Armstrong- Frederick model.

The present work uses the phase field framework proposed by Miehe and coworkers (Miehe et al., [108],[107]) as a basis. This approach supposes the diffusive (regularized) crack topology instead of the sharp crack topology leading to serious difficulties in the numerical implementation due to the lack of the continuity and differentiability. It relies on the evaluation of the damage variable d, which continuously changes in the range [0; 1], where zero-value corresponds to the intact material and the unity-value to the fully broken state, following a small strain setting. The approach starts by postulating an expression for the crack surface density function depending on the damage variable d

$$\gamma(d, \nabla d) = \frac{1}{2l} d^2 + \frac{l}{2} |\nabla d|^2, \tag{4.1}$$

which is furthermore used to define the total crack surface A for the entire body $\mathcal{B}$

$$A(d) = \int_B \gamma(d, \nabla d)\, dV. \tag{4.2}$$

An assumption that the crack propagation is a fully dissipative process yields to the conclusion that the constitutive dissipation potential has to be proportional to the rate of crack surface density

$$\Phi = g_c \dot{\gamma}(\dot{d}, \nabla\dot{d}, d, \nabla d), \tag{4.3}$$

where parameter g_c is related to the critical Griffith-type fracture energy and can be seen as a constitutive threshold value. However, this potential still does not guarantee that the damage is an increasing function. For this reason, the potential is extended by introducing the penalty term

$$P(\dot{d}) = \frac{k_\mathrm{p}}{2}\langle\dot{d}\rangle_-^2. \tag{4.4}$$

Here, the negative Macaulay brackets $\langle\bullet\rangle_- = (\bullet - |\bullet|)/2$ assure that the penalty term only activates for a negative damage evolution and the constant k_p has to be chosen as high as possible in order to stipulate the condition $\dot{d} \geq 0$. Along with the penalty term (4.4), the damage potential turns into

$$\Phi^d = \Phi + P(\dot{d}) = g_c \dot{\gamma}(\dot{d}, \nabla\dot{d}, d, \nabla d) + \frac{k_\mathrm{p}}{2}\langle\dot{d}\rangle_-^2. \tag{4.5}$$

In a further step, the model focuses on the definition of the free energy and its reduction on the basis of function $\omega = ((1-d)^2 + k_\mathrm{d})$. Here, the positive constant k_d prevents the energy to become identical to zero at a fully broken state. Moreover, the reduction function only affects the tension part of the energy which corresponds to the concept of the anisotropic degradation of energy

$$\Psi^\mathrm{d}(\boldsymbol{\epsilon}, d) = \omega(d)\Psi_+(\boldsymbol{\epsilon}) + \Psi_-(\boldsymbol{\epsilon}). \tag{4.6}$$

The additive split of the energy into a tension part $\Psi_+(\boldsymbol{\epsilon})$ and a compression part $\Psi_-(\boldsymbol{\epsilon})$, is of the special interest for simulating the cyclic behavior where the crack closure in the compression mode has to be considered. The definitions of the positive and negative energy parts of the free energy are based on the spectral decomposition of the small strain tensor

$$\boldsymbol{\epsilon}_\pm = \sum_i \langle\epsilon_i\rangle_\pm \boldsymbol{n}_i \otimes \boldsymbol{n}_i, \tag{4.7}$$

where $\boldsymbol{\epsilon}_i$ are the principal strains, $\boldsymbol{n}_i$ are the principal strain directions and i is the summation index. Equation (4.7) uses positive and negative Macaulay brackets. Positive

ones are defined as $\langle\bullet\rangle_+ = (\bullet + |\bullet|)/2$, whereas the negative ones have already been used in Eq. (4.4). The stresses corresponding to (4.7) are then defined as

$$\boldsymbol{\sigma} = \frac{\partial \Psi^{\mathrm{d}}}{\partial \boldsymbol{\epsilon}} = \omega(d)\boldsymbol{\sigma}_+ + \boldsymbol{\sigma}_- \tag{4.8}$$

such that it holds $\boldsymbol{\sigma}_\pm = \frac{\partial \Psi_\pm}{\partial \boldsymbol{\epsilon}}$. For a case of an isotropic material characterized by Lamé constants λ and μ, the energy spit turns into

$$\Psi_\pm(\boldsymbol{\epsilon}) = \frac{1}{2}\lambda \left(\mathrm{tr}\langle\boldsymbol{\epsilon}\rangle_\pm\right)^2 + \mu\, \mathrm{tr}\left(\langle\boldsymbol{\epsilon}\rangle_\pm^2\right) \tag{4.9}$$

with the corresponding equilibrium equation and stresses

$$\mathrm{Div}\left[\omega(d)\boldsymbol{\sigma}_+ + \boldsymbol{\sigma}_-\right] = \mathbf{0}, \tag{4.10}$$

$$\boldsymbol{\sigma}_\pm = \sum_i \left[\lambda\, \mathrm{tr}\langle\boldsymbol{\epsilon}\rangle_\pm + 2\mu\, \langle\epsilon_i\rangle_\pm\right] \boldsymbol{n}_i \otimes \boldsymbol{n}_i. \tag{4.11}$$

Since the free energy and the dissipation potential are known, the minimum principle of dissipation potential is used to derive the evolution equation for the internal parameter, namely

$$\min_{\dot{d}} \left(\mathcal{L}^{\mathrm{MDP}} = \dot{\Psi}^{\mathrm{d}}(\dot{\boldsymbol{\epsilon}}, \dot{d}) + \Phi^{\mathrm{d}}(d, \dot{d})\right) \quad \Rightarrow \quad \frac{g_c}{l}\left[d - l^2\Delta d\right] + \left[\omega' \Psi_+ + k_{\mathrm{p}}\langle\dot{d}\rangle_-\right] = 0. \tag{4.12}$$

The equilibrium equation (4.10) together with the evolution equation (4.12)b defines the strong problem of brittle fracture.

4.3 The Armstrong-Frederick kinematic hardening model

The Armstrong-Frederick kinematic hardening model (Armstrong and Frederick, [12]) is widely accepted to simulate the characteristic phenomena of the hardening behavior of metals, namely the Bauschinger and the ratcheting effect. Within the framework of the small strain plasticity, the formulation of the Armstrong-Frederick model starts with the typical assumption for the additive decomposition of strain tensor $\boldsymbol{\epsilon}$ into an elastic part $\boldsymbol{\epsilon}^{\mathrm{e}}$ and a plastic part $\boldsymbol{\epsilon}^{\mathrm{p}}$, namely $\boldsymbol{\epsilon} = \boldsymbol{\epsilon}^{\mathrm{e}} + \boldsymbol{\epsilon}^{\mathrm{p}}$. However, the description of the hardening effects requires the introduction of an additional strain-like internal variable $\boldsymbol{\xi}$. According to Lion (Lion, [100]), $\boldsymbol{\xi}$ relates to local viscoelastic deformations induced by dislocations. In rheological models, it is simulated as a damping element connected in series to an elastic spring. These are additionally coupled to a friction element in parallel (Dettmer and Reese, [48]). This internal variable is responsible for

the change of material stiffness depending on the loading history and is incorporated in the Helmholtz free energy, which now includes two parts: the elastic energy $\Psi^{\mathrm{el}}(\boldsymbol{\epsilon}^{\mathrm{e}})$ and free energy due to the hardening $\Psi^{\mathrm{hard}}(\boldsymbol{\xi})$, both in the quadratic form

$$\Psi^{\mathrm{AF}} = \Psi^{\mathrm{el}}\left(\boldsymbol{\epsilon}^{\mathrm{e}}\right) + \Psi^{\mathrm{hard}}(\boldsymbol{\xi}) = \frac{1}{2}\left(\boldsymbol{\epsilon} - \boldsymbol{\epsilon}^{\mathrm{p}}\right) : \mathbb{C} : \left(\boldsymbol{\epsilon} - \boldsymbol{\epsilon}^{\mathrm{p}}\right) + \frac{1}{2} c\, \boldsymbol{\xi} : \boldsymbol{\xi}. \tag{4.13}$$

Here, $\mathbb{C}$ is the fourth order elasticity tensor and c represents the kinematic hardening modulus. The Helmholtz free energy serves furthermore as a basis for the formulation of dissipation which, in the case of an isothermal process, only depends on the elastic power $(\boldsymbol{\sigma} : \dot{\boldsymbol{\epsilon}})$ and free energy rate $(\dot{\Psi}^{\mathrm{AF}})$

$$\mathcal{D} = \boldsymbol{\sigma} : \dot{\boldsymbol{\epsilon}} - \dot{\Psi}^{\mathrm{AF}} \geq 0. \tag{4.14}$$

In the concrete case of the Armstrong-Frederick model, the dissipation turns into:

$$\left(\boldsymbol{\sigma} - \frac{\partial \Psi^{\mathrm{AF}}}{\partial \boldsymbol{\epsilon}}\right) : \dot{\boldsymbol{\epsilon}} - \frac{\partial \Psi^{\mathrm{AF}}}{\partial \boldsymbol{\epsilon}^{\mathrm{P}}} : \dot{\boldsymbol{\epsilon}}^{\mathrm{p}} - \frac{\partial \Psi^{\mathrm{AF}}}{\partial \boldsymbol{\xi}} : \dot{\boldsymbol{\xi}} \geq 0, \tag{4.15}$$

which yields two groups of consequences. The first consequence is the constitutive law $\boldsymbol{\sigma} = \frac{\partial \Psi^{\mathrm{AF}}}{\partial \boldsymbol{\epsilon}}$, whereas the second consequence defines the driving forces of internal variables:

$$\boldsymbol{q}_{\boldsymbol{\epsilon}^{\mathrm{P}}} = -\frac{\partial \Psi^{\mathrm{AF}}}{\partial \boldsymbol{\epsilon}^{\mathrm{P}}} = \mathbb{C} : \left[\boldsymbol{\epsilon} - \boldsymbol{\epsilon}^{\mathrm{P}}\right] = \boldsymbol{\sigma}, \tag{4.16}$$

$$\boldsymbol{q}_{\boldsymbol{\xi}} = -\frac{\partial \Psi^{\mathrm{AF}}}{\partial \boldsymbol{\xi}} = -c\, \boldsymbol{\xi} = \boldsymbol{\chi}. \tag{4.17}$$

The later definition corresponds to the back stress and gives insight into the physical meaning of material parameter c. It is a proportionality constant relating the back stress $\boldsymbol{\chi}$ to the strain-like quantity $\boldsymbol{\xi}$. In analogy to the constitutive law of elastic materials, c represents the kinematic hardening modulus. A shorter notation for internal variables $\boldsymbol{\nu} = \boldsymbol{\epsilon}^{p}, \boldsymbol{\xi}$ and for corresponding driving forces $\boldsymbol{q} = \boldsymbol{\sigma}, \boldsymbol{\chi}$, together with the constitutive law for stresses, yields the result for the so-called reduced dissipation

$$\mathcal{D}^{\mathrm{red}} = \boldsymbol{q} : \dot{\boldsymbol{\nu}} = \boldsymbol{\sigma} : \dot{\boldsymbol{\epsilon}}^{\mathrm{p}} + \boldsymbol{\chi} : \dot{\boldsymbol{\xi}} \geq 0. \tag{4.18}$$

The Armstrong-Frederick model is eventually completed by introducing the yield locus formula

$$\Omega^{\mathrm{AF}} = \|\bar{\boldsymbol{\sigma}} - \bar{\boldsymbol{\chi}}\| - \bar{\sigma}_{\mathrm{Y}} = 0, \quad \bar{\sigma}_{\mathrm{Y}} = \sqrt{2/3}\boldsymbol{\sigma}_{\mathrm{Y}}, \tag{4.19}$$

where symbol $||\bullet|| = \sqrt{\bullet : \bullet}$ denotes the Frobenius norm, $\bar{\boldsymbol{\sigma}}$ and $\bar{\boldsymbol{\chi}}$ are deviatoric parts of stresses $\boldsymbol{\sigma}$ and back stresses $\boldsymbol{\xi}$ and σ_{Y} is the yield limit. Condition (4.19) defines the admissible set of driving forces yielding inelastic deformations.

4.4 Derivation of the evolution equations based on the minimum principle for the dissipation potential in terms of driving forces

The completion of the Armstrong-Frederick model previously described also requires the derivation of evolution equations which can be accomplished by using different concepts. One possibility is to follow the minimum principle of dissipation potential (MDP) as proposed in works by Dettmer and Reese ([48]) and by Aygün and Klinge ([15])

$$\min_{\boldsymbol{q}} \left(\mathcal{L}^{\mathrm{MDP}^*} = -\boldsymbol{q} : \dot{\boldsymbol{\nu}} + \Phi^{\mathrm{AF}^*}(\boldsymbol{\nu}, \boldsymbol{q}) \right), \tag{4.20}$$

$$\Phi^{\mathrm{AF}^*}(\boldsymbol{\nu}, \boldsymbol{q}) = a\|\bar{\boldsymbol{\sigma}} - \bar{\boldsymbol{\chi}}\| + \frac{1}{2b}\|\bar{\boldsymbol{\chi}}\|^2. \tag{4.21}$$

The dissipation potential (4.21) is inspired by the expression for the yield locus (4.19) but additionally includes a term depending on the norm of driving force $\boldsymbol{\chi}$. Symbols a and b denote material parameters. However, the subsequent derivations will show that parameter a does not influence the evolution equations, whereas parameter b plays an important role and represents pseudo-viscoelasticty. Superscript $*$ indicates that a formulation in terms of driving forces is chosen. The Lagrangian corresponding to the minimization problem (4.20) and (4.21) has the form

$$\mathcal{L}^{\mathrm{MDP}^*} = -\boldsymbol{\sigma} : \dot{\boldsymbol{\epsilon}}^{\mathrm{p}} - \boldsymbol{\chi} : \dot{\boldsymbol{\xi}} + \Phi^{\mathrm{AF}^*}(\boldsymbol{\nu}, \boldsymbol{q}), \tag{4.22}$$

which yields the following stationary conditions

$$\frac{\partial \mathcal{L}^{\mathrm{MDP}^*}}{\partial \boldsymbol{q}} = \begin{pmatrix} \frac{\partial \mathcal{L}^{\mathrm{MDP}^*}}{\partial \boldsymbol{\sigma}} \\ \frac{\partial \mathcal{L}^{\mathrm{MDP}^*}}{\partial \boldsymbol{\chi}} \end{pmatrix} = \begin{pmatrix} -\dot{\boldsymbol{\epsilon}}^{\mathrm{p}} + \frac{\partial \Phi^{\mathrm{AF}^*}}{\partial \boldsymbol{\sigma}} \\ -\dot{\boldsymbol{\xi}} + \frac{\partial \Phi^{\mathrm{AF}^*}}{\partial \boldsymbol{\chi}} \end{pmatrix} = \boldsymbol{0}. \tag{4.23}$$

The first equation in (4.23) determines the evolution of plastic strains and shows that the rate $\dot{\boldsymbol{\epsilon}}^{\mathrm{p}}$ is equal to the derivative of dissipation potential with respect to corresponding driving force: $\dot{\boldsymbol{\epsilon}}^{\mathrm{p}} = \frac{\partial \Psi^{\mathrm{AF}^*}}{\partial \boldsymbol{\sigma}} = \frac{\bar{\boldsymbol{\sigma}} - \bar{\boldsymbol{\chi}}}{\|\bar{\boldsymbol{\sigma}} - \bar{\boldsymbol{\chi}}\|}$. However, the received derivative is not uniquely defined and only contains the information on the direction of the ow of the plastic strains, not on the magnitude. For that reason, the right-hand side expression is scaled by the plastic multiplier λ which yields the standard solution

$$\dot{\boldsymbol{\epsilon}}^{\mathrm{p}} = \frac{\partial \Phi^{\mathrm{AF}^*}}{\partial \boldsymbol{\sigma}} = \lambda \frac{\bar{\boldsymbol{\sigma}} - \bar{\boldsymbol{\chi}}}{\|\bar{\boldsymbol{\sigma}} - \bar{\boldsymbol{\chi}}\|}. \tag{4.24}$$

The second equation in (4.23) determines the evolution of the internal variable $\boldsymbol{\xi}$. Here, the same argumentation as in Eq. (4.24) is used for the first term, whereas the second term is uniquely determined and does not need to be scaled with the multiplier λ

$$\dot{\boldsymbol{\xi}} = \frac{\partial \Phi^{\mathrm{AF}^*}}{\partial \boldsymbol{\chi}} = -\lambda \frac{\bar{\boldsymbol{\sigma}} - \bar{\boldsymbol{\chi}}}{\|\bar{\boldsymbol{\sigma}} - \bar{\boldsymbol{\chi}}\|} + \frac{1}{b}\bar{\boldsymbol{\chi}} = -\dot{\boldsymbol{\epsilon}}^{\mathrm{p}} + \frac{1}{b}\bar{\boldsymbol{\chi}} \quad \Rightarrow \quad \bar{\boldsymbol{\chi}} = b\left(\dot{\boldsymbol{\xi}} + \dot{\boldsymbol{\epsilon}}^{\mathrm{p}}\right). \tag{4.25}$$

Equations (4.24) and (4.25)a show the deviatoric character of internal variables $\boldsymbol{\epsilon}^{\mathrm{p}}$ and $\boldsymbol{\xi}$. Moreover, Eq. (4.25)b represents a constitutive law typical of a viscous material with the viscosity b. Finally, Eq. (4.17) along with Eq. (4.25)a provides the evolution equation for back stress $\boldsymbol{\chi}$ which can also be identified as a deviatoric quantity:

$$\dot{\boldsymbol{\chi}} = -c\dot{\boldsymbol{\xi}} = c\dot{\boldsymbol{\epsilon}}^{\mathrm{p}} - \frac{c}{b}\bar{\boldsymbol{\chi}} = \dot{\bar{\boldsymbol{\chi}}}. \tag{4.26}$$

The MDP-approach differs from the common approach treating the yield locus equation as a subsidiary condition within the Lagrange formalism of the constrained optimization. The main difference manifests itself in the evolution equations taking the form $\dot{\boldsymbol{n}}\boldsymbol{u} = \lambda \frac{\partial \Omega}{\partial \boldsymbol{q}}$ with λ as the Lagrange multiplier. An important advantage of the MDP-approach compared to the constrained optimization method is that it allows a standardized variable transformation, which is often a useful tool in coupling strategies.

4.5 Derivation of the evolution equations based on the minimum principle for the dissipation potential in terms of rates of internal variables

Both models summarized in Sects. 4.2 and 4.4 apply the minimum principle of dissipation potential. However, the phase field model uses a formulation in terms of the rate of internal variables, whereas the Armstrong-Frederick model minimizes the dissipation potential in terms of driving forces. Naturally, the coupling procedure requires a unique formulation in a single space. The present contribution deals with the approach in terms of velocities, such that the transformation of the potential $\Psi^{\mathrm{AF}^*}(\boldsymbol{\nu}, \boldsymbol{q})$ into the space of rates is necessary. This type of exchange is conducted on the basis of Legendre transformation (LT) defining the new potential as follows

$$\Phi^{\mathrm{AF}}(\boldsymbol{\nu}, \dot{\boldsymbol{\nu}}) = \max_{\boldsymbol{q}} \left\{ \mathcal{L}^{\mathrm{LT}} = \boldsymbol{q} : \dot{\boldsymbol{\nu}} - \Phi^{\mathrm{AF}^*}(\boldsymbol{\nu}, \boldsymbol{q}) \right\}, \tag{4.27}$$

$$\mathcal{L}^{\mathrm{LT}} = \boldsymbol{\sigma} : \dot{\boldsymbol{\epsilon}}^{\mathrm{p}} + \boldsymbol{\chi} : \dot{\boldsymbol{\xi}} - a\|\bar{\boldsymbol{\sigma}} - \bar{\boldsymbol{\chi}}\| - \frac{1}{2b}\|\bar{\boldsymbol{\chi}}\|^2. \tag{4.28}$$

The maximization procedure relies on two stationary conditions, the first of which gives a relationship for rates of plastic deformations

$$\frac{\partial \mathcal{L}^{\mathrm{LT}}}{\partial \boldsymbol{\sigma}} = \dot{\boldsymbol{\epsilon}}^{\mathrm{p}} - \lambda \frac{\bar{\boldsymbol{\sigma}} - \bar{\boldsymbol{\chi}}}{\|\bar{\boldsymbol{\sigma}} - \bar{\boldsymbol{\chi}}\|} = \mathbf{0}. \tag{4.29}$$

Bearing in mind that the multiplier λ is a scalar, Eq. (4.29) shows that rate $\dot{\boldsymbol{\epsilon}}^{\mathrm{p}}$ and difference $\bar{\boldsymbol{\sigma}} - \bar{\boldsymbol{\chi}}$ are coaxial. In other words, it holds that $\frac{\dot{\boldsymbol{\epsilon}}^{\mathrm{p}}}{||\dot{\boldsymbol{\epsilon}}^{\mathrm{p}}||} = \frac{\bar{\boldsymbol{\sigma}} - \bar{\boldsymbol{\chi}}}{||\bar{\boldsymbol{\sigma}} - \bar{\boldsymbol{\chi}}||}$. Moreover, the plastic flow only occurs if the stress state fulfills the yield locus equation (4.19) such that the norm $||\bar{\boldsymbol{\sigma}} - \bar{\boldsymbol{\chi}}||$ can be replaced by the yield limit $\bar{\sigma}_{\mathrm{Y}}$. Equation (4.29) is then rewritten as follows

$$\bar{\boldsymbol{\sigma}} - \bar{\boldsymbol{\chi}} = \bar{\sigma}_{\mathrm{Y}} \frac{\dot{\boldsymbol{\epsilon}}^{\mathrm{p}}}{\|\dot{\boldsymbol{\epsilon}}^{\mathrm{p}}\|} \quad \Rightarrow \quad \bar{\boldsymbol{\sigma}} = \bar{\sigma}_{\mathrm{Y}} \frac{\dot{\boldsymbol{\epsilon}}^{\mathrm{p}}}{\|\dot{\boldsymbol{\epsilon}}^{\mathrm{p}}\|} + \bar{\boldsymbol{\chi}}. \tag{4.30}$$

On the other hand, the second stationary condition

$$\frac{\partial \mathcal{L}^{\mathrm{LT}}}{\partial \boldsymbol{\chi}} = \dot{\boldsymbol{\xi}} + \lambda \frac{\bar{\boldsymbol{\sigma}} - \bar{\boldsymbol{\chi}}}{\|\bar{\boldsymbol{\sigma}} - \bar{\boldsymbol{\chi}}\|} - \frac{1}{b}\bar{\boldsymbol{\chi}} = 0 \quad \Rightarrow \quad \bar{\boldsymbol{\chi}} = b\dot{\boldsymbol{\xi}} + b\dot{\boldsymbol{\epsilon}}^{\mathrm{p}} \tag{4.31}$$

together with (4.30)b leads to the final expression for deviatoric stresses

$$\bar{\boldsymbol{\sigma}} = \bar{\sigma}_{\mathrm{Y}} \frac{\dot{\boldsymbol{\epsilon}}^{\mathrm{p}}}{\|\dot{\boldsymbol{\epsilon}}^{\mathrm{p}}\|} + b\dot{\boldsymbol{\xi}} + b\dot{\boldsymbol{\epsilon}}^{\mathrm{p}}. \tag{4.32}$$

Driving forces (4.31)b and (4.32) are now inserted into (4.28), which reads the desired dissipation potential in terms of the internal variables and their rates

$$\Phi^{\mathrm{AF}}(\boldsymbol{\nu}, \dot{\boldsymbol{\nu}}) = \bar{\sigma}_{\mathrm{Y}} \left\|\dot{\boldsymbol{\epsilon}}^{\mathrm{P}}\right\| + \frac{b}{2} \left\|\dot{\boldsymbol{\epsilon}}^{\mathrm{P}}\right\|^2 + \frac{b}{2}\|\dot{\boldsymbol{\xi}}\|^2 + b\dot{\boldsymbol{\epsilon}}^{\mathrm{p}} : \dot{\boldsymbol{\xi}}. \tag{4.33}$$

More details on derivation are presented in Appendix A. Result (4.33) now enables the formulation of the new minimization problem

$$\min_{\dot{\nu}} \left(\mathcal{L}^{\mathrm{MDP}} = \dot{\Psi}^{\mathrm{AF}} + \Phi^{\mathrm{AF}}(\boldsymbol{\nu}, \dot{\boldsymbol{\nu}}) \right), \quad \mathcal{L}^{\mathrm{MDP}} = \boldsymbol{\sigma} : \dot{\boldsymbol{\epsilon}} - \boldsymbol{\sigma} : \dot{\boldsymbol{\epsilon}}^{\mathrm{p}} - \boldsymbol{\chi} : \dot{\boldsymbol{\xi}} + \Phi^{\mathrm{AF}}(\boldsymbol{\nu}, \dot{\boldsymbol{\nu}}). \tag{4.34}$$

Bearing in mind the deviatoric character of quantities $\dot{\boldsymbol{\epsilon}}$ and $\dot{\boldsymbol{\xi}}$, the problem can also be written as:

$$\min_{\dot{\boldsymbol{\nu}}} \left(\mathcal{L}^{\mathrm{MDP}} = \dot{\Psi}^{\mathrm{AF}} + \Phi^{\mathrm{AF}}(\boldsymbol{\nu}, \dot{\boldsymbol{\nu}}) \right), \quad \mathcal{L}^{\mathrm{MDP}} = \boldsymbol{\sigma} : \dot{\boldsymbol{\epsilon}} - \bar{\boldsymbol{\sigma}} : \dot{\boldsymbol{\epsilon}}^{\mathrm{p}} - \bar{\boldsymbol{\chi}} : \dot{\boldsymbol{\xi}} + \Phi^{\mathrm{AF}}(\boldsymbol{\nu}, \dot{\boldsymbol{\nu}}). \tag{4.35}$$

Equation (4.35) is the counterpart of the MDP-problem (4.20) in terms of velocities and provides expressions for driving forces according to relationship $\boldsymbol{q} = \frac{\partial \Phi^{\mathrm{AF}}}{\partial \dot{\boldsymbol{\nu}}}$:

$$\boldsymbol{q}_{\boldsymbol{\epsilon}^{\mathrm{P}}} = \bar{\boldsymbol{\sigma}} = \frac{\partial \Phi^{\mathrm{AF}}}{\partial \dot{\boldsymbol{\epsilon}}^{\mathrm{P}}} = \bar{\sigma}_{\mathrm{Y}} \frac{\dot{\boldsymbol{\epsilon}}^{\mathrm{P}}}{\left\| \dot{\boldsymbol{\epsilon}}^{\mathrm{P}} \right\|} + b \dot{\boldsymbol{\epsilon}}^{\mathrm{P}} + b \dot{\boldsymbol{\xi}}, \tag{4.36}$$

$$\boldsymbol{q}_{\boldsymbol{\xi}} = \bar{\boldsymbol{\chi}} = \frac{\partial \Phi^{\mathrm{AF}}}{\partial \dot{\boldsymbol{\xi}}} = b \dot{\boldsymbol{\xi}} + b \dot{\boldsymbol{\epsilon}}^{\mathrm{P}}. \tag{4.37}$$

A transformation of the system (4.36) and (4.37) yields the evolution equations identical to the ones from Sect. 4.4 (Eqs. (4.24) and (4.25)):

$$\dot{\boldsymbol{\epsilon}}^{\mathrm{P}} = \lambda \frac{\bar{\boldsymbol{\sigma}} - \bar{\boldsymbol{\chi}}}{\| \bar{\boldsymbol{\sigma}} - \bar{\boldsymbol{\chi}} \|}, \quad \dot{\boldsymbol{\xi}} = -\dot{\boldsymbol{\epsilon}}^{\mathrm{P}} + \frac{1}{b} \bar{\boldsymbol{\chi}}. \tag{4.38}$$

Note that the insertion of (4.37) into (4.36) yields the intermediate result

$$\bar{\boldsymbol{\sigma}} = \bar{\sigma}_{\mathrm{Y}} \frac{\dot{\boldsymbol{\epsilon}}^{\mathrm{P}}}{\left\| \dot{\boldsymbol{\epsilon}}^{\mathrm{P}} \right\|} + \boldsymbol{\chi} \quad \Rightarrow \quad \bar{\boldsymbol{\sigma}} - \bar{\boldsymbol{\chi}} = \bar{\sigma}_{\mathrm{Y}} \frac{\dot{\boldsymbol{\epsilon}}^{\mathrm{P}}}{\left\| \dot{\boldsymbol{\epsilon}}^{\mathrm{P}} \right\|}, \tag{4.39}$$

which is only valid for $||\dot{\boldsymbol{\epsilon}}^{\mathrm{P}}|| \neq 0$. By taking the norm of (4.39)b, it follows that $||\bar{\boldsymbol{\sigma}} - \bar{\boldsymbol{\chi}}|| = \bar{\sigma}_{\mathrm{Y}}$. This consequence indicates that dissipation potential (4.33) intrinsically includes the yield locus condition. Accordingly, it can be summed up that the dissipation potential (4.33) describes the same problem as the dissipation potential (4.21) along with the yield locus function (4.19). Finally, the strong form corresponding to the Armstrong-Frederick problem can be recapitulated as follows:

$$\mathrm{Div}\, \boldsymbol{\sigma} = \mathbf{0}, \tag{4.40}$$

$$\boldsymbol{\sigma} = \mathbb{C} : (\boldsymbol{\epsilon} - \boldsymbol{\epsilon}^{\mathrm{p}}), \tag{4.41}$$

$$\dot{\boldsymbol{\epsilon}}^{\mathrm{p}} = \lambda \frac{\bar{\boldsymbol{\sigma}} - \bar{\boldsymbol{\chi}}}{\| \bar{\boldsymbol{\sigma}} - \bar{\boldsymbol{\chi}} \|}, \tag{4.42}$$

$$\dot{\boldsymbol{\chi}} = c \left(\dot{\boldsymbol{\epsilon}}^{\mathrm{p}} - \frac{1}{b} \bar{\boldsymbol{\chi}} \right), \tag{4.43}$$

$$\Omega^{\mathrm{AF}} = \| \bar{\boldsymbol{\sigma}} - \bar{\boldsymbol{\chi}} \| - \bar{\sigma}_{\mathrm{Y}} \tag{4.44}$$

$$\lambda \geq 0,\ \Omega^{\mathrm{AF}} \leq 0,\ \lambda \Omega^{\mathrm{AF}} = 0. \tag{4.45}$$

The previous system includes the equilibrium equation, the constitutive law, two evolution equations and the Karush-Kuhn-Tucker conditions defining the plastic domain.

Equation (4.43) is derived by using the time derivative of definition (4.17) and rate (4.38)b. The body forces in the equilibrium equation are neglected. Evolution equation (4.42) and Karush-Kuhn-tucker conditions depend on plastic multiplier λ which is typically determined from the consistency condition.

4.6 Coupling of the Armstrong-Frederick model to the phase-field approach

The coupling of the two methods starts by writing the Armstrong-Frederick energy in a form splitting the tension and compression part of elastic energy in order to introduce the damage influence as was done in Sect. 4.2

$$\Psi^{\mathrm{AF}}\left(\boldsymbol{\epsilon}^{\mathrm{e}}, \boldsymbol{\xi}\right) = \Psi^{\mathrm{el}}\left(\boldsymbol{\epsilon}^{\mathrm{e}}\right) + \Psi^{\mathrm{hard}}(\boldsymbol{\xi}) = \Psi_{+}^{\mathrm{el}}\left(\boldsymbol{\epsilon}^{\mathrm{e}}\right) + \Psi_{-}^{\mathrm{el}}\left(\boldsymbol{\epsilon}^{\mathrm{e}}\right) + \Psi^{\mathrm{hard}}\left(\boldsymbol{\xi}\right). \tag{4.46}$$

However, damage also influences the hardening energy in the case where the tension mode is active. For this reason, the present model introduces a function distinguishing the pure compression mode from the pure tension and from the mixed modes

$$\bar{\omega} = \begin{cases} \omega(d) & \text{if} \quad \max\left\{\left(\boldsymbol{\epsilon}_i\right)_{i=1,2,3}, 0\right\} > 0, \\ 1 & \text{if} \quad \max\left\{\left(\boldsymbol{\epsilon}_i\right)_{i=1,2,3}, 0\right\} \leq 0. \end{cases} \tag{4.47}$$

By using this new notation, the coupled free energy is written as

$$\Psi^{\mathrm{c}}\left(\boldsymbol{\epsilon}^{\mathrm{e}}, d, \boldsymbol{\xi}\right) = \omega\Psi_{+}^{\mathrm{el}}\left(\boldsymbol{\epsilon}^{\mathrm{e}}\right) + \Psi_{-}^{\mathrm{el}}\left(\boldsymbol{\epsilon}^{\mathrm{e}}\right) + \bar{\omega}\Psi^{\mathrm{hard}}\left(\boldsymbol{\xi}\right) \tag{4.48}$$

and corresponding constitutive laws take the form

$$\boldsymbol{\sigma} = \frac{\partial\Psi^{\mathrm{c}}}{\partial\boldsymbol{\epsilon}} = \omega\frac{\partial\Psi_{+}^{\mathrm{el}}}{\partial\boldsymbol{\epsilon}} + \frac{\partial\Psi_{-}^{\mathrm{el}}}{\partial\boldsymbol{\epsilon}} = \omega\boldsymbol{\sigma}_{+} + \boldsymbol{\sigma}_{-}, \tag{4.49}$$

$$\boldsymbol{\sigma}_{\pm} = \frac{\partial\Psi_{\pm}^{\mathrm{el}}}{\boldsymbol{\epsilon}} = \mathbb{C} : \boldsymbol{\epsilon}_{\pm}^{\mathrm{e}} = \mathbb{C} : \left\langle\boldsymbol{\epsilon} - \boldsymbol{\epsilon}^{\mathrm{p}}\right\rangle_{\pm}, \tag{4.50}$$

$$\boldsymbol{\chi} = \frac{\partial\Psi^{\mathrm{c}}}{\partial\boldsymbol{\xi}} = -\bar{\omega}c\boldsymbol{\xi}, \tag{4.51}$$

where the spectral decomposition of elastic strains has the standard form

$$\boldsymbol{\epsilon}_{\pm}^{\mathrm{e}} = \left(\boldsymbol{\epsilon} - \boldsymbol{\epsilon}^{\mathrm{p}}\right)_{\pm} = \sum_{i}\left\langle\boldsymbol{\epsilon}_{i}^{\mathrm{e}}\right\rangle_{\pm}\boldsymbol{n}_i \otimes \boldsymbol{n}_i = \sum_{i}\left\langle\left(\boldsymbol{\epsilon} - \boldsymbol{\epsilon}^{\mathrm{p}}\right)_i\right\rangle_{\pm}\boldsymbol{n}_i \otimes \boldsymbol{n}_i. \tag{4.52}$$

Bearing in mind stress definition (4.49), the equilibrium equation turns into

$$\mathrm{Div}\left[\omega(d)\boldsymbol{\sigma}_+ + \boldsymbol{\sigma}_-\right] = 0. \tag{4.53}$$

The damage influence on the dissipation functional related to the plastic deformations follows the same argumentation as in the case of the hardening energy, such that the coupled dissipation potential Φ^{c} consists of two terms where the second term is weighted by the function $\bar{\omega}$

$$\Phi^{c} = \Phi^{\mathrm{d}} + \bar{\omega}\Phi^{\mathrm{AF}}. \tag{4.54}$$

With the definitions (4.48) and (4.54), the minimization of the corresponding Lagrange function

$$\mathcal{L}^{\mathrm{MDP}} = \dot{\Psi}^{\mathrm{c}} + \Phi^{\mathrm{c}} = \dot{\Psi}^{\mathrm{c}} + \Phi^{\mathrm{d}} + \bar{\omega}\Phi^{\mathrm{AF}} \tag{4.55}$$

yields the following system of equations which, together with equilibrium equation (4.53), defines the strong form of the coupled problem

$$\boldsymbol{\sigma} = \omega(d)\boldsymbol{\sigma}_+ + \boldsymbol{\sigma}_-, \tag{4.56}$$

$$\dot{\boldsymbol{\epsilon}}^{\mathrm{p}} = \lambda\bar{\boldsymbol{N}}, \quad \bar{\boldsymbol{N}} = \frac{\bar{\boldsymbol{\sigma}} - \bar{\boldsymbol{\chi}}}{\|\bar{\boldsymbol{\sigma}} - \bar{\boldsymbol{\chi}}\|}, \tag{4.57}$$

$$\dot{\boldsymbol{\xi}} = \frac{1}{b\bar{\omega}}\bar{\boldsymbol{\chi}} - \dot{\boldsymbol{\epsilon}}^{\mathrm{p}}, \tag{4.58}$$

$$\dot{\boldsymbol{\chi}} = -\dot{\bar{\omega}}c\boldsymbol{\xi} + c\bar{\omega}\left(\dot{\boldsymbol{\epsilon}}^{\mathrm{p}} - \frac{1}{b\bar{\omega}}\bar{\boldsymbol{\chi}}\right), \tag{4.59}$$

$$\Omega^{\mathrm{c}} = \|\bar{\boldsymbol{\sigma}} - \bar{\boldsymbol{\chi}}\| - \bar{\omega}\bar{\sigma}_{\mathrm{Y}}, \tag{4.60}$$

$$\lambda \geq 0, \Omega^{\mathrm{c}} \leq 0, \lambda\Omega^{\mathrm{c}} = 0, \tag{4.61}$$

$$\frac{g_c}{l}\left[d - l^2\Delta d\right] + \left[\omega'\Psi_+^{\mathrm{el}} + \bar{\omega}'\Psi^{\mathrm{hard}} + k_{\mathrm{p}}\langle\dot{d}\rangle-\right] = 0. \tag{4.62}$$

Here, a shorter notation $\bar{\boldsymbol{N}} = \frac{\bar{\boldsymbol{\sigma}}-\bar{\boldsymbol{\chi}}}{\|\bar{\boldsymbol{\sigma}}-\bar{\boldsymbol{\chi}}\|}$ is introduced to denote the so-called direction tensor. Details on the derivation of evolution equations and of the yield criterion are provided in Appendix B.

4.7 Determination of the plastic multiplier

Evolution equation (4.57) and the Karush-Kuhn-Tucker conditions (4.61) depend on plastic multiplier λ which is commonly determined from the consistency condition $\lambda\dot{\Omega}^c = 0$. An appropriate form of this condition is obtained by taking the time derivative of the yield locus formula

$$\|\bar{\boldsymbol{\sigma}} - \bar{\boldsymbol{\chi}}\|^2 = \bar{\omega}^2\bar{\sigma}_{\mathrm{Y}}^2 \quad \Rightarrow \quad (\bar{\boldsymbol{\sigma}} - \bar{\boldsymbol{\chi}}) : (\dot{\bar{\boldsymbol{\sigma}}} - \dot{\bar{\boldsymbol{\chi}}}) = 0. \tag{4.63}$$

Since difference $(\bar{\boldsymbol{\sigma}} - \bar{\boldsymbol{\chi}})$ is deviatoric, the condition above also can be written as follows:

$$(\bar{\boldsymbol{\sigma}} - \bar{\boldsymbol{\chi}}) : (\dot{\boldsymbol{\sigma}} - \dot{\boldsymbol{\chi}}) = 0. \tag{4.64}$$

In a further step, the stress rate

$$\dot{\boldsymbol{\sigma}} = \omega'\boldsymbol{\sigma}_+ + \omega(d)\mathbb{C} : (\dot{\boldsymbol{\epsilon}} - \dot{\boldsymbol{\epsilon}}^{\mathrm{P}})_+ + \mathbb{C} : \left(\dot{\boldsymbol{\epsilon}} - \dot{\boldsymbol{\epsilon}}^{\mathrm{P}}\right)_- \tag{4.65}$$

along with Eqs. (4.57) and (4.59) is introduced in (4.64) which yields

$$(\bar{\boldsymbol{\sigma}} - \bar{\boldsymbol{\chi}}) : \left[\omega'\boldsymbol{\sigma}_+ + \omega\mathbb{C} : [\dot{\boldsymbol{\epsilon}} - \lambda\bar{\boldsymbol{N}}]_+ + \mathbb{C} : [\dot{\boldsymbol{\epsilon}} - \lambda\bar{\boldsymbol{N}}]_- + \dot{\bar{\omega}}c\boldsymbol{\xi} - c\bar{\omega}\lambda\bar{\boldsymbol{N}} + \frac{c}{b}\bar{\boldsymbol{\chi}}\right] = 0. \tag{4.66}$$

However, the split of the elastic strain rate into a positive and a negative part cannot be performed as a superposition of positive/negative parts of the total and plastic strains. For this reason, the previous equation can only be solved numerically by using an iterative procedure. For this purpose, the initial guess λ_0 is obtained by neglecting the terms including the stress rates

$$(\bar{\boldsymbol{\sigma}} - \bar{\boldsymbol{\chi}}) : \left[\omega'\boldsymbol{\sigma}_+ + \dot{\bar{\omega}}c\boldsymbol{\xi} - c\bar{\omega}\lambda_0\bar{N} + \frac{c}{b}\bar{\boldsymbol{\chi}}\right] = 0. \tag{4.67}$$

Thereafter, all subsequent steps follow the iteration rule for the calculation of the updated value λ_i

$$(\bar{\boldsymbol{\sigma}} - \bar{\boldsymbol{\chi}}) : \left[\omega'\boldsymbol{\sigma}_+ + \omega\mathbb{C} : \left[\dot{\boldsymbol{\epsilon}} - \lambda_{i-1}\bar{N}\right]_+ + \mathbb{C} : \left[\dot{\boldsymbol{\epsilon}} - \lambda_{i-1}\bar{N}\right]_- + \dot{\bar{\omega}}c\boldsymbol{\xi} - c\bar{\omega}\lambda_i\bar{\boldsymbol{N}} + \frac{c}{b}\bar{\boldsymbol{\chi}}\right] = 0. \tag{4.68}$$

The iterative process stops if the prescribed accuracy is achieved.

4.8 Numerical implementation

4.8.1 General approach

The minimum principle of dissipation potential along with the time-incremental variational principles represents an important tool for the numerical solution of boundary value problems. Within this concept, the Lagrange function $\mathcal{L}^{\mathrm{MDP}}$ corresponding to the body is integrated over a single time increment $[t_n; t_{n+1}]$. In its original form, this integral depends on external variables ($\boldsymbol{u}$), internal variables ($\boldsymbol{\nu}$) and on the rates of internal variables, so-called velocities $\dot{\boldsymbol{\nu}}$. However, the velocities can be replaced by the Euler-forward approximation $\dot{\boldsymbol{\nu}} = (\boldsymbol{\nu}_{n+1} - \boldsymbol{\nu}_n)/\Delta t$, where $\Delta t = t_{n+1} - t_n$ is the time increment. As a consequence, the result only depends on discrete values of external and internal variables such that the time integration is performed as follows

$$\int_{t_n}^{t_{n+1}} \int_\Omega \mathcal{L}^{\mathrm{MDP}} dV dt \approx \int_\Omega \left\{ \Psi\left(\boldsymbol{\epsilon}^{\mathrm{e}}_{n+1}, \boldsymbol{\nu}_{n+1}\right) - \Psi\left(\boldsymbol{\epsilon}^{\mathrm{e}}_{n}, \boldsymbol{\nu}_{n}\right) + \Delta t \Phi\left(\boldsymbol{\nu}_{n+1}, \left(\boldsymbol{\nu}_{n+1} - \boldsymbol{\nu}_{n+1}\right)/\Delta t\right) \right\} dV. \quad (4.69)$$

Here, displacement $\boldsymbol{u}$ is the only external variable since an isothermal process is considered. In a further step, the minimization with respect to the displacements and internal variables in the current time step $n+1$ yields the sought solution. Within this procedure, term $\Psi(\boldsymbol{\epsilon}^{\mathrm{e}}_n, \boldsymbol{\nu}_n)$ can be neglected since it only depends on values in the previous time step n. By adding the potential of external forces $l(t_{n+1}, u_{n+1})$ in (4.69), the new, combined Lagrangian is constructed

$$\mathcal{L}^{\mathrm{comb}} = \int_\Omega \left\{ \Psi\left(\boldsymbol{\epsilon}^{\mathrm{e}}_{n+1}, \boldsymbol{\nu}_{n+1}\right) + \Delta t \Phi\left(\boldsymbol{\nu}_{n+1}, \left(\boldsymbol{\nu}_{n+1} - \boldsymbol{\nu}_{n+1}\right)/\Delta t\right) \right\} dV + l\left(t_{n+1}, \boldsymbol{u}_{n+1}\right). \quad (4.70)$$

Within the present work, the minimization of (4.70) is performed by an approach consisting of two parts: the global level solution part and the material point solution part. The former calculates deformation and damage, whereas the latter evaluates the internal variables $\boldsymbol{\epsilon}_{\mathrm{p}}$ and $\boldsymbol{\xi}$ by using the predictor-corrector scheme. In the continuation, each solution part is explained separately. The indexes related to step $n+1$ are omitted in order to achieve a concise representation.

4.8.2 Global solution part

The definition of the global solution part (gl) starts with the reduced formulation of the Lagrangian by only including the reduced elastic energy and damage potential

$$\mathcal{L}^{\mathrm{gl}} = \int_\Omega \mathcal{L} dV = \int_\Omega \omega(d)\Psi_+^{\mathrm{el}}\left(\boldsymbol{\epsilon}^{\mathrm{e}}\right) + \Psi_-^{\mathrm{el}}\left(\boldsymbol{\epsilon}^{\mathrm{e}}\right) dV + \int_\Omega \Delta t \Phi^{\mathrm{d}}\left(d_n, \nabla d_n, d, \nabla d\right) dV + l(t, \boldsymbol{u}). \tag{4.71}$$

By using the expression for the crack surface density (4.1) and definition (4.5) the increment $\Delta\Phi^{\mathrm{d}}$ can be reconstructed as shown in Miehe et al. (4.2010a,b)

$$\Delta t \Phi^{\mathrm{d}}\left(d_n, \nabla d_n, d, \nabla d\right) = \frac{g_c}{2l}\left(d^2 - d_n^2\right) + \frac{g_c l}{2}\left(|\nabla d|^2 - |\nabla d_n|^2\right) + \frac{k_{\mathrm{p}}}{2\Delta t}\left\langle d - d_n\right\rangle_-^2. \tag{4.72}$$

The FE-implementation now requires the derivatives of the Lagrangian $\mathcal{L}$. The first derivatives are required in order to form the residual

$$\partial_{\boldsymbol{\epsilon}}\mathcal{L} = \omega\mathbb{C} : \boldsymbol{\epsilon}_+^{\mathrm{e}} + \mathbb{C} : \boldsymbol{\epsilon}_-^{\mathrm{e}}, \tag{4.73}$$

$$\partial_d\mathcal{L} = \omega'\Psi_+^{\mathrm{el}} + \frac{g_c}{l}d + \frac{k_{\mathrm{p}}}{\Delta t}\left\langle d - d_n\right\rangle_-, \quad \partial_{\nabla d}\mathcal{L} = g_c l \nabla d, \tag{4.74}$$

whereas the second derivatives are needed for the definition of the stiffness matrix

$$\partial^2_{\boldsymbol{\epsilon}\boldsymbol{\epsilon}}\mathcal{L} = \omega\mathbb{C} : \boldsymbol{I}_+^{\boldsymbol{\epsilon}^{\mathrm{e}}} + \mathbb{C} : \boldsymbol{I}_-^{\boldsymbol{\epsilon}^{\mathrm{e}}}, \quad \partial^2_{\boldsymbol{\epsilon}d}\mathcal{L} = \omega'\mathbb{C} : \boldsymbol{\epsilon}_+^{\mathrm{e}}, \tag{4.75}$$

$$\partial^2_{dd}\mathcal{L} = \omega''\Psi_+^{\mathrm{el}} + \frac{g_c}{l} + \frac{k_{\mathrm{p}}}{\Delta t}I^d, \quad \partial^2_{\nabla d \nabla d}\mathcal{L} = g_c l. \tag{4.76}$$

These relationships use the following indicator functions

$$\boldsymbol{I}_+^{\boldsymbol{\epsilon}^{\mathrm{e}}} = \frac{\partial \boldsymbol{\epsilon}_+^{\mathrm{e}}}{\partial \boldsymbol{\epsilon}^{\mathrm{e}}} = \sum_i I_{i+}^{\mathrm{e}} \boldsymbol{m}_i \otimes \boldsymbol{m}_i, \quad \boldsymbol{m}_i = \boldsymbol{n}_i \otimes \boldsymbol{n}_i, \tag{4.77}$$

$$\boldsymbol{I}_-^{\boldsymbol{\epsilon}^{\mathrm{e}}} = \frac{\partial \boldsymbol{\epsilon}_-^{\mathrm{e}}}{\partial \boldsymbol{\epsilon}^{\mathrm{e}}} = \sum_i \left(1 - I_{i+}^{\mathrm{e}}\right) \boldsymbol{m}_i \otimes \boldsymbol{m}_i, \tag{4.78}$$

$$I_{i+}^{\mathrm{e}} = \begin{cases} 1 & \text{if} \quad \boldsymbol{\epsilon}_i > 0, \\ 0 & \text{if} \quad \boldsymbol{\epsilon}_i \leq 0, \end{cases} \quad I^d = \begin{cases} 1 & \text{if} \quad d < d_n, \\ 0 & \text{if} \quad d \geq d_n. \end{cases} \tag{4.79}$$

The remaining part of the numerical procedure at this level encompasses the standard steps typical of an FE-model. To this end, the bilinear shape functions corresponding to a quadrilateral element and staggered solution scheme are applied in the present work. This approach staggers between the displacement and the phase-field and is

advantageous compared to the monolithic solution type due to its higher robustness. However, both approaches are well established nowadays as shown in works applying monolithic schemes (Miehe et al., [106]; Kuhn and Müller, [95]; Schlueter et al., [128]; Msekh et al., [110]) or using its counterpart (Miehe et al., [105]; Borden et al., [27]; Hofacker and Miehe, [74]). The standard Newton-Raphson procedure is applied for the solution of nonlinear systems of equations.

4.8.3 Material point solution part

The material point solution part evaluates internal variables $\boldsymbol{\epsilon}^{\mathrm{p}}$ and $\boldsymbol{\xi}$ by using a predictor-corrector scheme if damage and deformations $(d, \boldsymbol{u})$ as well as rate $\dot{\bar{\omega}} = \omega' \frac{d-d_n}{\Delta t}$ are known from the global level solution. The predictor step calculates the trial stress by assuming that plastic deformations do not change in comparison with the previous time step n

$$\boldsymbol{\sigma}^{\mathrm{tr}} = \omega(d)\mathbb{C} : (\boldsymbol{\epsilon} - \boldsymbol{\epsilon}_n^{\mathrm{p}})_+ + \mathbb{C} : (\boldsymbol{\epsilon} - \boldsymbol{\epsilon}_n^{\mathrm{p}})_- \,. \tag{4.80}$$

The trial stress is furthermore introduced in the yield locus function to check whether the prediction is true

$$\Phi^{\mathrm{c,tr}} = \left\| \bar{\boldsymbol{\sigma}}^{\mathrm{tr}} - \bar{\boldsymbol{\chi}}_n \right\| - \bar{\omega}\bar{\sigma}_{\mathrm{Y}}. \tag{4.81}$$

If the control value $\Phi^{\mathrm{c,tr}}$ is negative, the prediction (4.80) is correct and the plastic deformations do not evolve in the present step. Otherwise, a corrector step is needed to update the plastic deformations. The corrector step firstly calculates the plastic multiplier according to the scheme shown in Sect. 4.7. The initial value λ_0 is determined by solving the simplified problem (4.67)

$$\lambda_0 = \frac{(\bar{\boldsymbol{\sigma}}^{\mathrm{tr}} - \bar{\boldsymbol{\chi}}_n) : \left[\omega' \bar{\boldsymbol{\sigma}}_+^{\mathrm{tr}} + \dot{\bar{\omega}} c \boldsymbol{\xi}_n + \frac{c}{b} \bar{\boldsymbol{\chi}}_n\right]}{c\bar{\omega}\,(\bar{\boldsymbol{\sigma}}^{\mathrm{tr}} - \bar{\boldsymbol{\chi}}_n) : \bar{N}^{\mathrm{tr}}}, \tag{4.82}$$

whereas the later iterations follow the rule

$$\lambda_i = \frac{(\bar{\boldsymbol{\sigma}}^{\mathrm{tr}} - \bar{\boldsymbol{\chi}}_n) : \boldsymbol{R}}{c\bar{\omega}\,(\bar{\boldsymbol{\sigma}}^{\mathrm{tr}} - \bar{\boldsymbol{\chi}}_n) : \bar{N}^{\mathrm{tr}}}, \tag{4.83}$$

$$\boldsymbol{R} = \left[\omega' \boldsymbol{\sigma}_+^{\mathrm{tr}} + \omega\mathbb{C} : \left[\frac{(\boldsymbol{\epsilon} - \boldsymbol{\epsilon}_n)}{\Delta t} - \lambda_{i-1} \boldsymbol{N}^{\mathrm{tr}}\right]_+ + \mathbb{C} : \left[\frac{(\boldsymbol{\epsilon} - \boldsymbol{\epsilon}_n)}{\Delta t} - \lambda_{i-1} \boldsymbol{N}^{\mathrm{tr}}\right]_- + \dot{\bar{\omega}} c \boldsymbol{\xi}_n + \frac{c}{b} \bar{\boldsymbol{\chi}}_n\right]. \tag{4.84}$$

The previous expressions use the approximation $\dot{\boldsymbol{\epsilon}} = \frac{\boldsymbol{\epsilon} - \boldsymbol{\epsilon}_n}{\Delta t}$ and notation $\bar{\boldsymbol{N}}^{\mathrm{tr}} = \frac{(\bar{\boldsymbol{\sigma}}^{\mathrm{tr}} - \bar{\boldsymbol{\chi}}^{\mathrm{n}})}{||\bar{\boldsymbol{\sigma}}^{\mathrm{tr}} \bar{\boldsymbol{\chi}}^{\mathrm{n}}||}$. Note that index i is related to the iterative solution for λ_i, whereas index n denotes the time step. Quantities without any index are related to the step $n + 1$ or are constant.

Table 4.1: Elastic and plastic material parameters for CS and SS.

Parameter	Value CS	Value SS	Unit	Name
E	212910	197960	[MPa]	Young's modulus
ν	0.3	0.3	[-]	Poisson's ratio
σ_{Y}	451	552	[MPa]	yield stress
b	5	6	[Ns/mm^2]	pseudo-viscosity
c	30000	70000	[N/mm]	kinematic hardening parameter

Finally, the solution of the iterative procedure (4.83)-(84) is denoted $\lambda - \lambda_i$ and used to update plastic deformations $\boldsymbol{\epsilon}^{\mathrm{p}}$, driving forces $\boldsymbol{\chi}$ and stress response $\boldsymbol{\sigma}$

$$\dot{\boldsymbol{\epsilon}}_{\mathrm{p}} = \frac{\boldsymbol{\epsilon}^{\mathrm{p}} - \boldsymbol{\epsilon}^{\mathrm{p}}_n}{\Delta \mathrm{t}} = \lambda \bar{N}^{\mathrm{tr}} \quad \Rightarrow \quad \boldsymbol{\epsilon}^{\mathrm{p}} = \Delta t \lambda \bar{N}^{\mathrm{tr}} + \boldsymbol{\epsilon}^{\mathrm{p}}_n, \tag{4.85}$$

$$\dot{\boldsymbol{\xi}} = \frac{\boldsymbol{\xi} - \boldsymbol{\xi}_n}{\Delta t} = \frac{1}{b\bar{\omega}} \bar{\boldsymbol{\chi}}_n - \dot{\boldsymbol{\epsilon}}_{\mathrm{p}} \Rightarrow \quad \boldsymbol{\xi} = \frac{\Delta t}{b\bar{\omega}} \bar{\boldsymbol{\chi}}_n - \Delta t \lambda \bar{\boldsymbol{N}}^{\mathrm{tr}} + \boldsymbol{\xi}_n, \tag{4.86}$$

$$\begin{aligned} \dot{\boldsymbol{\chi}} = \dot{\bar{\boldsymbol{\chi}}} = \frac{\bar{\boldsymbol{\chi}} - \bar{\boldsymbol{\chi}}_n}{\Delta \mathrm{t}} &= -\dot{\bar{\omega}} c \boldsymbol{\xi}_n + c\bar{\omega} \dot{\boldsymbol{\epsilon}}_{\mathrm{p}} - \frac{c}{b} \boldsymbol{\chi}_n \\ \Rightarrow \quad \boldsymbol{\chi} = \bar{\boldsymbol{\chi}} &= -\Delta t \dot{\bar{\omega}} c \boldsymbol{\xi}_n + c\bar{\omega} \Delta t \lambda \bar{N}^{\mathrm{tr}} - \frac{c \Delta t}{b} \bar{\boldsymbol{\chi}}_n + \bar{\boldsymbol{\chi}}_n, \end{aligned} \tag{4.87}$$

$$\boldsymbol{\sigma} = \omega(d) \mathbb{C} : (\boldsymbol{\epsilon} - \boldsymbol{\epsilon}^{\mathrm{p}})_+ + \mathbb{C} : (\boldsymbol{\epsilon} - \boldsymbol{\epsilon}^{\mathrm{p}})_- \,. \tag{4.88}$$

4.9 Representative numerical examples

The model developed inherits the advantages of both methods that it incorporates. That makes its application field large, as demonstrated in the subsequent sections studying the behavior of the cold-formed carbon steel (CS) and of the cold-formed stainless steel (SS). Among others, selected numerical examples deal with the purely elasto-plastic material behavior (Sect. 4.9.1), with the simulation of crack propagation on a notched sample (Sect. 4.9.2) and with the study of the life time in the LCF-mode (Sect. 4.9.3).

4.9.1 Elasto-plastic behavior of the carbon steel and of the stainless steel

The first group of examples illustrating the application of the model studies a purely elasto-plastic material behavior under a cyclic load by neglecting the damage effects. To this end, simulations at a single material point are performed for parameter sets shown in Tab. 1. The prescribed strains gradually change from zero to 1 % and thereafter

decrease to -1 %. The cycle again closes at zero load level. Two cycles with identical load paths are carried out. Each cycle takes 2 s to complete, whereas a single time step is $\Delta t = 0.01$ s.

Simulations are carried out for two kinds of steel, namely for the cold-formed carbon steel (CS) and the cold-formed stainless steel (SS). The results are furthermore compared to the experimental findings by Nip et al. ([115]). This comparison is presented in Fig. 4.1 and approves an excellent agreement. The stainless steel hardens stronger than the carbon steel, such that parameter c is higher in this case. More details on the parameter identification in the context of the Armstrong-Frederick model are for example provided in Wolff et al. ([161]); Lubarda and Benson ([101]).

4.9.2 Crack propagation on a notched sample

The geometry of the sample for the second group of simulations is shown in Fig. 4.2. The chosen square plate has dimensions 1 mm × 1 mm and a thickness of 1 mm and represents a cutout of a 3D body with the large thickness, which substantiates the assumption of plane strains (Fig. 4.2a). The model does not include any material length scale, such that sample size and prescribed displacements can be scaled in a straightforward manner. The left edge of the sample is fixed in horizontal direction. The vertical displacement at the bottom left corner is additionally suppressed. Horizontal displacements $\bar{u}_x$ are prescribed at the right edge. The plate has a vertical initial crack from the middle of the bottom edge to the midpoint of the sample. It is discretized by a mesh with approximately 22500 quadrilateral elements such that a fine discretization is performed in the areas where crack propagation is expected (Fig. 4.2b). In this area, the effective element size h fulfills the condition $h \approx 0.001$ mm $< l/2$ and is significantly less than the minimum size required to achieve reasonable accuracy in the crack zone (Miehe et al., [106]). Here, l denotes the characteristic crack width typical of the phase field method. The section simulates the crack propagation on the notched example and investigates the influence of material parameters on this process. The carbon steel is assumed as the representative material this time. Apart from elastic and plastic material parameters (Tab. 1), simulations require damage parameters. The values chosen to this end are listed in Tab. 2. Here, the values proposed by Miehe et al. ([106]) are used for the critical energy g_c and characteristic crack width l. Constant k_p of the penalty function (Eq. (4.4)) is chosen to be 1×10^8, which is sufficiently large to suppress the negative damage rate. Constant k_d has the value of 1×10^{-8} and prevents the energy from becoming identical to zero in the case of full material damage. In all examples of this group, the load increment and damage parameters g_c and l are assumed such that the crack formation and propagation can be simulated within a fairly small number of time steps in order to reduce the computational effort and to provide a qualitative analysis of relevant phenomena according to the results from Miehe et al. ([106]). The behavior of the notched sample (Fig. 4.2) is investigated for three load constellations: uniformly increasing tension, cyclic load with a tension and

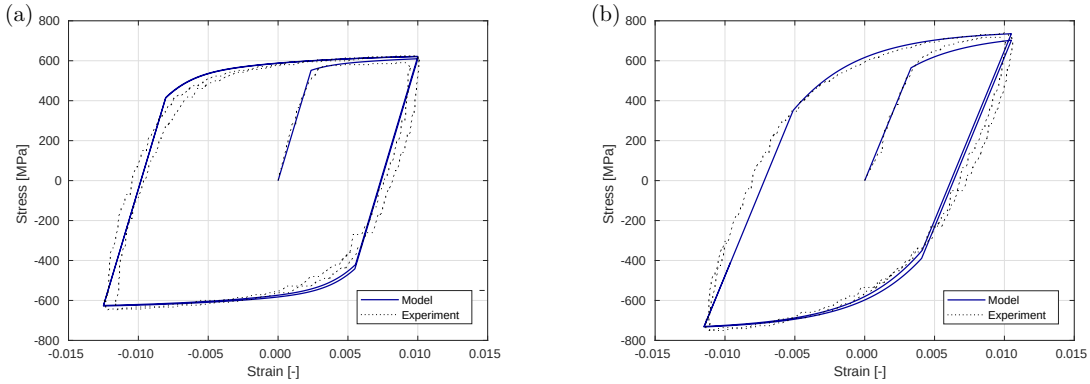

Figure 4.1: Comparison of experimental and numerical results at a material point. (a) Stress-strain hysteresis for carbon steel (CS). (b) Stress-strain hysteresis for stainless steel (SS). Plotted are the 11-components of the stress tensor and the strain tensor. Experimental results are taken from Nip et al. (4.2010).

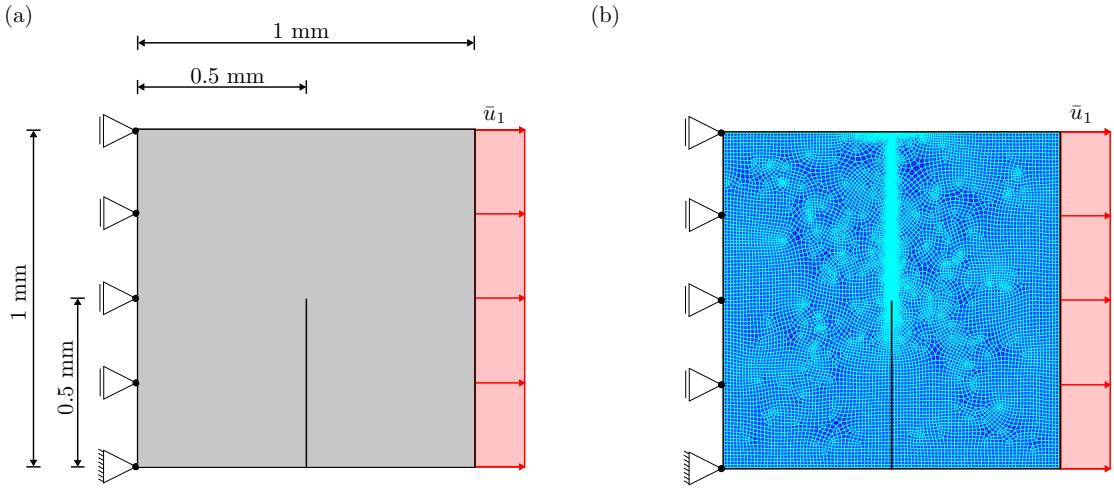

Figure 4.2: (a) Geometry of the notched plate with prescribed horizontal displacements $\bar{u}_x$. (b) Discretization of the plate with approximately 22500 elements.

compression phase and cyclic load with an increasing amplitude in the tension regime. In the first case, the prescribed displacement linearly increases up to the maximum value of $\bar{u}_x = 0.005$ mm. The constant time increment is $\Delta t = 0.005$ s and the total loading time amounts to 1 s. The results at a quadrature point of an element directly located at the end of the initial crack are monitored for the illustration in Fig. 4.3. This figure shows the change of damage and stress state during tension tests for different pairs of parameters b and c. Here, rapidly hardening materials with a high hardening modulus c lead to a faster increase of damage, whereas the higher pseudo-viscosity slows down the damage evolution and postpones softening. Damage increases from moderate values to the maximum, such that the material loses its strength and stress falls to the nearly zero

Table 4.2: Material parameters of the damage model.

Parameter	Value	Unit	Name
g_c	0.27	[N/mm^2]	critical energy release rate
l	0.0375	[mm]	characteristic crack width
k_p	1×10^8	[-]	penalty constant
k_d	1×10^{-8}	[-]	numerical constant

value. The stress drop takes place in approximately 0.05 s. Simulations are performed for different time increments in order to check the accuracy of the solution. For a time increment $\Delta t = 0.005$ s and less, identical results are achieved. The same setup (Fig. 4.2)

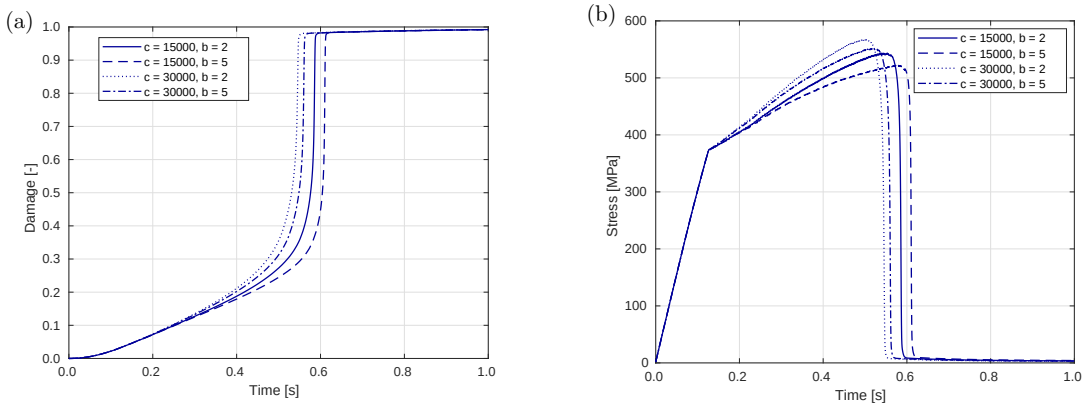

Figure 4.3: Results of tensile tests for different parameter pairs b and c. Prescribed displacements uniformly change up to the value of 0.005 mm. (a) Applied load as a function of time and damage evolution over time. (b) The 11-component of the stress tensor over the time. Hardening modulus c is expressed in N/mm and pseudo-viscosity b is expressed in Ns/mm^2.

is used to investigate influences of a cyclic load as shown in Fig. 4.4. Here, two load cycles are performed with the total duration of 4 s. The time increment is $\Delta t = 0.005$ s. The horizontal displacement $\bar{u}_x$ changes in the range [0.0025 mm, -0.0025 mm], implying that a cycle includes both: the tension and the compression mode. The load amplitudes are constant in both cycles. Figure 4.4a shows the load path and the damage evolution. The damage variable evolves during the tension phase, whereas the unloading and the compression mode do not affect it. This behavior goes back to the split of the energy into a tension and a compression part (Eq. (4.6)). Even though the same displacement is applied in every cycle, an increase in damage is observed during each loading cycle. Figure 4.4b shows the strong influence of damage on the corresponding stress-strain hysteresis. Here, the Baushinger effect is hardly noticeable, although a displacement controlled test with constant amplitudes is simulated. Fig. 4.4b depicts the ratcheting rather than the Bauschinger effect. The last load constellation applied to the setup from Fig. 4.2 deals with the cyclic load in the tension regime with the increasing amplitude (Fig. 4.5). The amplitude increment amounts to 2×10^{-4} mm per cycle. Time increment

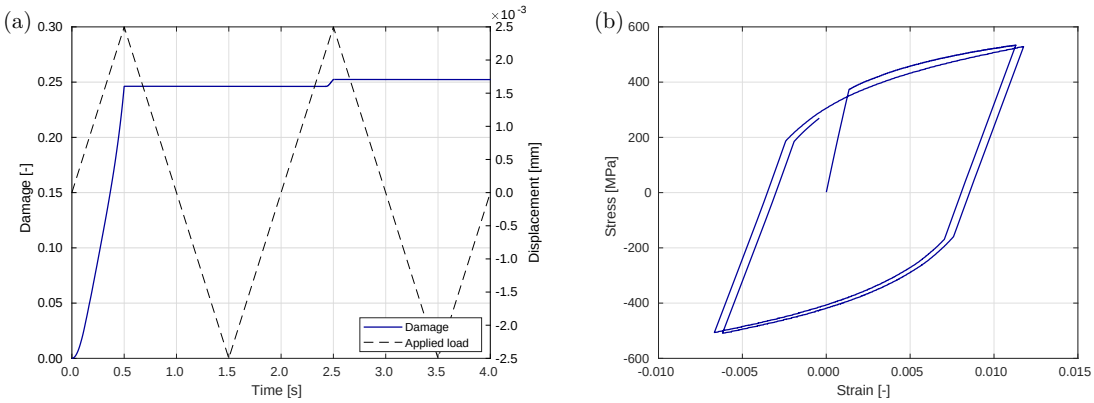

Figure 4.4: (a) Applied load as a function of time and the damage evolution for two load cycles. (b) The 11-component of the stress tensor over the 11-component of the strain tensor.

$\Delta t = 0.005$ s is assumed. Three damage contour plots are chosen presenting states of the crack during propagation for parameters $c = 15000$ N/mm (Fig. 4.6a) and $c = 30000$ N/mm (Fig. 4.6b). The first snapshot indicates the state at which damage variable d reaches a value of one at the already existing crack tip. The second plot is taken when the crack has propagated roughly half the way through the plate, and the last plot is taken when the plate is fully torn in half. For the first parameter value ($c = 15000$ N/mm), the crack opening starts in the 19th load cycle and is fully propagated throughout the plate in the 23rd load cycle (Fig. 4.6a). For the second parameter value ($c = 30000$ N/mm), damage evolves earlier and faster: here, the complete crack propagation takes place within three load cycles (Fig. 4.6b).

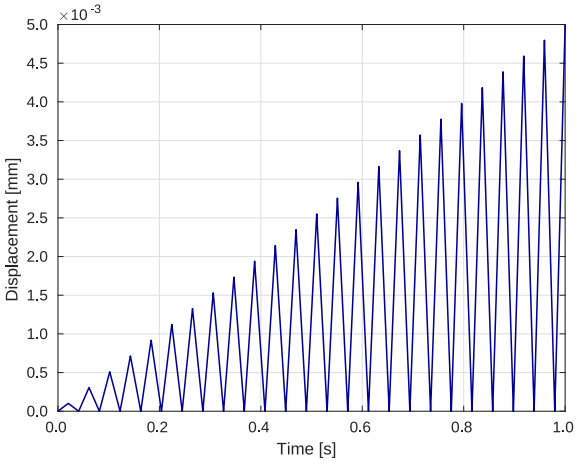

Figure 4.5: Increasing load amplitudes as a function of time.

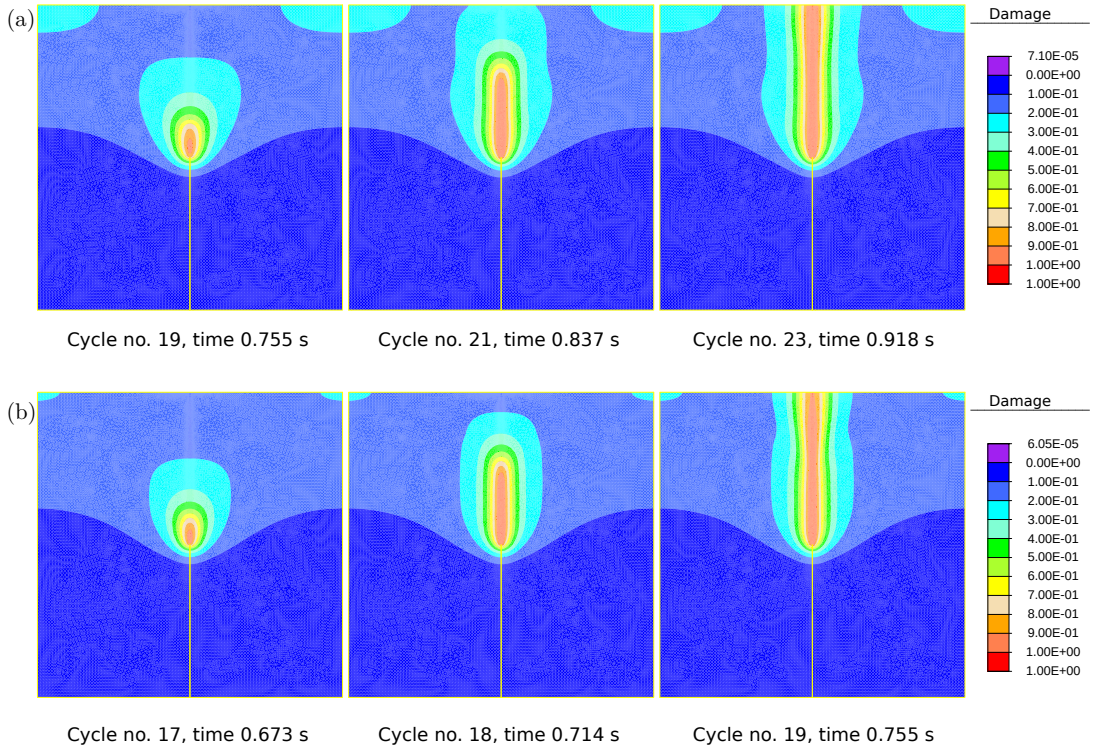

Figure 4.6: (a) Crack propagation takes place in five cycles ($c = 15000$ N/mm, $b = 2$ Ns/mm^2). (b) Crack propagation takes place in three cycles ($c = 30000$ N/mm, $b = 2$ Ns/mm^2).

4.9.3 Life time of the cold steel and of the stainless steel in the LCF-mode

Amongst others, the model proposed enables the estimation of the life time in the LCF-mode. To this end, the number of cycles up to the total failure is evaluated dependent on the amplitude of the cyclic load applied. The latter is kept constant during the test. The material failure is caused by the material defects such as production process induced pores at a small length scale. In most cases, surface porosity is the critical factor for the fatigue phenomenon. However, the present paper assumes that different methods of the surface treatment can resolve this type of imperfection and that a defect in the bulk of material causes the crack initiation.

This part of the analysis assumes the sample geometry (Fig. 4.7a) proposed by Nip et al. ([115]). The horizontal displacements are constrained at the left boundary and the cyclic horizontal displacements are prescribed at the right boundary. In addition, the vertical displacement at the lower left corner is constrained to suppress the rigid body motion. For the chosen boundary condition, the largest deformations are expected in the center of the sample, which is discretized by a fine mesh. The effective element size in this area is $h \approx 0.25$ mm, such that the crack width length $l = 0.6$ is chosen. The critical energy is set to $g_c = 100$ N/mm^2 which corresponds to a ductile material

behavior, whereas the remaining material parameters are kept as in Sects. 9.1 and 9.2. Simulations are additionally performed for higher values of the hardening modulus c in order to study the influence of this parameter. A defect is created in an element in the center of the specimen, which initiates crack growth in the otherwise homogeneous material. In this element, the values of the Young's modulus and the yield stress are set to 75% of the actual material parameters.

The very first step of the analysis applies a strain of 3%. The assumed time increment is $\Delta t = 4.28 \times 10^{-4}$ s and 2000 time steps simulate a single cycle. As expected, a vertical crack propagates through the middle of the sample, which is shown in Fig. 4.7b. Here, an early stage of the crack is already noticeable in the 47th cycle, whereas the total failure occurs in cycle number 96. Figure 4.7b corresponds to the carbon steel with the hardening modulus $c = 30000$ N/mm. Furthermore, the tests are repeated by increasing

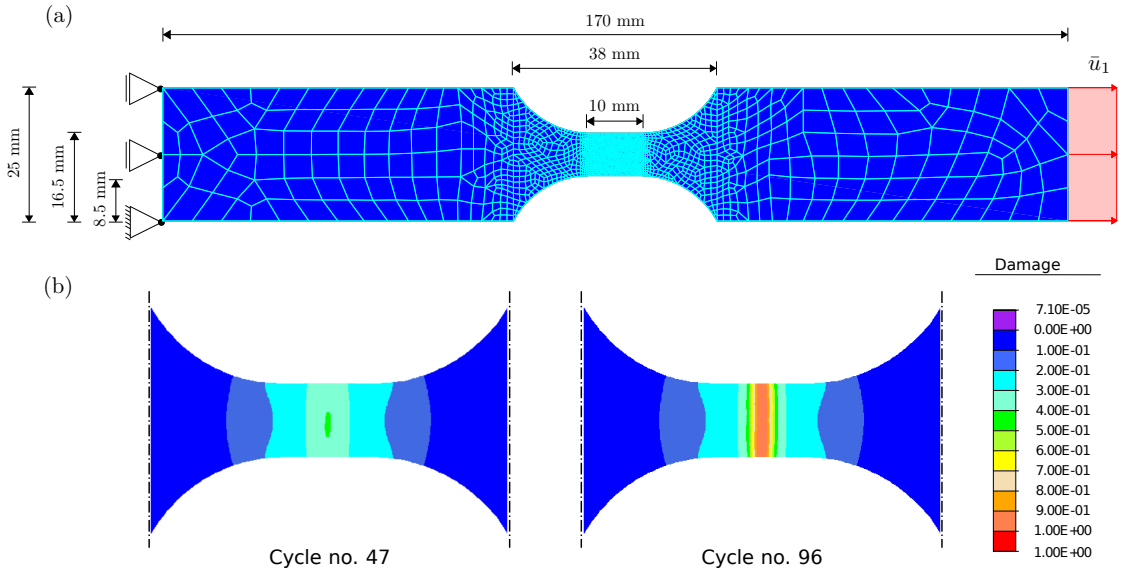

Figure 4.7: (a) Geometry of the simulated sample and prescribed boundary conditions. (b) Different stages of the crack propagation under the cyclic load. Simulations are performed for the carbon steel with the hardening modulus $c = 30000$ N/mm.

the load amplitude to the strain of 4%, 5%, 6% and 7%. The same setup (Fig. 4.7a) is applied to this end. The number of time steps within a cycle is kept constant (4.2000), however, the time increment varies in the range from $\Delta t = 4.28 \times 10^{-4}$ s to $\Delta t = 1 \times 10^{-3}$ s. Accordingly, the duration of one cycle takes the values between 0.856 s and 2 s.

The results of simulations together with the experimental results by Nip et al. ([115]) are presented in Fig. 4.8. First, the behavior of carbon steel is studied and compared to the Coffin-Manson curve relating the applied strains to the number of cycles, both in logarithmic scales (Fig. 4.8a). Numerical results show an excellent agreement with the experimental findings, in particular for higher strains. The dependence between the applied strains and the number of cycles is linear, however, the number of cycles is min-

imally overestimated. The discrepancy between the experimental and numerical results slightly increases with the decreasing strains. The same kind of simulations is repeated for a higher value of the hardening parameter, which leads to a significant decrease of the number of cycles up to the failure. This tendency goes back to the fact that a higher hardening modulus is related to the faster damage evolution and consequently causes a reduction of the number of cycles. Simulations for a higher hardening modulus approves the linear dependency between data, however, they indicate that a change of the strain amplitude has a higher influence on the change of number of cycles in this case.

The observations mentioned previously have also been approved by repeating the same kind of tests for the stainless steel as shown in Fig. 4.8b. Here, the Manson-Coffin curve has a slightly higher slope, but numerical results compared to the experimental ones show the same tendencies as for the carbon steel.

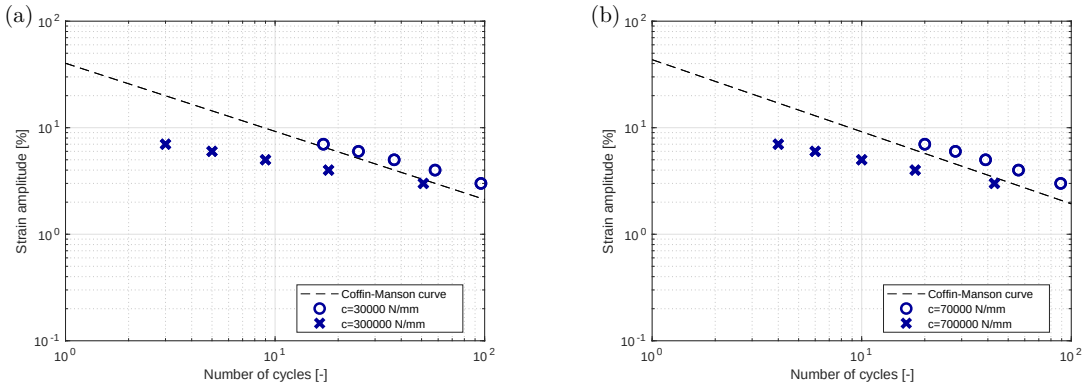

Figure 4.8: Comparison of the experimental Coffin-Manson curve (Nip et al., 2010) to the numerical results. (a) Results for carbon steel with two different hardening parameters $c = 30000$ N/mm and $c = 300000$ N/mm. (b) Results for the stainless steel with the hardening parameters $c = 70000$ N/mm and $c = 700000$ N/mm.

4.10 Conclusions and outlook

The present work couples the phase field method of fracture to the Armstrong- Frederick model of plasticity with the kinematic hardening. The chosen concept inherits the advantages of both techniques and is aimed at the study of LCF effects in ductile materials. However, the numerical implementation of this promising approach faces several challenges, such as the definition of a unique framework for both setups, the derivation of coupled evolution equations, the distinction between tension and compression mode and the development of a computationally efficient algorithm. The basis for the phase field fracture model are the Griffith's theory and the dissipation potential relying on the assumption of a crack surface function. The derivation of evolution equations uses the minimum principle of the dissipation potential, which requires to express the dissipation potential of the classical Armstrong-Frederick model in terms of the internal

variable rates by using the Legendre transformation. The model developed also takes into account that the unloading and the compression mode have no effect on the damage evolution. The approach is eventually implemented in the FE-program FEAP where the displacements and damage are calculated at the global level by using a staggered scheme, whereas inelastic internal variables are updated locally, at each Gauss point.

The application of the model is illustrated by three groups of examples related to the cold-formed carbon steel and the cold-formed stainless steel. The first group of tests investigates the purely elasto-plastic material behavior without the influence of damage and focuses on the numerical reconstruction of the stress-strain hysteresis due to a cyclic load. The second group of tests simulates the crack propagation on a notched sample and particularly analyses the influence of plastic parameters on the damage evolution. The simulations show that the rapidly hardening materials are prone to a faster damage evolution. The ability of the model to constrain the damage evolution in the unloading and compression stages of a loading cycle is demonstrated as well. The last group of tests studies the life time of the carbon steel in the LCF-mode and compares the numerical results to the experimental findings by Nip et al. ([115]). The results show an excellent qualitative and quantitative agreement, and the linear dependency between the data in a logarithmic scale is approved.

The model proposed is a promising tool with regard to the simulation of fatigue effects, giving rise to many new issues. Among others, it can be extended to capture "hidden" aspects of the fatigue process such as the microcrack initiation based on the theory of persistent slip bands and the microcrack propagation along the crystallographic planes. Moreover, the additional effects typical of high and very high cycle fatigue, as well as the threshold for the damage initiation have to be incorporated. A comprehensive validation of the model with respect to the experimental results as well as its application and calibration for further materials are also envisaged.

A Legendre transformation

The formulation of the MDP in terms of rates of internal variables is based on Legendre transformation:

$$\Phi^{\mathrm{AF}}(\boldsymbol{\nu}, \dot{\boldsymbol{\nu}}) = \max_{\boldsymbol{q}} \left\{ \mathcal{L}^{\mathrm{LT}} = \boldsymbol{q} : \dot{\boldsymbol{\nu}} - \Phi^{\mathrm{AF}^*}(\boldsymbol{\nu}, \boldsymbol{q}) \right\}, \tag{4.89}$$

$$\mathcal{L}^{\mathrm{LT}} = \boldsymbol{\sigma} : \dot{\boldsymbol{\epsilon}}^{\mathrm{p}} + \boldsymbol{\chi} : \dot{\boldsymbol{\xi}} - a\|\bar{\boldsymbol{\sigma}} - \bar{\boldsymbol{\chi}}\| - \frac{1}{2b}\|\bar{\boldsymbol{\chi}}\|^2. \tag{4.90}$$

The corresponding stationary conditions have already been derived in Sect.5 (Eqs.(30)b and(31)b)

$$\bar{\boldsymbol{\sigma}} = \bar{\sigma}_{\mathrm{Y}} \frac{\dot{\boldsymbol{\epsilon}}^{\mathrm{p}}}{\|\dot{\boldsymbol{\epsilon}}^{\mathrm{p}}\|} + b\dot{\boldsymbol{\xi}} + b\dot{\boldsymbol{\epsilon}}^{\mathrm{p}}, \quad \bar{\boldsymbol{\chi}} = b\dot{\boldsymbol{\xi}} + b\dot{\boldsymbol{\epsilon}}^{\mathrm{p}}. \tag{4.91}$$

Their implementation in (4.90) now yields

$$\begin{aligned}
\mathcal{L}^{\mathrm{LT}} &= \boldsymbol{\sigma} : \dot{\boldsymbol{\epsilon}}^{\mathrm{p}} + \boldsymbol{\chi} : \dot{\boldsymbol{\xi}} - a\|\bar{\boldsymbol{\sigma}} - \bar{\boldsymbol{\chi}}\| - \frac{1}{2b}\|\bar{\boldsymbol{\chi}}\|^2 \\
&= \bar{\sigma}_{\mathrm{Y}} \frac{\dot{\boldsymbol{\epsilon}}^{\mathrm{p}}}{\|\dot{\boldsymbol{\epsilon}}^{\mathrm{p}}\|} : \dot{\boldsymbol{\epsilon}}^{\mathrm{p}} + b\dot{\boldsymbol{\xi}} : \dot{\boldsymbol{\epsilon}}^{\mathrm{p}} + b\dot{\boldsymbol{\epsilon}}^{\mathrm{p}} : \dot{\boldsymbol{\epsilon}}^{\mathrm{p}} + b\dot{\boldsymbol{\xi}} : \dot{\boldsymbol{\xi}} + b\dot{\boldsymbol{\epsilon}}^{\mathrm{p}} : \dot{\boldsymbol{\xi}} \\
&\qquad - a\left\|\bar{\sigma}_{\mathrm{Y}} \frac{\dot{\boldsymbol{\epsilon}}^{\mathrm{p}}}{\|\dot{\boldsymbol{\epsilon}}^{\mathrm{p}}\|}\right\| - \frac{1}{2b}\left[b^2\|\dot{\boldsymbol{\xi}}\|^2 + 2b^2\dot{\boldsymbol{\xi}} : \dot{\boldsymbol{\epsilon}}^{\mathrm{p}} + b^2\left\|\dot{\boldsymbol{\epsilon}}^{\mathrm{p}}\right\|^2\right] \\
&= \bar{\sigma}_{\mathrm{Y}}\left\|\dot{\boldsymbol{\epsilon}}^{\mathrm{p}}\right\| + b\dot{\boldsymbol{\xi}} : \dot{\boldsymbol{\epsilon}}^{\mathrm{p}} + b\left\|\dot{\boldsymbol{\epsilon}}^{\mathrm{p}}\right\|^2 + b\|\dot{\boldsymbol{\xi}}\|^2 + b\dot{\boldsymbol{\xi}} : \dot{\boldsymbol{\epsilon}}^{\mathrm{p}} - a\bar{\sigma}_{\mathrm{Y}} - \frac{b}{2}\|\dot{\boldsymbol{\xi}}\|^2 - b\dot{\boldsymbol{\xi}} : \dot{\boldsymbol{\epsilon}}^{\mathrm{p}} - \frac{b}{2}\left\|\dot{\boldsymbol{\epsilon}}^{\mathrm{p}}\right\|^2 \\
&= \bar{\sigma}_{\mathrm{Y}}\left\|\dot{\boldsymbol{\epsilon}}^{\mathrm{p}}\right\| + \frac{b}{2}\left\|\dot{\boldsymbol{\epsilon}}^{\mathrm{p}}\right\|^2 + \frac{b}{2}\|\dot{\boldsymbol{\xi}}\|^2 + b\dot{\boldsymbol{\epsilon}}^{\mathrm{p}} : \dot{\boldsymbol{\xi}} - a\bar{\sigma}_{\mathrm{Y}}.
\end{aligned} \tag{4.92}$$

The last term is a constant and thus can be neglected, since the evolution equations are obtained by its minimization of the potential. Accordingly, the sought potential turns into

$$\Phi^{\mathrm{AF}}(\boldsymbol{\nu}, \dot{\boldsymbol{\nu}}) = \bar{\sigma}_{\mathrm{Y}}\left\|\dot{\boldsymbol{\epsilon}}^{\mathrm{P}}\right\| + \frac{b}{2}\left\|\dot{\boldsymbol{\epsilon}}^{\mathrm{P}}\right\|^2 + \frac{b}{2}\|\dot{\boldsymbol{\xi}}\|^2 + b\dot{\boldsymbol{\epsilon}}^{\mathrm{p}} : \dot{\boldsymbol{\xi}}. \tag{4.93}$$

B Evolution equations of the coupled problem

The potential of the coupled problem has the form

$$\mathcal{L}^{\mathrm{MDP}} = \dot{\Psi}^{\mathrm{c}} + \Phi^{\mathrm{c}} = \dot{\Psi}^{\mathrm{c}} + \Phi^{\mathrm{d}} + \bar{\omega}\Phi^{\mathrm{AF}}, \tag{4.94}$$

where $\dot{\Psi}^{c}$ is defined in Eq. (4.48), Φ^{d} is defined by Eq. (4.5) and Φ^{AF} by Eq. (4.33). Driving forces corresponding to $\boldsymbol{\epsilon}^{\mathrm{p}}$ and $\boldsymbol{\xi}$ are then calculated as following derivatives

$$\boldsymbol{q}_{\boldsymbol{\epsilon}^{\mathrm{p}}} = \bar{\boldsymbol{\sigma}} = \frac{\partial \Phi^{\mathrm{c}}}{\partial \dot{\boldsymbol{\epsilon}}^{\mathrm{P}}} = \bar{\omega}\left[\bar{\sigma}_{\mathrm{Y}} \frac{\dot{\boldsymbol{\epsilon}}^{\mathrm{p}}}{\left\|\dot{\boldsymbol{\epsilon}}^{\mathrm{P}}\right\|} + b\dot{\boldsymbol{\epsilon}}^{\mathrm{p}} + b\dot{\boldsymbol{\xi}}\right], \tag{4.95}$$

$$\boldsymbol{q}_{\boldsymbol{\xi}} = \bar{\boldsymbol{\chi}} = \frac{\partial \Phi^{\mathrm{c}}}{\partial \dot{\boldsymbol{\xi}}} = \bar{\omega}\left[b\dot{\boldsymbol{\xi}} + b\dot{\boldsymbol{\epsilon}}^{\mathrm{P}}\right], \tag{4.96}$$

such that a transformation of the system (4.95) and (4.96) yields the evolution equations

$$\dot{\boldsymbol{\epsilon}}^{\mathrm{p}} = \lambda \frac{\bar{\boldsymbol{\sigma}} - \bar{\boldsymbol{\chi}}}{\|\bar{\boldsymbol{\sigma}} - \bar{\boldsymbol{\chi}}\|}, \quad \dot{\boldsymbol{\xi}} = -\dot{\boldsymbol{\epsilon}}^{\mathrm{p}} + \frac{1}{\bar{\omega}b}\bar{\boldsymbol{\chi}}, \tag{4.97}$$

whereas the insertion of (4.96) into (4.95) provides the yield locus equation

$$\bar{\boldsymbol{\sigma}} = \bar{\omega}\bar{\sigma}_{\mathrm{Y}}\frac{\dot{\boldsymbol{\epsilon}}^{\mathrm{p}}}{\|\dot{\boldsymbol{\epsilon}}^{\mathrm{p}}\|} + \boldsymbol{\chi} \quad \Rightarrow \quad \bar{\boldsymbol{\sigma}} - \bar{\boldsymbol{\chi}} = \bar{\omega}\bar{\sigma}_{\mathrm{Y}}\frac{\dot{\boldsymbol{\epsilon}}^{\mathrm{p}}}{\left\|\dot{\boldsymbol{\epsilon}}^{\mathrm{P}}\right\|} \quad \Rightarrow \quad \|\bar{\boldsymbol{\sigma}} - \bar{\boldsymbol{\chi}}\| = \bar{\omega}\bar{\sigma}_{\mathrm{Y}}. \tag{4.98}$$

Finally, constitutive law (4.51) is used to derive the evolution equation for the back stress:

$$\dot{\boldsymbol{\chi}} = -\dot{\bar{\omega}}c\boldsymbol{\xi} - \bar{\omega}c\dot{\boldsymbol{\xi}} = -\dot{\bar{\omega}}c\boldsymbol{\xi} + c\bar{\omega}\left(\dot{\boldsymbol{\epsilon}}^{\mathrm{p}} - \frac{1}{b\bar{\omega}}\bar{\boldsymbol{\chi}}\right). \tag{4.99}$$

5 Conclusions & Outlook

Interfaces are omnipresent in every aspect of our life, even in areas we are not particularly aware of. Besides their abundance, each interface comes with unique characteristics and is suited for the specific task it fulfills. They are present on all scales and contribute significantly to our understanding of the involved processes. In the scope of this work, three specific interfaces have been analyzed in detail, namely, the viral uptake into a cell via receptor driven endocytosis, the sintering of hollow spheres and the fatigue behavior under cyclic loading. Three different modeling approaches were chosen, based on the specific challenges and selected aspects of interest for the interfaces at hand.

Receptor driven endocytosis emphasizes that interfaces cannot only occur in the nano meter regime, but also represent a primary mechanic characterizing the viral uptake. Modeling the process aids in identifying and adapting design parameters, in order to archive a greater control on the uptake. The process has been modeled by using the finite difference method. The established framework provides an intuitive way to model the discontinuous distribution of receptors on the free surface of the cell and the contact area with the virus. It is possible to obtain information on the progress of the uptake and the geometric evolution of the cell surface without the need to create a geometric model.

Sintering of hollow spheres has been chosen as the second example, highlighting its application to artificially created interfaces. Its modeling provides valuable insight into preliminary design choices affecting the final properties of the material. In the context of this example, a shell element has been implemented into an IGA framework. Even though IGA is a relatively new approach, its ability to model complex geometries and bridge the gap between CAD and FEA has already led to remarkable results. Here, the focus was set on the fundamental mechanics, creating a base framework. Thus, the configuration was kept to two bodies. However, the framework already establishes a solid foundation to various extensions such as multiple bodies. In addition, the implemented shell element, covering thermo-mechanical effects, shows great potential to adapt, extend and vary the underlying material model.

Coupling the phase field approach, describing the material damage, to the Armstrong-Frederick model provides a thermodynamically consistent framework for the underlying formulation. The Legendre transformation has been used to formulate the model in terms of the rates of internal variables and a load-dependent evolution for low cycle

fatigue. They are designed specifically to recapture the stress-strain hysteresis, isolate the influence of the plastic parameters and were able to be compared to experimental data, showing excellent qualitative and quantitative agreement.

Future developments can greatly improve the work presented here. Each framework provides a strong base for further applications.

Endocytosis presents great potential to be extended regarding geometric aspects, such as different virus shapes. Extending the formulation to a fully three dimensional framework would allow the incorporation of arbitrary virus shapes. Furthermore, the deformation of the cell surface that is not in contact to the virus is of great interest. To this end, considering additional numerical frameworks, such as the IGA, could be a suitable approach to the modeling of organic shapes created in the endocytosis process. The general formulation also provides an interface to incorporate additional mechanisms regarding the movement of receptors on the cell surface, for example by considering different types of receptors.

The established IGA framework in the second example presents a base framework which still offers a great potential for numerical optimization and design parameters to be investigated. This is already highlighted by the initial meshing of the model. Being able to tune the coordinates of control points and their respective weights, various configurations can be applied to a given geometry, without proper understanding of the impact on the numerical performance. Various refinement strategies, such as h-refinement, subdividing the mesh into finer elements or p-refinement, increasing the polynomial degree of basis functions, are already well established but represent only a small subset of available methods. The examples presented were chosen in a way to exploit specific symmetry characteristics. Here, different approaches can be considered to extend the model for multiple bodies with irregular configurations.

The coupled model for low cycle fatigue also has great potential for further development. The formulation presented covers a specific set of mechanisms involved in the fatigue process. In addition to low cycle fatigue, the effects of high and very high cycle fatigue are of interest, where plasticity no longer plays a significant role.

Bibliography

[1] A. Abdollahi and I. Arias. Phase-field modeling of crack propagation in piezoelectric and ferroelectric materials with different electromechanical crack conditions. *Journal of the Mechanics and Physics of Solids*, 60(12):2100–2126, 2012.

[2] A. W. Adamson, A. P. Gast, et al. *Physical chemistry of surfaces*, volume 150. Interscience publishers New York, 1967.

[3] R. Alessi, J.-J. Marigo, and S. Vidoli. Gradient damage models coupled with plasticity and nucleation of cohesive cracks. *Archive for Rational Mechanics and Analysis*, 214:575–615, 2014.

[4] S. M. Allen and J. W. Cahn. A microscopic theory for antiphase boundary motion and its application to antiphase domain coarsening. *Acta metallurgica*, 27(6): 1085–1095, 1979.

[5] H. Altenbach, N. Chinchaladze, R. Kienzler, and W. H. Müller. *Analysis of Shells, Plates and Beams*. Springer, 2020.

[6] J. Alvarez, H. Snijder, T. Vaneker, H. Cheng, A. Thornton, S. Luding, and T. Weinhart. Visco-elastic sintering kinetics in virgin and aged polymer powders. *Powder Technology*, 397:117000, 2022.

[7] M. Ambati, T. Gerasimov, and L. De Lorenzis. Phase-field modeling of ductile fracture. *Computational Mechanics*, 55:1017–1040, 2015.

[8] M. Ambati, R. Kruse, and L. De Lorenzis. A phase-field model for ductile fracture at finite strains and its experimental verification. *Computational Mechanics*, 57: 149–167, 2016.

[9] L. Ambrosio. On the approximation of free discontinuity problems. *Boll. Un. Mat. Ital., B*, (7):105–123, 1992.

[10] L. Ambrosio and V. M. Tortorelli. Approximation of functional depending on jumps by elliptic functional via t-convergence. *Communications on Pure and Applied Mathematics*, 43(8):999–1036, 1990.

[11] O. Andersen, U. Waag, L. Schneider, G. Stephani, and B. Kieback. Novel metallic hollow sphere structures. *Advanced Engineering Materials*, 2(4):192–195, 2000.

[12] P. J. Armstrong, C. O. Frederick, et al. *A mathematical representation of the multiaxial Bauschinger effect*, volume 731. Berkeley Nuclear Laboratories Berkeley, CA, 1966.

[13] M. Arroyo and A. DeSimone. Relaxation dynamics of fluid membranes. *Phys. Rev. E*, 79(3):031915, 2009.

[14] M. Ashby. A first report on sintering diagrams. *Acta Metallurgica*, 22(3):275–289, 1974.

[15] S. Aygün and S. Klinge. Continuum mechanical modeling of strain-induced crystallization in polymers. *International Journal of Solids and Structures*, 196:129–139, 2020.

[16] S. Aygün, T. Wiegold, and S. Klinge. Coupling of the phase field approach to the armstrong-frederick model for the simulation of ductile damage under cyclic load. *International Journal of Plasticity*, 143:103021, 2021.

[17] J. Balaji and T. A. Ryan. Single-vesicle imaging reveals that synaptic vesicle exocytosis and endocytosis are coupled by a single stochastic mode. *Proceedings of the National Academy of Sciences*, 104(51):20576–20581, 2007.

[18] S. Bari and T. Hassan. Kinematic hardening rules in uncoupled modeling for multiaxial ratcheting simulation. *International Journal of Plasticity*, 17(7):885–905, 2001.

[19] E. Barrow, A. V. Nicola, and J. Liu. Multiscale perspectives of virus entry via endocytosis. *Virology journal*, 10(1):177, 2013.

[20] A. Bartels, P. Kurzeja, and J. Mosler. Cahn-hilliard phase field theory coupled to mechanics: Fundamentals, numerical implementation and application to topology optimization. *Computer Methods in Applied Mechanics and Engineering*, 383: 113918, 2021.

[21] A. Bartezzaghi, L. Dede, and A. Quarteroni. Isogeometric analysis of high order partial differential equations on surfaces. *Computer Methods in Applied Mechanics and Engineering*, 295:446–469, 2015.

[22] G. I. Bell. Models for the specific adhesion of cells to cells. *Science*, 200(4342): 618–627, 1978.

[23] T. Belytschko, W. K. Liu, B. Moran, and K. Elkhodary. *Nonlinear finite elements for continua and structures*. John Wiley & Sons, 2014.

[24] D. R. Beniac, A. Andonov, E. Grudeski, and T. F. Booth. Architecture of the sars coronavirus prefusion spike. *Nature structural & molecular biology*, 13(8):751–752, 2006.

[25] R. Berthelsen, R. Denzer, P. Oppermann, and A. Menzel. Computational homogenisation for thermoviscoplasticity: application to thermally sprayed coatings. *Computational Mechanics*, 60:739–766, 2017.

[26] A. Bertram. *Compendium on gradient materials*. 2023. URL `https://link.springer.com/book/10.1007/978-3-031-04500-4`.

[27] M. J. Borden, C. V. Verhoosel, M. A. Scott, T. J. Hughes, and C. M. Landis. A phase-field description of dynamic brittle fracture. *Computer Methods in Applied Mechanics and Engineering*, 217:77–95, 2012.

[28] M. J. Borden, T. J. Hughes, C. M. Landis, A. Anvari, and I. J. Lee. A phase-field formulation for fracture in ductile materials: Finite deformation balance law derivation, plastic degradation, and stress triaxiality effects. *Computer Methods in Applied Mechanics and Engineering*, 312:130–166, 2016.

[29] B. Bourdin and A. Chambolle. Implementation of an adaptive finite-element approximation of the mumford-shah functional. *Numerische Mathematik*, 85:609–646, 2000.

[30] B. Bourdin, G. A. Francfort, and J.-J. Marigo. Numerical experiments in revisited brittle fracture. *Journal of the Mechanics and Physics of Solids*, 48(4):797–826, 2000.

[31] B. Bourdin, G. A. Francfort, and J.-J. Marigo. The variational approach to fracture. *Journal of elasticity*, 91:5–148, 2008.

[32] B. Bourdin, C. Chukwudozie, and K. Yoshioka. A variational approach to the numerical simulation of hydraulic fracturing. In *SPE Annual Technical Conference and Exhibition?*, pages SPE–159154. SPE, 2012.

[33] B. Bourdin, J.-J. Marigo, C. Maurini, and P. Sicsic. Morphogenesis and propagation of complex cracks induced by thermal shocks. *Physical review letters*, 112(1): 014301, 2014.

[34] B. Brandenburg and X. Zhuang. Virus trafficking-learning from single-virus tracking. *Nature Reviews Microbiology*, 5(3):197–208, 2007.

[35] H.-J. Butt, K. Graf, and M. Kappl. *Physics and chemistry of interfaces*. John Wiley & Sons, 2023.

[36] J. W. Cahn and J. E. Hilliard. Free energy of a nonuniform system. i. interfacial free energy. *The Journal of chemical physics*, 28(2):258–267, 1958.

[37] P. B. Canham. The minimum energy of bending as a possible explanation of the biconcave shape of the human red blood cell. *Journal of Theoretical Biology*, 26 (1):61–81, 1970.

[38] E. Carrera. Theories and finite elements for multilayered, anisotropic, composite plates and shells. *Archives of Computational Methods in Engineering*, 9:87–140, 2002.

[39] O. Caty, E. Maire, S. Youssef, and R. Bouchet. Modeling the properties of closed-cell cellular materials from tomography images using finite shell elements. *Acta Materialia*, 56(19):5524–5534, 2008.

[40] P. G. Ciarlet. An introduction to differential geometry with applications to elasticity. *Journal of Elasticity*, 78(1):1–215, 2005.

[41] F. H. C. Crick and J. D. Watson. Structure of small viruses. *Nature*, 177(4506): 473–475, 1956.

[42] V. Crismale and G. Lazzaroni. Viscous approximation of quasistatic evolutions for a coupled elastoplastic-damage model. *Calculus of Variations and Partial Differential Equations*, 55:1–54, 2016.

[43] S. Dales. An electron microscope study of the early association between two mammalian viruses and their hosts. *The Journal of cell biology*, 13(2):303–322, 1962.

[44] M. E. Davis, Z. Chen, and D. M. Shin. Nanoparticle therapeutics: An emerging treatment modality for cancer. In *Nanoscience and technology: A collection of reviews from nature journals*, pages 239–250. World Scientific, 2010.

[45] L. De Lorenzis, P. Wriggers, and G. Zavarise. A mortar formulation for 3d large deformation contact using nurbs-based isogeometric analysis and the augmented lagrangian method. *Computational Mechanics*, 49:1–20, 2012.

[46] M. Dembo, D. C. Torney, K. Saxman, and D. Hammer. The reaction-limited kinetics of membrane-to-surface adhesion and detachment. *Proc. R. Soc. Lond. B. Biol. Sci.*, 234:55–83, 1988.

[47] B. V. Derjaguin, V. M. Muller, and Y. P. Toporov. Effect of contact deformations on the adhesion of particles. *J. Colloid Interf. Sci.*, 53(2):314–326, 1975.

[48] W. Dettmer and S. Reese. On the theoretical and numerical modelling of armstrong–frederick kinematic hardening in the finite strain regime. *Computer Methods in Applied Mechanics and Engineering*, 193(1-2):87–116, 2004.

[49] K. Dill and S. Bromberg. *Molecular driving forces: Statistical thermodynamics in biology, chemistry, physics, and nanoscience*. Garland Science, 2012.

[50] B. J. Dimitrijevic and K. Hackl. A method for gradient enhancement of continuum damage models. *Technische Mechanik-European Journal of Engineering Mechanics*, 28(1):43–52, 2008.

[51] T. X. Duong, F. Roohbakhshan, and R. A. Sauer. A new rotation-free isogeometric thin shell formulation and a corresponding continuity constraint for patch boundaries. *Comput. Methods. Appl. Mech. Eng.*, 316:43–83, 2017.

[52] T. X. Duong, F. Roohbakhshan, and R. A. Sauer. A new rotation-free isogeometric thin shell formulation and a corresponding continuity constraint for patch boundaries. *Computer Methods in Applied Mechanics and Engineering*, 316:43–83, 2017.

[53] W. Engl, B. Arasi, L. L. Yap, J. P. Thiery, and V. Viasnoff. Actin dynamics modulate mechanosensitive immobilization of e-cadherin at adherens junctions. *Nat. Cell Biol.*, 16(6):584–591, 2014.

[54] E. M. Fallon, S. F. Liparoto, K. J. Lee, T. L. Ciardelli, and D. A. Lauffenburger. Increased endosomal sorting of ligand to recycling enhances potency of an interleukin-2 analog. *J. Biol. Chem.*, 275(10):6790–6797, 2000.

[55] M. Fassin, R. Eggersmann, S. Wulfinghoff, and S. Reese. Gradient-extended anisotropic brittle damage modeling using a second order damage tensor–theory, implementation and numerical examples. *International Journal of Solids and Structures*, 167:93–126, 2019.

[56] S. F. Fenz, T. Bihr, D. Schmidt, R. Merkel, U. Seifert, K. Sengupta, and A. S. Smith. Membrane fluctuations mediate lateral interaction between cadherin bonds. *Nat. Phys.*, 13(9):906–913, 2017.

[57] G. Francfort and J.-J. Marigo. Revisiting brittle fracture as an energy minimization problem. *Journal of the Mechanics and Physics of Solids*, 46(8):1319–1342, 1998.

[58] G. A. Francfort and J.-J. Marigo. Revisiting brittle fracture as an energy minimization problem. *Journal of the Mechanics and Physics of Solids*, 46(8):1319–1342, 1998.

[59] F. Fraternali. Free discontinuity finite element models in two-dimensions for in-plane crack problems. *Theoretical and Applied Fracture Mechanics*, 47(3):274–282, 2007.

[60] F. Freddi and F. Iurlano. Numerical insight of a variational smeared approach to cohesive fracture. *Journal of the Mechanics and Physics of Solids*, 98:156–171, 2017.

[61] L. B. Freund and Y. Lin. The role of binder mobility in spontaneous adhesive contact and implications for cell adhesion. *J. Mech. Phys. Solids*, 52:2455–2472, 2004.

[62] H. Gao, W. Shi, and L. B. Freund. Mechanics of receptor-mediated endocytosis. *PNAS*, 102(27):9469–9474, 2005.

[63] X. Gao, Z. Huang, J. Qu, and D. Fang. A curvature-dependent interfacial energy-based interface stress theory and its applications to nano-structured materials:(i) general theory. *Journal of the Mechanics and Physics of Solids*, 66:59–77, 2014.

[64] I. L. García and M. Marsh. A biophysical perspective on receptor-mediated virus entry with a focus on hiv. *BBA-Bioenergetics*, 1862(6):183158, 2020.

[65] M. C. Geoffrey and R. E. Hausman. *The cell: A molecular approach.* Boston University, Sunderland, 2000.

[66] M. M. Gibbons, T. Chou, and M. R. D'Orsogna. Diffusion-dependent mechanisms of receptor engagement and viral entry. *J. Phys. Chem. B*, 114:15403–15412, 2010.

[67] S. K. Godunov and I. Bohachevsky. Finite difference method for numerical computation of discontinuous solutions of the equations of fluid dynamics. *Matematičeskij sbornik*, 47(3):271–306, 1959.

[68] B. Gorissen, D. Melancon, N. Vasios, M. Torbati, and K. Bertoldi. Inflatable soft jumper inspired by shell snapping. *Science Robotics*, 5(42):eabb1967, 2020.

[69] D. C. Grahame. The electrical double layer and the theory of electrocapillarity. *Chemical reviews*, 41(3):441–501, 1947.

[70] M. E. Gurtin and A. Ian Murdoch. A continuum theory of elastic material surfaces. *Archive for Rational Mechanics and Analysis*, 57:291–323, 1975.

[71] T. Heitbreder, P. Kurzeja, and J. Mosler. On general imperfect interfaces with spatially non-constant displacement jumps. *International Journal of Solids and Structures*, 232:111068, 2021.

[72] W. Helfrich. Size distributions of vesicles: the role of the effective rigidity of membranes. *Journal de Physique*, 47(2):321–329, 1986.

[73] W. Helfrich. Elastic properties of lipid bilayers: theory and possible experiments. *Zeitschrift für Naturforschung c*, 28(11-12):693–703, 1973.

[74] M. Hofacker and C. Miehe. A phase field model of dynamic fracture: Robust field updates for the analysis of complex crack patterns. *International Journal for Numerical Methods in Engineering*, 93(3):276–301, 2013.

[75] M. Hubbard and W. Stronge. Bounce of hollow balls on flat surfaces. *Sports Engineering*, 4(2):49–61, 2001.

[76] T. J. Hughes, J. A. Cottrell, and Y. Bazilevs. Isogeometric analysis: Cad, finite elements, nurbs, exact geometry and mesh refinement. *Computer Methods in Applied Mechanics and Engineering*, 194(39-41):4135–4195, 2005.

[77] R. J. Hunter. Foundations of colloid science. 2001.

[78] S. Ilic, K. Hackl, and R. P. Gilbert. Application of the multiscale FEM to the modeling of cancellous bone. *Biomech. Model. Mechanobiol.*, 9:87–102, 2010.

[79] A. Javili and P. Steinmann. A finite element framework for continua with boundary energies. part iii: The thermomechanical case. *Computer Methods in Applied Mechanics and Engineering*, 200(21-22):1963–1977, 2011.

[80] A. Javili, F. Dell'Isola, and P. Steinmann. Geometrically nonlinear higher-gradient elasticity with energetic boundaries. *Journal of the Mechanics and Physics of Solids*, 61(12):2381–2401, 2013.

[81] A. Javili, P. Steinmann, and J. Mosler. Micro-to-macro transition accounting for general imperfect interfaces. *Computer Methods in Applied Mechanics and Engineering*, 317:274–317, 2017.

[82] K. L. Johnson. *Contact mechanics*. Press, Cambridge University, 1985.

[83] K. L. Johnson, K. Kendall, and A. D. Roberts. Surface energy and the compact of elastic solids. *Proc. Roy. Soc. Lond*, 324:301–313, 1971.

[84] M. Kamyabi, R. Sotudeh-Gharebagh, R. Zarghami, and K. Saleh. Principles of viscous sintering in amorphous powders: A critical review. *Chemical Engineering Research and Design*, 125:328–347, 2017.

[85] A. Karma, D. A. Kessler, and H. Levine. Phase-field model of mode iii dynamic fracture. *Physical Review Letters*, 87(4):045501, 2001.

[86] D. Kaurin. A theoretical and computational study of soft adhesion mediated by mobile binders. *Doctoral Thesis, Universitat Politècnica de Catalunya, BarcelonaTech, Barcelona, Spain*, 2018.

[87] A. Kennedy. Porous metals and metal foams made from powders. *Powder Metallurgy*, 2:31–46, 2012.

[88] A. S. Khan and K. M. Jackson. On the evolution of isotropic and kinematic hardening with finite plastic deformation part i: compression/tension loading of ofhc copper cylinders. *International journal of plasticity*, 15(12):1265–1275, 1999.

[89] B. Kiefer, T. Waffenschmidt, L. Sprave, and A. Menzel. A gradient-enhanced damage model coupled to plasticity-multi-surface formulation and algorithmic concepts. *International Journal of Damage Mechanics*, 27(2):253–295, 2018.

[90] K. S. Kim, R. M. McMeeking, and K. L. Johnson. Adhesion, slip, cohesive zones and energy fluxes for elastic spheres in contact. *J. Mech. Phys. Solids*, 46(2): 243–266, 1998.

[91] O. Kintzel. *Modeling of elasto-plastic material behavior and ductile micropore damage of metallic materials at large deformations*. PhD thesis, Dissertation, Bochum, Ruhr-Universität Bochum, 2006, 2007.

[92] M. Kobayashi and N. Ohno. Implementation of cyclic plasticity models based on a general form of kinematic hardening. *International Journal for Numerical Methods in Engineering*, 53(9):2217–2238, 2002.

[93] H. Krobath, G. J. Schütz, R. Lipowsky, and T. R. Weikl. Lateral diffusion of receptor-ligand bonds in membrane adhesion zones: Effect of thermal membrane roughness. *EPL (Europhysics Letters)*, 78:38003, 2007.

[94] H. Krobath, B. Różycki, R. Lipowsky, and T. R. Weikl. Binding cooperativity of membrane adhesion receptors. *Soft Matter*, 5:3354–3361, 2009.

[95] C. Kuhn and R. Müller. A continuum phase field model for fracture. *Engineering Fracture Mechanics*, 77(18):3625–3634, 2010.

[96] P. Kurzeja and H. Steeb. Acoustic waves in saturated porous media with gas bubbles. *Philosophical Transactions of the Royal Society A*, 380(2237):20210370, 2022.

[97] K. Langenfeld, P. Kurzeja, and J. Mosler. On the curvature dependence of gradient damage models: Control and opportunities. *Computer Methods in Applied Mechanics and Engineering*, 410:115987, 2023.

[98] B. Li, C. Peco, D. Millán, I. Arias, and M. Arroyo. Phase-field modeling and simulation of fracture in brittle materials with strongly anisotropic surface energy. *International Journal for Numerical Methods in Engineering*, 102(3-4):711–727, 2015.

[99] A. M. Lieto, R. C. Cush, and N. L. Thompson. Ligand-receptor kinetics measured by total internal reflection with fluorescence correlation spectroscopy. *Biophys. J.*, 85:3294–3302, 2003.

[100] A. Lion. Constitutive modelling in finite thermoviscoplasticity: a physical approach based on nonlinear rheological models. *International Journal of Plasticity*, 16(5):469–494, 2000.

[101] V. A. Lubarda and D. J. Benson. On the numerical algorithm for isotropic–kinematic hardening with the armstrong–frederick evolution of the back stress. *Computer Methods in Applied Mechanics and Engineering*, 191(33):3583–3596, 2002.

[102] G. Lührs, S. Hartmann, and P. Haupt. On the numerical treatment of finite deformations in elastoviscoplasticity. *Computer Methods in Applied Mechanics and Engineering*, 144(1-2):1–21, 1997.

[103] D. Maugis. Adhesion of spheres: The jkr-dmt transition using a dugdale model. *J. Colloid Interf. Sci.*, 150(1):243–269, 1992.

[104] C. Maurini, B. Bourdin, G. Gauthier, and V. Lazarus. Crack patterns obtained by unidirectional drying of a colloidal suspension in a capillary tube: experiments and numerical simulations using a two-dimensional variational approach. In *Fracture Phenomena in Nature and Technology: Proceedings of the IUTAM Symposium on Fracture Phenomena in Nature and Technology held in Brescia, Italy, 1-5 July 2012*, pages 75–91. Springer, 2014.

[105] C. Miehe, M. Hofacker, and F. Welschinger. A phase field model for rate-independent crack propagation: Robust algorithmic implementation based on operator splits. *Computer Methods in Applied Mechanics and Engineering*, 199 (45-48):2765–2778, 2010.

[106] C. Miehe, F. Welschinger, and M. Hofacker. Thermodynamically consistent phase-field models of fracture: Variational principles and multi-field fe implementations. *International journal for numerical methods in engineering*, 83(10):1273–1311, 2010.

[107] C. Miehe, M. Hofacker, L.-M. Schänzel, and F. Aldakheel. Phase field modeling of fracture in multi-physics problems. part ii. coupled brittle-to-ductile failure criteria and crack propagation in thermo-elastic–plastic solids. *Computer Methods in Applied Mechanics and Engineering*, 294:486–522, 2015.

[108] C. Miehe, F. Aldakheel, and A. Raina. Phase field modeling of ductile fracture at finite strains: A variational gradient-extended plasticity-damage theory. *Interna-*

tional Journal of Plasticity, 84:1–32, 2016.

[109] F. Mollica, K. Rajagopal, and A. Srinivasa. The inelastic behavior of metals subject to loading reversal. *International Journal of Plasticity*, 17(8):1119–1146, 2001.

[110] M. A. Msekh, J. M. Sargado, M. Jamshidian, P. M. Areias, and T. Rabczuk. Abaqus implementation of phase-field model for brittle fracture. *Computational Materials Science*, 96:472–484, 2015.

[111] J. Nam and M. M. Santore. The adhesion kinetics of sticky vesicles in tension: The distinction between spreading and receptor binding. *Langmuir*, 23(21):10650–10660, 2007.

[112] S. Narayan and L. Anand. A gradient damage theory of fracture of quasibrittle materials. *Journal of the Mechanics and Physics of Solids*, 129:119–146, 2019.

[113] M. Negri and M. Paolini. Numerical minimization of the mumford–shah functional. *Calcolo*, 38:67–84, 2001.

[114] V. P. Nguyen, C. Anitescu, S. P. Bordas, and T. Rabczuk. Isogeometric analysis: an overview and computer implementation aspects. *Mathematics and Computers in Simulation*, 117:89–116, 2015.

[115] K. Nip, L. Gardner, C. Davies, and A. Elghazouli. Extremely low cycle fatigue tests on structural carbon steel and stainless steel. *Journal of constructional steel research*, 66(1):96–110, 2010.

[116] N. Ohno and J.-D. Wang. Kinematic hardening rules with critical state of dynamic recovery, part i: formulation and basic features for ratchetting behavior. *International journal of plasticity*, 9(3):375–390, 1993.

[117] N. S. Ottosen, M. Ristinmaa, and J. Mosler. Framework for non-coherent interface models at finite displacement jumps and finite strains. *Journal of the Mechanics and Physics of Solids*, 90:124–141, 2016.

[118] L. Piegl and W. Tiller. *The NURBS book*. Springer Science & Business Media, 1996.

[119] D. Pino-Munoz, J. Bruchon, S. Drapier, and F. Valdivieso. Sintering at particle scale: an eulerian computing framework to deal with strong topological and material discontinuities. *Archives of Computational Methods in Engineering*, 21: 141–187, 2014.

[120] D. Proserpio, M. Ambati, L. De Lorenzis, and J. Kiendl. Phase-field simulation of ductile fracture in shell structures. *Computer Methods in Applied Mechanics and Engineering*, 385:114019, 2021.

[121] A. Puzrin and G. Houlsby. Fundamentals of kinematic hardening hyperplasticity. *International journal of solids and structures*, 38(21):3771–3794, 2001.

[122] J. N. Reddy. An introduction to the finite element method. *New York*, 27:14, 1993.

[123] L. Rubinshteĭn. *The stefan problem*, volume 27. American Mathematical Soc., 1971.

[124] R. A. Sauer, T. X. Duong, K. K. Mandadapu, and D. J. Steigmann. A stabilized finite element formulation for liquid shells and its application to lipid bilayers. *J. Comput. Phys.*, 330:436–466, 2017.

[125] R. A. Sauer and T. X. Duong. On the theoretical foundations of thin solid and liquid shells. *Mathematics and Mechanics of Solids*, 22(3):343–371, 2017.

[126] R. A. Sauer, T. X. Duong, and C. J. Corbett. A computational formulation for constrained solid and liquid membranes considering isogeometric finite elements. *Computer Methods in Applied Mechanics and Engineering*, 271:48–68, 2014.

[127] E. J. Savitha and R. A. Sauer. A new anisotropic bending model for nonlinear shells: Comparison with existing models and isogeometric finite element implementation. *International Journal of Solids and Structures*, 268:112169, 2023.

[128] A. Schlüter, A. Willenbücher, C. Kuhn, and R. Müller. Phase field approximation of dynamic brittle fracture. *Computational Mechanics*, 54:1141–1161, 2014.

[129] E. M. Schmid and H. T. McMahon. Integrating molecular and network biology to decode endocytosis. *Nature*, 448:883–888, 2007.

[130] B. Schmidt, F. Fraternali, and M. Ortiz. Eigenfracture: an eigendeformation approach to variational fracture. *Multiscale Modeling & Simulation*, 7(3):1237–1266, 2009.

[131] S. Shames. First-order solution to glass-ice stefan problem. *Wolfram Demonstrations Project*.

[132] V. B. Shenoy and L. B. Freund. Growth and shape stability of a biological membrane adhesion complex in the diffusion-mediated regime. *Proceedings of the National Academy of Sciences*, 102:3213–3218, 2005.

[133] A. S. Smith, K. Sengupta, S. Goennenwein, U. Seifert, and E. Sackmann. Force-induced growth of adhesion domains is controlled by receptor mobility. *PNAS*, 105 (19):6906–6911, 2008.

[134] M. H. Smith and J. R. Berman. What is rheumatoid arthritis? *Jama*, 327(12): 1194–1194, 2022.

[135] A. Sorkin. Cargo recognition during clathrin-mediated endocytosis: A team effort. *Curr. Opin. Cell Biol.*, 16:392–399, 2004.

[136] D. J. Steigmann. Koiter's shell theory from the perspective of three-dimensional nonlinear elasticity. *Journal of Elasticity*, 111:91–107, 2013.

[137] D. J. Steigmann, M. Bîrsan, and M. Shirani. *Lecture notes on the theory of plates and shells: classical and modern developments*, volume 274. Springer Nature, 2023.

[138] D. Steigmann. On the relationship between the cosserat and kirchhoff-love theories of elastic shells. *Mathematics and Mechanics of Solids*, 4(3):275–288, 1999.

[139] S. X. Sun and D. Wirtz. Mechanics of enveloped virus entry into host cells. *Biophys. J.*, 90(1):L10–L12, 2006.

[140] B. Svendsen, S. Arndt, D. Klingbeil, and R. Sievert. Hyperelastic models for elasto-plasticity with non-linear isotropic and kinematic hardening at large deformation. *International journal of solids and structures*, 35(25):3363–3389, 1998.

[141] X. Tao, L. Zhang, and Y. Zhao. Al matrix syntactic foam fabricated with bimodal ceramic microspheres. *Materials & Design*, 30(7):2732–2736, 2009.

[142] E. Tasciotti, X. Liu, R. Bhavane, K. Plant, A. D. Leonard, B. K. Price, M. M. Cheng, P. Decuzzi, J. M. Tour, F. Robertson, and M. Ferrari. Mesoporous silicon particles as a multistage delivery system for imaging and therapeutic applications. *Nat. Nanotechnol.*, 3:151–157, 2008.

[143] A. Tozeren, K. L. Sung, and S. Chien. Theoretical and experimental studies on cross-bridge migration during cell disaggregation. *Biophys. J.*, 55(3):479–487, 1989.

[144] Y.-H. Tseng and H. Huang. An immersed boundary method for endocytosis. *J. Comput. Phys.*, 273:143–159, 2014.

[145] P. K. Tsourkas, N. Baumgarth, S. I. Simon, and S. Raychaudhuri. Mechanisms of b-cell synapse formation predicted by monte carlo simulation. *Biophys. J.*, 92: 4196–4208, 2007.

[146] S. Tzlil, M. Deserno, W. M. Gelbart, and A. Ben-Shaul. A statistical-thermodynamic model of viral budding. *Biophys. J.*, 86(4):2037–2048, 2004.

[147] A. C. Ugural. *Stresses in beams, plates, and shells*. CRC press, 2009.

[148] J. Vlachopoulos, O. Pokluda, C. Bellehumeur, and J. Machopoulos. Modification of frenkel's model for sintering. *Aiche J*, 43, 1997.

[149] F. Wakai, K. Katsura, S. Kanchika, Y. Shinoda, T. Akatsu, and K. Shinagawa. Sintering force behind the viscous sintering of two particles. *Acta Materialia*, 109: 292–299, 2016.

[150] Q. Wang, Z. Qu, and D. Tian. Electric double layer theory of interfacial ionic liquids for capturing ion hierarchical aggregation and anisotropic dynamics. *Advanced Energy Materials*, 15(13):2402974, 2024.

[151] Q. Wang and X. Zhao. A three-dimensional phase diagram of growth-induced surface instabilities. *Scientific reports*, 5(1):8887, 2015.

[152] S. Watanabe, Q. Liu, M. W. Davis, G. Hollopeter, N. Thomas, N. B. Jorgensen, and E. M. Jorgensen. Ultrafast endocytosis at caenorhabditis elegans neuromuscular junctions. *Elife*, 2:e00723, 2013.

[153] J. Webb. Imposing linear constraints in finite-element analysis. *Communications in Applied Numerical Methods*, 6(6):471–475, 1990.

[154] T. R. Weikl, M. Asfaw, H. Krobath, B. Różycki, and R. Lipowsky. Adhesion of membranes via receptor-ligand complexes: Domain formation, binding cooperativity, and active processes. *Soft Matter*, 5:3213–3224, 2009.

[155] M. F. Wheeler, T. Wick, and W. Wollner. An augmented-lagrangian method for the phase-field approach for pressurized fractures. *Computer Methods in Applied Mechanics and Engineering*, 271:69–85, 2014.

[156] T. Wiegold, S. Klinge, P. Kurzeja, and J. Mosler. Non-linear thermo-mechanical modeling of hollow sphere shells using isogeometric analysis. *Submitted*.

[157] T. Wiegold, S. Klinge, R. P. Gilbert, and G. A. Holzapfel. Numerical simulation of the viral entry into a cell driven by receptor diffusion. *Computers & Mathematics with Applications*, 84:224–243, 2021.

[158] H. Wilbuer, P. Kurzeja, and J. Mosler. Phase field modeling of hyperelastic material interfaces - theory, implementation and application to phase transformations. *Computer Methods in Applied Mechanics and Engineering*, 426:116972, 2024.

[159] Z. A. Wilson and C. M. Landis. Phase-field modeling of hydraulic fracture. *Journal of the Mechanics and Physics of Solids*, 96:264–290, 2016.

[160] Z. A. Wilson, M. J. Borden, and C. M. Landis. A phase-field model for fracture in piezoelectric ceramics. *International Journal of Fracture*, 183:135–153, 2013.

[161] M. Wolff, B. Suhr, and C. Şimşir. Parameter identification for an armstrong–frederick hardening law for supercooled austenite of sae 52100 steel. *Computational materials science*, 50(2):487–495, 2010.

[162] J.-Y. Wu and H.-Y. Chen. Membrane-adhesion-induced phase separation of two species of junctions. *Phys. Rev. E Stat. Nonlin. Soft Matter Phys.*, 73:011914, 2006.

[163] N. Yang, P. Canavan, H. Nayeb-Hashemi, B. Najafi, and A. Vaziri. Protocol for constructing subject-specific biomechanical models of knee joint. *Computer methods in biomechanics and biomedical engineering*, 13(5):589–603, 2010.

[164] X. Yi and H. Gao. Kinetics of receptor-mediated endocytosis of elastic nanoparticles. *Nanoscale*, 9(1):454–463, 2017.

[165] J. Yvonnet, H. L. Quang, and Q. C. He. An xfem/level set approach to modelling surface/interface effects and to computing the size-dependent effective properties of nanocomposites. *Computational Mechanics*, 42:119–131, 2008.

[166] Q. Zhang, Y. Li, and R. W. Tsien. The dynamic control of kiss-and-run and vesicular reuse probed with single nanoparticles. *Science*, 323(5920):1448–1453, 2009.

Publication series of the Institute of Mechanics

published to date:

2010/01 Palnau, V.: Implementierung eines netzfreien Diskretisierungsverfahrens und seine Anwendung auf die Scherbandanalyse.
ISBN 978-3-921823-51-4

2010/02 Klusemann, B.: Application of homogenization methods and crystal plasticity to the modeling of heterogeneous materials of technological interest.
ISBN 978-3-921823-53-8

2011/01 Hortig, C.: Local and non-local thermomechanical modeling and finite-element simulation of high-speed cutting.
ISBN 978-3-921823-54-5

2011/02 Parvizian, F.: Modeling of microstructure evolution in aluminum alloys during hot extrusion.
ISBN 978-3-921823-56-9

2011/03 Noman, M.: Characterization and model identification for the simulation of the forming behavior of ferritic steels.
ISBN 978-3-921823-55-2

2011/04 Kayser, T.: Characterization of microstructure in aluminum alloys based on electron backscatter diffraction.
ISBN 978-3-921823-57-6

2011/05 Bargmann, S.: Computational modeling of material behavior on different scales based on continuum mechanics.
ISBN 978-3-921823-58-3

2013/01 Waffenschmidt, T.: Modelling and simulation of adaptation and degradation in anisotropic biological tissues.
ISBN 978-3-921823-61-3

2015/01 Ostwald, R.: Modelling and simulation of phase-transformations in elastoplastic polycrystals.
ISBN 978-3-921823-66-8

2016/01 Subramanian, M.: Phenomenological modelling and simulation of ferroelectric ceramics.
ISBN 978-3-921823-74-3

2016/02 Clausmeyer, T.: Evolution of plastic anisotropy in metals.
ISBN 978-3-921823-76-7

2017/01 Holtermann, R.: Computational multiscale modelling of grinding processes.
ISBN 978-3-921823-86-6

2017/02 Bartels, A.: Modelling of evolving microstructures at different scales.
ISBN 978-3-921823-93-4

2017/03 Dusthakar Kumar Rao, D. K.: Computational modelling of single and polycrystalline ferroelectric materials.
ISBN 978-3-921823-94-1

2019/01 Buckmann, K.: Microstructure evolution in functional magnetic materials.
ISBN 978-3-947323-09-8

2019/02 Kaiser, T.: Computational modelling of non-simple and anisotropic materials.
ISBN 978-3-947323-14-2

2019/03 Heitbreder, T.: Modelling of material interfaces at different length scales.
ISBN 978-3-947323-18-0

2020/01 Berthelsen, R.: Computational homogenisation of thermomechanical problems.
ISBN 978-3-947323-19-7

2020/02 Sievers, C.: Describing the macroscopic behavior of surfaces based on atomistic models.
ISBN 978-3-947323-24-1

2022/01 Rose, L.: Optimisation based parameter identification using optical field measurements.
ISBN 978-3-947323-31-9

2023/01 Langenfeld, K.: Continuum modeling of brittle and ductile damage: theory and computational frameworks.
ISBN 978-3-947323-41-8

2023/02 Schulte, R.: Parameter identification approaches with application to different classes of materials.
ISBN 978-3-947323-45-6

2023/03 Kaiser, T.: Multiscale multiphysics material modelling.
ISBN 978-3-947323-46-3

2024/01 Noll, I.: Thermomechanical modelling and simulation of laser powder bed fusion processes.
ISBN 978-3-947323-49-4

2024/02 Witt, C.: Isogeometric analysis of anisotropic mechanical and electromechanical higher-gradient continua.
ISBN 978-3-947323-50-0

2025/01 Kurzeja, P.: Modeling, control and opportunities of mechanical interfaces across the scales.
ISBN 978-3-947323-51-7

2025/02 Lammen, H.: Modeling and simulation of general imperfect interfaces using phase-field-theory.
ISBN 978-3-947323-52-4

2025/03 Sprave, L.: Computational modelling and simulation of ductile damage in metals.
ISBN 978-3-947323-54-8

2025/04 Schewe, M.: Computational modelling of surface interactions – wear, material separation and deposition.
ISBN 978-3-947323-55-5

2025/05 Wiegold, M.: On the numerical modeling of interfaces in engineering applications.
ISBN 978-3-947323-53-1